



AALBORG UNIVERSITY
DENMARK

Numerical and Experimental Investigation of Two-Phase Flows in Mini-Channels

Master's Thesis

Mathias Kjær Christensen and Niels Gaardboe Rasmussen

Thermal Energy and Process Engineering, M.Sc.
Department of Energy Technology
Aalborg University



AALBORG UNIVERSITET
STUDENTERRAPPORT

Title:

Numerical and Experimental Investigation of Two-Phase Flows in Mini-Channels

Project:

Master Thesis

Project period:

February 2018 - June 2018

Project group:

TEPE4 - 1000

Group members:

Mathias Kjær Christensen
Niels Gaardboe Rasmussen

Supervisor:

Henrik Sørensen
Anders Christian Olesen

Pages: 101

Appendices: 6

Project deadline: 01-06-2018

**School of engineering
and science**

Energy Engineering

Pontoppidanstræde 111

9000 Aalborg

<http://www.ses.aau.dk/>

Abstract:

Two-phase flows properties in mini-channels are a topic of academic and industrial interest, especially within electrolyser technology, as these can prove valuable in the future energy grid. As scientific work on validation between experimental and numerical VOF and Two-fluid model work on two-phase flows in squared mini-channels is lacking, this was chosen as the main focus of the thesis. A numerical and experimental two-phase test scenario was determined with air supplied at a constant superficial velocity of 0.7 m/s and water at a constant superficial velocity of 0.4 m/s. Based on the set test scenario, a experimental and numerical geometry was build and the volume fractions and pressure losses was chosen as the main parameters of validation. The VOF and Two-phase model was utilized for the numerical part of the thesis, whilst a Plexiglas T-junction cell, with optical access and pressure transducers, was setup for the experimental work. Results indicated, that the VOF modelling and experimental results were in best correlation with each other. However, it was also reasoned in the discussion, that errors in the numerical settings by the authors and uncertainties in the experiment, could prove to lower the overall actual error between the different methodologies.

Preface

This master thesis has been made during the 4th semester on the Thermal Energy and Process Engineering M.Sc. program at Aalborg University.

Reading guide

The contents of the individual chapters in the report are introduced and concluded with a section written in *italic* font. Throughout the report all references are listed by the end of the appendix report, in the bibliography. The references are denounced cf. the Harvard method, hence a statement will be referred by [Surname, year]. If more than one reference from the same year has the same author, these are denoted with a, b, c and so forth. This reference refers to the bibliography where books are referred by author, title, ISBN-number, publisher, edition and year while websites are referred by author, title, year, URL and time of last visit. Technical papers are referred by author, title and year. Figures, tables and equations are numbered according to the particular chapter they are placed in. The first figure in chapter three will here-fore be assigned with figure number 3.1 and the second 3.2 etc. Descriptive captions for tables are found above relevant tables and captions for figures are found under relevant figures.

The authors' 9th-semester paper, which was submitted for an in-house conference held for students at The Department of Energy Technology, has been uploaded alongside this Master's Thesis as references have been made to it. However, it is not subject to be evaluated during the examination of this Master's Thesis.

Acknowledgements The authors would like to thank Anders Christian Olesen and Henrik Sørensen for their guidance and feedback during the whole project phase.

Aalborg University, June 1, 2018



Mathias Kjær Christensen



Niels Gaardboe Rasmussen

Summary

To-fase flow egenskaber i mini-kanaler, er et emne af akademisk og industrial interesse, specielt indenfor elektrolyse teknologien, da denne kan vise sig værdifuld i fremtidens energinet. Et anerkendt problem med elektrolyse cellerne er hotspot formationer i gas-diffusion laget af elektrolyse cellen, som kraftigt nedsætter elektrolyse cellens effektivitet. Hotspots opstår som funktion af to-fase flowdannelsen inden i mini-kanalerne. Et af løsningsforslagene på problemet er bedre numeriske modeller, som ligeledes vil kunne nedbringe materielle og eksperimentielle omkostninger. Udfordringen ved de numeriske modeller er, at de dynamiske elektro-kemiske processer inden i elektrolyse celler er svære at modellere præcist. Ligeledes, er det svært at forudsige to-fase flow fænomener, såsom flow regimer, inden i mini-kanalerne. Forfatterne af dette speciale har i forlængelse af dette besluttet at forsimple problemstillingen og tage en mere fluid mekanisk tilgang til problemstillingen. Denne vil blive udført både eksperimentielt og numerisk.

Da videnskabeligt arbejde omhandlende validering af eksperimentielt og numerisk arbejde i firkantede mini-kanaler er mangelfuldt, blev dette valgt som hovedfokus af specialet. Baseret på dette blev et numerisk og eksperimentielt test scenarie opstillet. I test scenariet skulle luft tilføres, en numerisk og eksperimentiel opstillet geometri, med en konstant overfladisk hastighed på 0.7 m/s, mens vand skulle tilføres med en konstant overfladisk hastighed på 0.4 m/s. Baseret på det opstillede scenarie blev volume fraktionerne og tryktabet over geometrien opstillet som valideringsparametre.

De numeriske VOF og to-fluids modeller er begge numeriske multi-fase modeller, som er baseret på Euler-Euler tilgangen. Dog variere modellerne i deres tilgang til at løse interfacet mellem de forskellige faser i modelleringen. To-fluids modellen tillader gennemtrængen mellem fluidernes faser, og løser de underliggende numeriske ligninger, som en steady-state løsning. Modsat, tillader VOF modellen ikke gennemtrængen mellem fluidernes faser og løser de underliggende numeriske ligninger transient. Akademisk set, er VOF modellen bredt anerkendt som den mest præcise metode til modellering af to-fase flows. Dog har VOF modellen også de største computationelle krav. Derfor, grundet to-fluid modellens højere simplicitet og lavere computationelle krav, vil denne blive testet imod den numeriske VOF model og et eksperiment, i forhold til at bestemme to-fluid modellens overordnede brugbarhed, som en løsningsstrategi til modellering af to-fase flows. Grid uafhængigheds studier af de involverede modeller blev udført for at bestemme deres et celle antal for deres numeriske uafhængighed. Studiet viste at to-fluid modellen krævede 197835 celler og VOF modellen krævede 756000 celler for numerisk uafhængighed. Dog blev VOF modelleringen kun udført på en del af den opstillede geometri, for at spare på det computationale domæne. I forlængelse af grid uafhængighedsstudiet, blev et model studie af to-fluid modellen ligeledes udført. Dette resulterede i to uafhængige scenarier, et basis og et fuldt udviklet scenarie, som blev testet mod den numeriske VOF model og det eksperimentielle arbejde.

Eksperimentet blev udgjort af en Plexiglas T-kryds celle med optisk tilgang, hvor vand blev tilført fra bunden af cellen og luft blev tilført til siden af cellen. Dette gjorde det muligt at studere formation af to-fase flowet i outlet sektionen af mini-kanalen. Endvidere, blev tryks transducere

tilføjet i toppen og bunden af cellen til at måle tryktabet.

En sammenligning af de opnåede resultater viste at tryktabet i base scenariet af to-fluid modellen var -70.77 % lavere end de eksperimentielle resultater, mens tryktabet i det fuldt udviklede scenarie var -60.01 % lavere. Sammenlignet med VOF modellen, var tryk tabet i base scenariet -80.59 % lavere og -70.13 % i det fuldt udviklede scenarie. Dette indikerede at VOF modellen og de eksperimentielle resultater lå i bedre correlation med hinanden end to-fluid modellen. Sidst blev volume fraktionerne mellem de numeriske og eksperimentielle metoder undersøgt og sammenlignet. Sammenligningen viste at den fuldt udviklede to-fluid model var tættest på de eksperimentielle resultater.

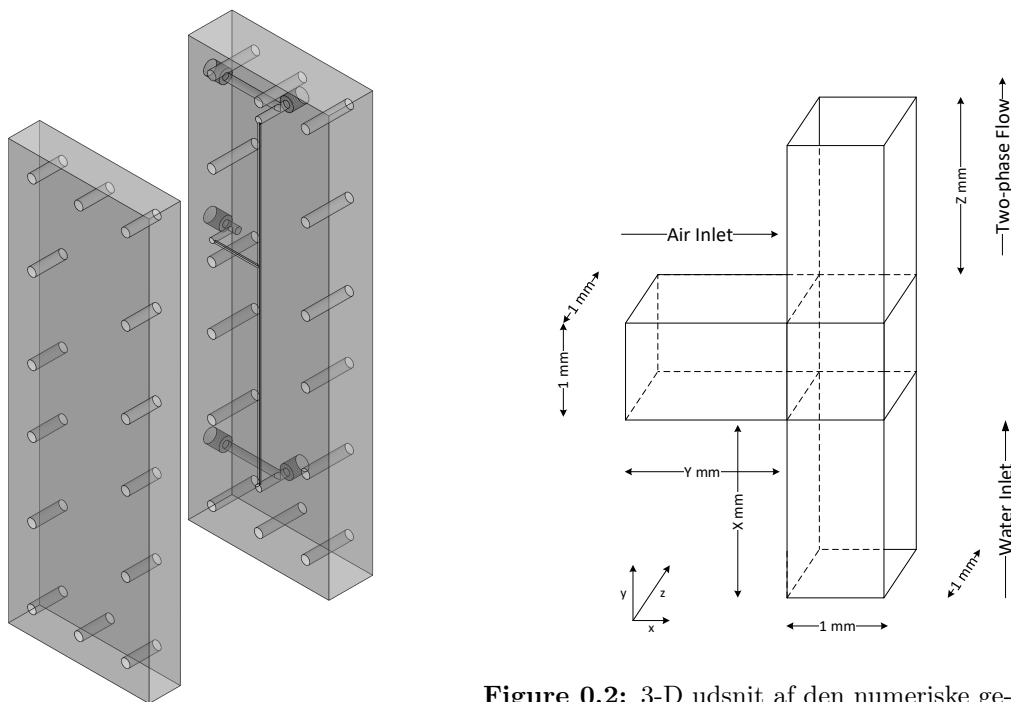


Figure 0.2: 3-D udsnit af den numeriske geometri.

Figure 0.1: 3-D tegning af den eksperimentielle geometri.

Contents

Nomenclature	11
1 Introduction	13
1.1 Research development of numerical and experimental work on two-phase flow: A state of the art review	18
1.2 Introduction to the framework of this project	20
1.3 Geometry of cell and mini-channel	21
2 Problem statement	27
2.1 Parameters of validation between the models	27
3 Numerical methodologies	29
3.1 Computational Fluid Dynamics (CFD)	29
3.2 Grid in-dependency study of the Two-fluid model	47
3.3 Investigation of additional physics models in the Two-fluid model	51
3.4 Grid in-dependency study of the VOF model	55
4 Experimental methodologies	59
4.1 Flow Measurement Techniques	59
4.2 Experimental Setup	63
5 Experimental and Numerical Results	71
5.1 Two-fluid model results	71
5.2 VOF model results	73
5.3 Experimental results	76
6 Discussion and Measures of Uncertainties	83
6.1 Comparison of pressure drop between the Two-fluid and experimental approach . .	83
6.2 Comparison of pressure drop in the numerical approaches	85
6.3 Comparison of estimated slug lengths	86
6.4 Comparison of volume fraction between numerical and experimental approaches . .	87
7 Conclusions	89
Bibliography	91
A Appendix A: Experimental equipment methodologies and limitations	95
A.1 Pressure transmitter	95
A.2 LED Lamp	97
A.3 Mass Flow Controller	98
A.4 Water Pump	99
A.5 Flowmeter for water	100

B Appendix: Extra Uploaded Content

101

Nomenclature

The following list of symbols used in the report, are outlined in the order; lower- and upper case arabic notation, greek notation and the abbreviations.

Symbol	Description	Unit
A_c	Cross-sectional area	m^2
\vec{A}_i	Normal Vector	-
\vec{c}_i	Center cell vector	-
C_o	Courant Number	-
C	Law coefficient	-
D	Diameter	m
D_h	Hydraulic diameter	mm
d	Mean diameter	mm
F	Force	N
\vec{f}_i	Pointing vector	-
g	Gravitation acceleration	$m \cdot s^{-2}$
H	Height	mm
h	Enthalpy	J
k	Turbulence Kinetic Energy	$J \cdot kg^{-1}$
L_h	Entry length	m
m	Mass imbalance	%
\dot{m}	Mass Flow	$kg \cdot s^{-1}$
P	Pressure	bar / Pa
P_{wet}	Wetted perimeter	m
Q	Heat Exchange	
q	Heat Flux	$W \cdot m^{-2}$
R	Interaction Forces	N
S	Source Term	Arbitrary
T	Temperature	$^{\circ}C$
t	time	s
u	Superficial Velocity	$m \cdot s^{-1}$
U	Velocity	$m \cdot s^{-1}$
\dot{V}	Volume Flow	$L \cdot hr^{-1}$
W	Width	mm
y^+	y-plus	-
x	length	m

α	Volume Fraction	-
ρ	Density	$kg \cdot m^{-3}$
ϕ	General flow variable	Arbitrary
ϵ	Surface roughness	m
μ	Dynamic viscosity	$kg \cdot m^{-1} \cdot s^{-1}$
∇	Gradient	-
Γ	Effective diffusivity	-
ν	Kinematic viscosity	$m^2 \cdot s^{-1}$
θ	angle	$^\circ$
τ	Wall Shear Stresses	Pa
ω	Specific dissipation rate	$1 \cdot s^{-1}$
σ	Surface Tension Coefficient	$N \cdot m^{-1}$
Re	Reynolds number	-

Abbreviation	Description
ATL	Anode Transport Layer
BC	Boundary condition
CFD	Computational fluid dynamics
CV	Control volume
ECT	Electrical Capacitance Tomography
EWT	Enhanced Wall Treatment
FEM	Finite element method
FVM	Finite volume method
GDL	Gas Diffusion Layer
GUI	Graphical user interface
LED	Light-emitting diode
PMMA	plexiglas
PEMEC	Polymer Exchange Membrane Electrolyser
PIV	Particle image velocimetry
SOEC	Solid Oxide Electrolyser
SST	Shear-Stress Transport
VOF	Volume of fluid
WF	Wall Function

Introduction

1

This chapter presents the basis of the thesis and outlines the overall definitions and challenges of two-phased flows in mini-channels. Furthermore, a state-of-the-art on numerical and experimental work on two-phase flow in mini-channels will be presented to determine the direction of the thesis. Lastly, the framework of the project will be presented and the experimental geometries determined.

The worldwide demand for energy has been estimated by the European World Energy Technology and Climate Policy Outlook (WETO) to increase annually by 1.8 percent in the period of 2000-2030 [Commision, 2003] and, as can be seen in figure 1.1, the U.S Energy Information Administration (EIA) estimates a rise of 28 percent in the total world energy consumption from 2015 to 2040 [Administration, 2017]. Both agencies predict that the highest energy growth will occur in countries which are experiencing industrial and economic growth and that the increased energy demand will mostly be covered by fossil fuelled energy production and transportation. The usage of fossil fuels in both energy production and transportation is a large contributor of the emitted greenhouse gasses, which is predominantly the cause of global warming, and a transition away from fossil fuels is thus needed.

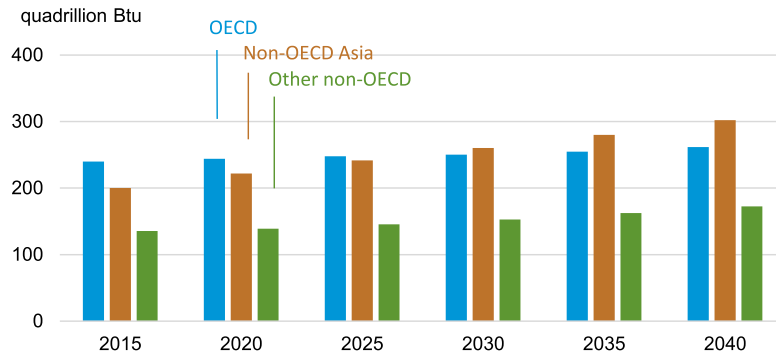


Figure 1.1: U.S. EIA projection for worldwide energy consumption up to year 2040 [Administration, 2017].

In 2012, Denmark instigated the “green transition” toward renewable energy sources, when the government signed an energy agreement with the target of at least 50% of the energy consumption in 2020 to be supplied by wind power. Furthermore with a ambitious target of an energy consumption from 100% renewable energy sources in 2050, [Government, 2012; og Energiministeriet, 2011], a revamp of the energy matrix is required [Carmo et al., 2013].

Hydrogen could prove valuable, as it can replace fossil fuels in almost every application, without the emission of most of the damaging greenhouse gasses. Furthermore, the conversion of hydrogen into useful energy may be more efficient than for fossil fuels. As hydrogen does not exist in nature in its elemental form it has to be produced. Thus, hydrogen is defined as a energy carrier – capable of storing and converting energy. Usually hydrogen has been produced through steam reforming of natural gas or other fossil fuels. However, this produces a hydrogen gas with a low purity and a high concentration of carbonaceous species. In addition, steam reforming does not relieve the reliance on fossil fuels or reduce the emission of greenhouse gasses. Another possibility is the electrochemical process called electrolysis, where water molecules are dissociated into hydrogen and oxygen as a voltage and direct current is applied. Compared to the steam reforming process, the purity of the hydrogen gas is vastly superior when it is produced by electrolysis. The overall equation for water electrolysis is as noted in equation 1.1



Different electrolyzers and methods for water electrolysis exist, each with their own advantages, disadvantages and future prospects [Lehner et al., 2014; Carmo et al., 2013].

Two of the most promising electrolyser types is the PEMEC (Polymer exchange membrane electrolyser) and SOEC (Solid oxide electrolyser). PEMEC and SOEC technology utilize mini-channels for dissociation of water into its respective products shown in equation 1.1. This dissociation is mainly controlled by the electrochemical processes inside the layers of the electrolyser and results in two-phase flow fields inside the micro-channels. However, if the electrochemical conversion processes is not monitored properly, effects inside the two-phase flow field, like hotspot formation, could arise and potentially damage the overall functionality of the electrolyser. Thus, two-phase flow field properties in mini-channels are of academic and industrial interest, as for instance electrolyzers could prove valuable as a part of the solution towards a fully sustainable energy grid in 2050, and needs to be examined more in-depth.

The articles of [Olesen et al., 2016; Lafmejani et al., 2017] and unpublished work of [Christensen and Rasmussen, 2017] all examine two-phase gas-liquid flows inside PEMECs, however using different methodologies.

[Olesen et al., 2016] continued previous work on single-phase flow field dynamics of the anode side of a PEMEC using a interdigitated, planar-circular cell design by [Olesen and Kær, 2014], with a numerical study of the gas-liquid two-phase flow in the anode of a high pressure PEMEC. The purpose of the study was to see how a two-phase flow would affect the flow field inside the PEMEC and disperse throughout the cell. [Olesen and Kær, 2014] had shown that the interdigitated design allowed for a thinner electrolysis cell design with a higher supply of water to the GDL (Gas Defusion Layer). However, the design also induced a higher pressure loss throughout the cell, which resulted in an uneven pressure distribution within the manifold and further caused an uneven mass flow distribution within the GDL. The preliminary results of [Olesen et al., 2016] was similar to the previous work when extended to a gas-liquid flow simulation. However, a parametric study showed that at low stoichiometric and nominal conditions, excessive formation of hotspots were observed in the two-phase simulation, compared to the single-phase. Furthermore the land area between the channels were shown to have an influence on the overall mass flow distribution. This indicated that the bubble size of gas through the micro-channels of the PEMEC were a property, which strongly affected the overall performance of the cell and that experimental validation on the subject was

necessary.

[Lafmejani et al., 2017] builds on the works of [Olesen et al., 2016] with a numerical VOF (Volume of fluid) CFD (Computational fluid dynamics) analysis of the gas-liquid flow through an interdigitated cell. To validate the VOF CFD simulations, an experiment based on photographs of the gas-liquid flow in transparent micro-channels of a PEMEC anode was conducted for comparison. The purpose was to gain further information and be able to predict flow phenomena, like flow patterns, within the anode channels and the anode transport layer (ATL). Figure 1.2 shows the possible flow regimes in micro-channels.

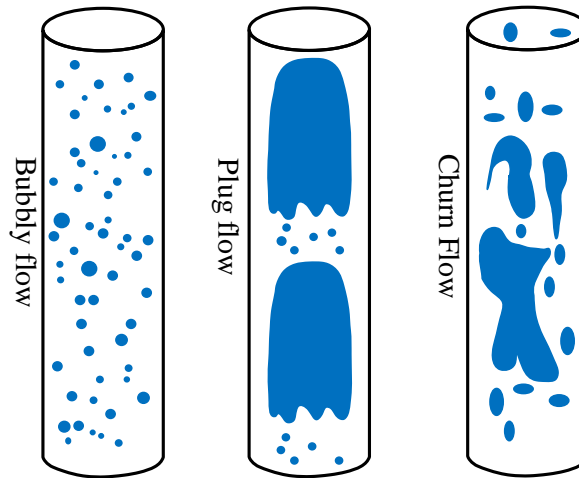


Figure 1.2: Possible gas-liquid flow types in PEMEC microchannels, drawn with inspiration from [Lafmejani et al., 2017].

According to the inlet conditions of the PEMEC and wall conditions in the micro-channels, the different flow regimes can be obtained throughout the electrolysis cell. [Lafmejani et al., 2017] utilized a 3-D structured mesh of the channels and ATL for an accurate computational representation of the area. The experimental setup was based on photos of a electrolysis cell with transparent flow plates made of Plexiglas and can be seen in figure 1.3. The setup made it possible to see the formation two-phase flow within the micro-channels during operation of the cell. The results showed a good coherence between the VOF CFD simulation and experimental setup. Furthermore the results showed that the distance between the bubbles in the incoming channel affected the uniformity of the flow and that long Taylor bubbles could show to make the flow more uniform. However a more detailed model and even better experimental understanding of two-phase flow in micro-channels is needed to obtain more information about the subject.

The unpublished work of [Christensen and Rasmussen, 2017] sought to develop the experimental work of [Lafmejani et al., 2017] and create a clear distinction between the gas-liquid phases in order to characterize the two-phase flow within the transparent PEMEC. Using an experimental approach similar to figure 1.3 with a high intensity lighting source from above and different camera settings created clear and distinct images of the two-phase flow in the mini-channels for further analysis.

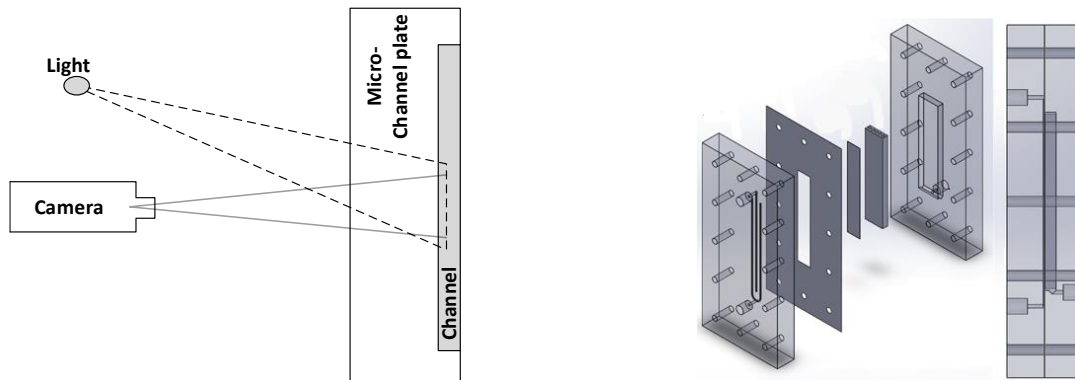


Figure 1.3: Overview of experimental setup and transparent electrolyser used for validation of VOF CFD modelling [Lafmejani et al., 2017].

By means of image processing the flow field inside the mini-channels could be characterized and two-phase variables, like void fractions, could be determined. However, it also showed that the methodology needed further refinement, according to different flow conditions. An example is seen in figure 1.4, where a low velocity bubble is captured by the image processing program, whereas a high velocity bubble resulted in discrepancies across the image. Furthermore, the results showed that the overall performance of the transparent PEMEC was low and that further experimentation and numerical work on the subject are needed, in order to gain more knowledge on the subject.

Further discussions between the authors of [Olesen et al., 2016] and [Christensen and Rasmussen, 2017] have resulted in a new direction of investigating two-phase flows in mini-channels. The

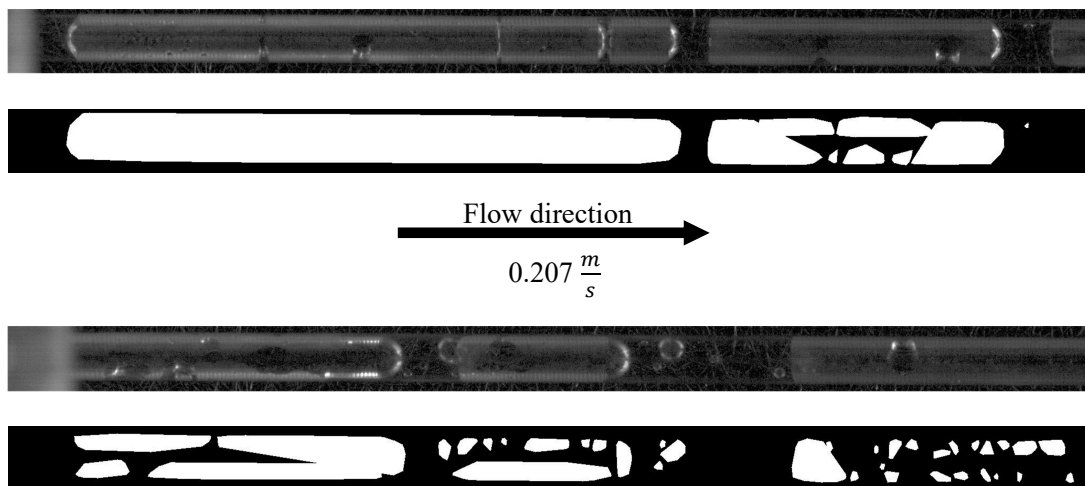


Figure 1.4: Example of original and processed image at liquid superficial velocities of 0.083 m/s and 0.207 m/s [Christensen and Rasmussen, 2017].

electro-chemical dynamics of hydrogen production from the PEMEC make it difficult to accurately simulate and predict fluid phenomena, like flow regimes, inside the mini-channel. Thus, the authors have decided to simplify and look away from the electro-chemical aspect of the PEMEC and take a more fluid mechanical approach to the two-phase flow characteristics in mini-channels, both numerically and experimentally.

Due to the size and layout of mini-channels, the characteristics of the two-phase flow and its heat-transfer is highly controlled by surface tension effects, compared to the forces (inertia, viscosity and gravity) which usually control flow characteristics in larger channels. The increased surface tension effects is furthermore seen to have an influence on the inertia and viscosity effects of the mini-channels. This results in several different two-phase phenomena for mini-channels. Some of the characteristic phenomena seen in mini-channels are high pressure drops across the mini-channel due to higher viscous effects and more complex interactions between the fluid and walls, as the surface and viscous forces dominates the gravitational forces seen for normal channels. Thus, two-phased flows in mini-channels is a area of academic interest, as these are not fully understood yet [Crowe, 2005].

The definitions of mini-channels are many and criteria for classification of mini-channels likewise. [Crowe, 2005] and [Saisorn and Wongwises, 2008] list several different definitions of mini-channels based on either geometrical constraints or fulfillment of dimensionless criterion's, like the Eötvös number which is a measure of how gravitational forces compare to the surface tension forces on objects, like bubbles and droplets, in channels. However, both authors conclude that a dimensionless analysis often is insufficient to describe the distinction between different channel sizes, as flow conditions have to be determined prior and are known to be dominated by surface tension effects. Thus, geometrical constraints seems to set more clear-cut criterion's for the distinction of channel sizes. Thus, this thesis will utilize geometrical constraints for distinction between different channel sizes.

[Kandlikar, 2002] examined how flow boiling in mini- and micro-channels generate issues in the prediction of heat transfer and pressure drop across single- and multi-channels. As a part of the study, the author examined flow boiling phenomena in heat exchangers as a function of the hydraulic diameter (D_h). These finding was related these to the geometrical dimensions of the channel and used to propose the following definition of distinction between channel sizes, as seen in table 1.1.

Table 1.1: Geometrical distinction sizes of channels [Kandlikar, 2002].

Geometrical definition of channel sizes	
Channel type	Size
Conventional Channels	$D_h > 3 \text{ mm}$
Mini-channels	$200 \mu\text{m} \leq D_h \leq 3 \text{ mm}$
Micro-channels	$10 \mu\text{m} \leq D_h \leq 200 \mu\text{m}$

As several studies on flow channels have utilized the following definition, this thesis will also use it for distinction between channel sizes.

As mentioned, flow conditions change during operation in mini-channels due to higher surface

forces. Another challenge, which needs to be addressed during experimental operation of mini-channels, is flow instability. Flow instability can occur due to the compressibility of the fluids at inlets and supply lines and wave instability of the fluids inside the mini-channel. Thus, these flow effects needs to be accounted for in the test setup to secure a proper operation. Thus, the used materials needs to be capable of withstanding the pressure effects of the compression. Furthermore in two-phase applications, a mixing-chamber needs to added to the test-setup in order to secure a proper mixing of the interacting fluids. Having described the basics surrounding two-phase flow in mini-channels, a state of the art review of scientific articles will present current numerical and experimental work on two-phase flows to determine the overall framework of this thesis.

1.1 Research development of numerical and experimental work on two-phase flow: A state of the art review

The review article of [Shao et al., 2009] focus on flow regime patterns forming during adiabatic gas-liquid flows in micro-channels and if the affecting parameters of transition between the flow regimes can be predicted. In the review six overall flow regimes was observed according to the superficial velocity ratio between the gas and liquid phase, namely: Bubbly, Taylor, Churn, Taylor-Annular, Dispersed and Annular flow. The flow regimes according to their superficial velocity ratio between gas and liquid phase, as well as the dominating forces within the flow regime, can be seen in figure 1.5.

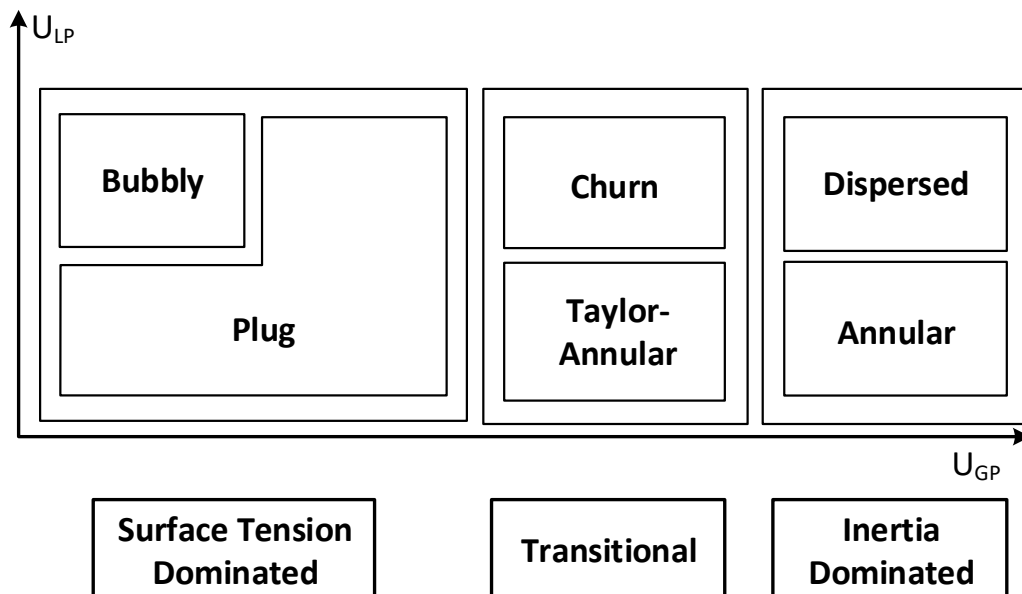


Figure 1.5: Flow regime in micro-channel according to superficial velocity ratio of gas and liquid phase, made with inspiration from [Shao et al., 2009].

From figure 1.5 it is seen that at low gas and liquid superficial velocities Bubbly - and Plug flow

appear and the two-phase flow is dominated by surface tension effects. Generally in the surface tension dominated region, the liquid phase will fill more of the channel than the gas phase. As the velocity of the gas phase is increased, the two-phase flow moves into the transitional dominated area where Churn and Taylor-Annular flow regimes are seen. Generally in the transitional region, the volume of the gas and liquid phase will be more or less equal. Lastly if the velocity of the gas phase increased further, the two-phase flow moves into the inertia dominated region where Dispersed and Annular are seen. Generally in the inertia dominated region the gas phase will fill more of the channel than the gas phase. The review compared flow pattern maps from several different studies and found no generalized flow pattern map, which accounted for all affecting parameters during transition between flow regimes. However, the review found that the parameters which affect the flow pattern and transition the most is the channel size, superficial velocities of the phases, surface tension between the phases, wettability of the channel and its geometry. Lastly, the review conclude that numerical simulations could prove helpful in further investigation of how parameters and boundary conditions affect the flow patterns inside micro-channels, whilst recognizing numerical work is challenging.

The article of [Guerrero et al., 2017] takes a numerical approach to the modelling of two-phase flows in vertical pipes with a comparison between the Two-fluid and VOF CFD models. The different models was validated against experimental results on similar channels by other authors. The purpose of the study was to demonstrate the difference between the tested models by analyzing their accuracy, ability to capture distinguishable phases and computational performance. The results showed that at low number of meshed cells, the VOF modelling had a higher error percentage compared to the Two-fluid modelling. However, as the cell count was increased, the error percentage of the VOF lowered, whilst the error percentage of the Two-fluid model was constant. The reason for this lie in the mathematical codes of the models. Both models solves the mass and momentum transfers of the two-phase flow. However, whilst the VOF model analyze each phase with a unique equation for mass and momentum transfer, the Two-fluid model only uses one equation to predict the different mass and momentum transfers across each phase. Thus the VOF model better details the bubbles in two-phase flows at higher cell counts, as it is able to resolve the continuity equations across the interface of the phases. On the contrary, the Two-fluid model does not resolve the contiunity equations across the interface of the phases. This results in average values of the each variable across the phases and a more uniform distribution of the results across the geometry. [Guerrero et al., 2017] recognize that both models give results of physical meaning for further interpretation. Due to mesh independency the Two-fluid model have a lower computational time and a lower average error percentage on the testing area. However, only the VOF model is capable of capturing the discontinuous and continuous phases in the solution.

The article of [Rajesh and Buwa, 2018] looks into VOF CFD simulation of gas-liquid-liquid flows in mini-channels. The use of multi-phase flows in mini-channels is propogated in microreactors for chemical processes, as the microreactors can intensify the utilized processes. Thus, the authors have investigated a multi-phase gas-liquid-liquid flow with a 3-D VOF CFD modelling and validated it with imaging experiments of a double T-junction experiment. The double T-junction was carved into a Plexiglas (PMMA) block and assembled with a Plexiglas back plate foroptical access to the mini-channel. Furthermore, to reduce the amount of leakage between the plates a thin layer of glue was applied. Thus, the geometry used for both numerical and experimental work can be seen in figure 1.6.

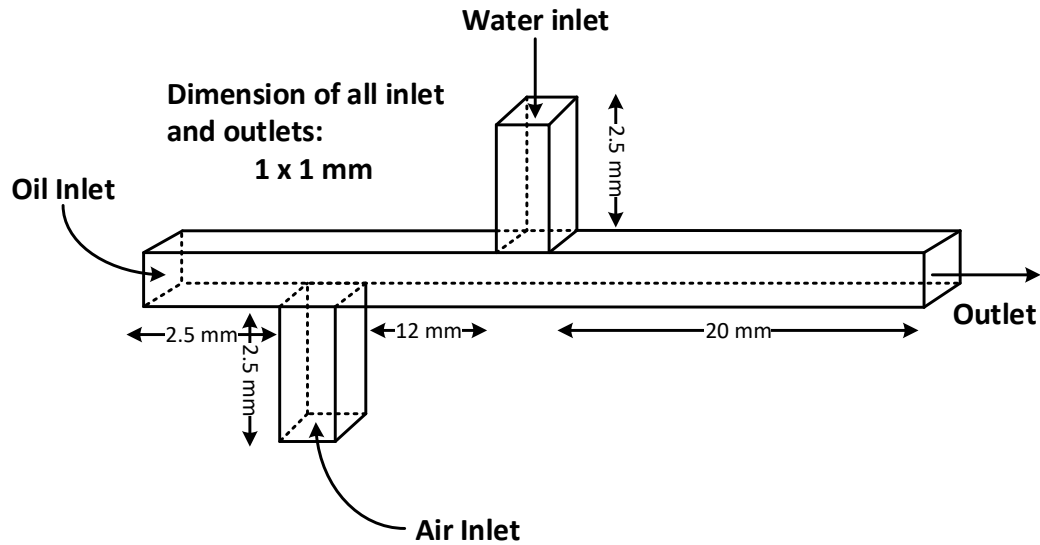


Figure 1.6: Experimental and numerical geometry used in [Rajesh and Buwa, 2018]. Drawn with inspiration from [Rajesh and Buwa, 2018]

A comparison between the results of the numerical and experimental work showed that after the first T-junction the dynamics of the bubble/slug formation was captured to a satisfactory degree. Furthermore, the results of the experimental flow regime mechanisms after the second T-junction could likewise be predicted with a good accuracy by the numerical model. Lastly a parametric study showed that different flow regimes could be predicted by the numerical model to a satisfactory degree. However, the study also showed situations after the second T-junction, where the results was over-predicted by the numerical model, which was explained by a shorter numerical domain.

1.2 Introduction to the framework of this project

Having described the basics surrounding two-phase flow in micro/mini-channels, the definition of channel size following [Kandlikar, 2002] will be utilized for the framework of this project. A literature review of the state-of-the-art research on experimental and numerical approaches to two- and three-phase flows in micro- and mini-channels was conducted. The examination literature revealed that several numerical methods can be utilized to describe the flow and that experimental work using PMMA sheets with optical access give comparable results. However, the review also showed that further work on the subject can be performed. One of the challenges of VOF CFD modelling is its high computational requirements for a good accuracy. Furthermore, the model is also capable of predicting fluid flow phenomena like flow regimes. On the contrary, the Two-fluid model is a quicker numerical approach, which give relatively good accurate results on average values for the fluid flow, like e.g. void fractions, at a lower computational cost. Thus, this thesis will focus on investigating the numerical accuracy of the Two-fluid model against VOF modelling compared to the computational costs of the model. This is done to proper determine if the Two-fluid model can be satisfactorily used for two-phase flow modelling in future studies. The numerical work will

be compared against the experimental work made concurrent. The geometry chosen for numerical and experimental work, on two-phase flow fields, will be a Plexiglas T-junction, where water and air will be used as the working fluids. The fluids are chosen as their properties are well-known and easily attainable. Furthermore the geometry is simple and does not require advanced experimental features to function properly and the numerical domain for the simulation can be meshed relatively easily. Previously one of the authors of [Olesen et al., 2016] compared the results of the article by [Bi and Zhao, 2001] in a flow regime map. The flow regime map can be seen in figure 1.7.

Based on the following flow regime map a working range of the superficial velocities of the fluids have been determined to be within the interval of $4 \text{ m/s} \geq V_L \geq 3 \cdot 10^{-2} \text{ m/s}$ for the liquid regime and within the interval of $2 \text{ m/s} \geq V_G \geq 2 \cdot 10^{-2} \text{ m/s}$ for the gas regime.

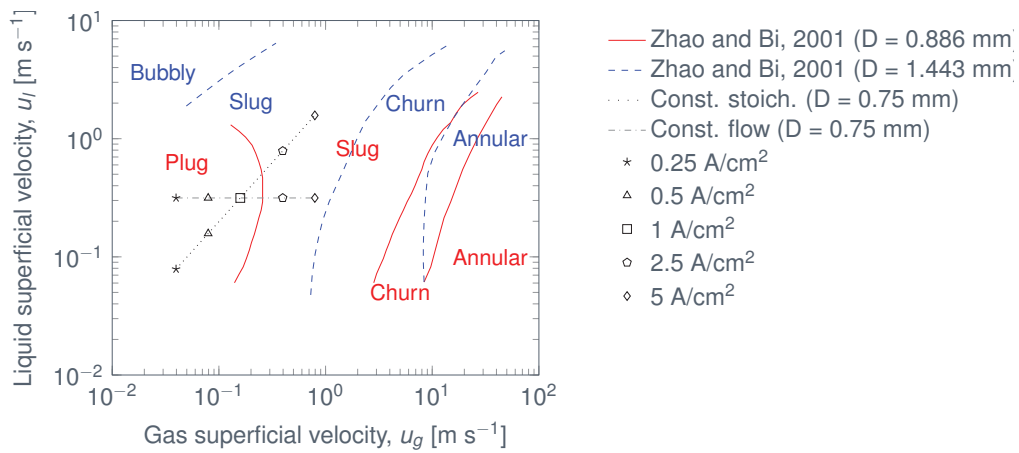


Figure 1.7: A comparison of two-phase flow regime maps of different size and operating conditions for vertical micro/mini-channels. Used with accept from one of the authors of [Olesen et al., 2016].

In the following a more in-depth description of the chosen geometry, scenario calculation and experiment will be presented.

1.3 Geometry of cell and mini-channel

To reduce the computational domain and ensure comparability between CFD simulations and the experimental results, the inlet entry length of both phases have been calculated and will be used to design the physical cell and its mini-channels. The entry length (L_h) denotes the length needed from the inlet to a point at which the velocity profile of the 1-phase fluid is said to be fully developed. In the fully developed region the velocity profile of a laminar flow is parabolic, whereas it is much flatter for turbulent flow as a consequence of the intense mixing and eddy motion. By ensuring that the fluid flow in the inlets has reached fully developed flow before the T-junction, this velocity profile can be implemented in the CFD-simulation shortly before the T-junction and the length of the inlet channels in the CFD-simulation can be minimized.

The entry length is dependent on the diameter of the channel and the Reynolds number of the flow

and different approximations are applicable depending on whether the flow is laminar or turbulent:

$$\frac{L_{h,laminar}}{D} \cong 0.05Re \quad (1.2a)$$

$$\frac{L_{h,turbulent}}{D} \cong 10 \quad (1.2b)$$

As an effect of the intense mixing in turbulent flow, the entry length is much smaller than for laminar flow and for practical engineering purposes the effect of the entrance region becomes minimal after a length of about 10 diameters (ie. equation (1.2b)) - after which the velocity profile is fully developed [Cengel et al., 2017].

To accommodate the entry length approximations in equation (1.2) to non-circular pipes, the hydraulic diameter, D_h , is introduced as:

$$D_h = \frac{4A_c}{P_{wet}} \quad (1.3)$$

Where A_c is the cross-sectional area and P_{wet} is the wetted perimeter of the pipe. Equation (1.3) is interchanged with the diameter, D , in eq. (1.2) to estimated the entry length for non-circular pipes.

The transition from laminar flow to turbulent flow has been reported to occur around $Re_{cri} = 2300$ for conventional channels [Cengel et al., 2017] - i.e. $D_h > 3 \text{ mm}$ according to table 1.1. However, different values of the critical Reynolds number have been reported, e.g. [Agarwal et al., 2010] which found the transition to occur at $Re \approx 1100$ for a rectangular mini-channel with a hydraulic diameter of 0.907 mm ($1.1 \times 0.772 \text{ mm}$). In [Steinke and Kandlikar, 2006] the authors have reviewed 150 articles dealing with fluid flow and heat transfer in microchannels with range of Reynolds number from $0.002 < Re < 5000$ and a range of hydraulic diameter from $8 < D_h < 990 \mu\text{m}$. They concluded that papers which presented data with a deviation from theory also neglected to account for the developing flow and/or entrance and exit losses in the microchannel. The remaining papers of the review presented data which showed agreement with theory.

In [J. Schmitt and Kandlikar, 2005] the critical Reynolds number for flow transition from laminar to turbulent is investigated under different hydraulic diameters ranging from $325 \mu\text{m}$ to $1819 \mu\text{m}$ and under different surface roughness. The authors conclude that rectangular minichannels in the investigated hydraulic range with a relative surface roughness of $\varepsilon/D_h < 0.000375$ showed no indications of early transitions to turbulent flow and supported the critical Reynolds number of $Re = 2300$ from macro scale flow. However, as the relative roughness of the surfaces was increased the transition from laminar to turbulent flow showed considerable deviations and the critical Reynolds number was found to decrease. The transitions from laminar to turbulent flow was also reported to be unaffected as they hydraulic diameter was decreased.

Based on the critical Reynolds number of $Re = 2300$, equations (1.2a) and (1.2b) are used to calculate the entry lengths of the 1-phase inlets of water and air. The fluid properties for both water and air are shown in table 1.2 and the Reynolds number is expressed as:

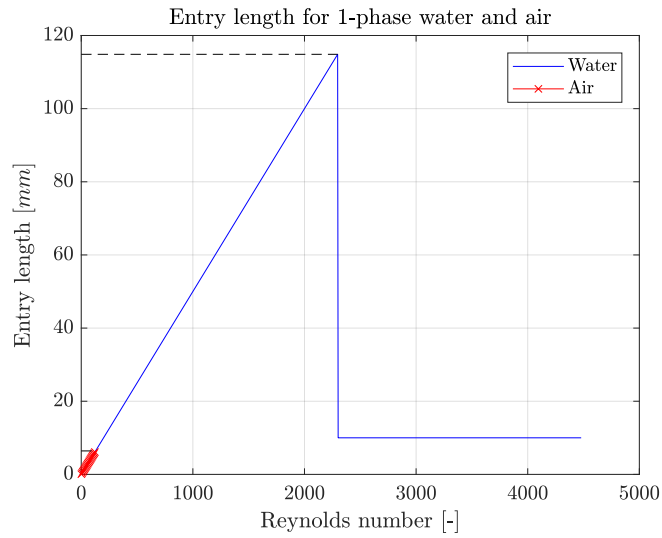
$$Re = \frac{\rho U D_h}{\mu} = \frac{U D_h}{\nu} \quad (1.4)$$

Where U is the fluid velocity, ρ is the fluid density, D_h the hydraulic diameter from equation (1.3), ν is the kinematic viscosity and μ is the dynamic viscosity of the fluid.

Table 1.2: Fluid properties for entry length estimations.

	T	P	ν	U -range
Air	25 °C	1 bar	$1.558 \cdot 10^{-5} \text{ m}^2 \text{ s}^{-1}$	0.02-2 m s^{-1}
Water	25 °C	1 bar	$8.931 \cdot 10^{-7} \text{ m}^2 \text{ s}^{-1}$	0.03-4 m s^{-1}

Figure 1.8 shows the calculated entry length for both water and air as a function of the Reynolds number, which again has been calculated using the velocity range for water and air specified in table 1.2

**Figure 1.8:** Entry length for water and air as as function of the Reynolds number.

From the graph the maximum entry length for water and air can be estimated to be $L_{h,w} = 115 \text{ mm}$ and $L_{h,g} = 6.41 \text{ mm}$. For water this corresponds to a Reynolds number of 2300 which is when the transition from laminar to turbulent occurs. Air never leaves the laminar region as the highest Reynolds number for air is around 128.

As the surface roughness of the plexiglass material is not known the transition from laminar to turbulent could potentially deviate from the critical Reynolds number of 2300. However, the two entry lengths will be used as reference to determine the length of the two inlet channels for water and air.

1.3.1 Scenario calculation

Based on the comparison flow regime map from the authors of [Olesen et al., 2016], intervals for the superficial velocities of the different fluids was set. This is used to set a base case which can be tested by the numerical models and experimental work. From figure 1.7 it is seen that liquid superficial velocities around 0.4 m/s and gas superficial velocities around 0.7 m/s should create a slug flow for all compared cases. Thus, this is chosen as the base case of the study. However, the

equipment used for setting inlet parameters of the different fluids, e.g. pumps and compressors, does not use the superficial velocity as a set point. Thus, these values have to be recalculated into equipment set points as the volume flow of the different faces. From the superficial velocities and knowledge of fluid properties of the different phases at a certain temperature the mass and volume flow of the different phases can be determined as:

$$\dot{m} = u \cdot \rho \cdot A_c \quad (1.5)$$

$$\dot{V} = \frac{\dot{m}}{\rho} \quad (1.6)$$

Using the equations above mass and volume flows for the base, maximum and minimum superficial velocities cases can be determined and the results of this are seen in table 1.3.

Table 1.3: Base, maximum and minimum Reynolds number and superficial velocities of gas and liquid phases for volume flow estimation @ 25 °C and a mini-channel cross area of $1 \cdot 10^{-6} \text{ m}^2$.

	u	ρ	\dot{m}	\dot{V}	Re
$u_{L,base}$	$0.4 \text{ m} \cdot \text{s}^{-1}$	$997.05 \text{ kg} \cdot \text{m}^{-3}$	$3.9928 \cdot 10^{-4} \text{ kg} \cdot \text{s}^{-1}$	$1.44 \text{ L} \cdot \text{hr}^{-1}$	448.08
$u_{G,base}$	$0.7 \text{ m} \cdot \text{s}^{-1}$	$1.1839 \text{ kg} \cdot \text{m}^{-3}$	$8.4287 \cdot 10^{-7} \text{ kg} \cdot \text{s}^{-1}$	$2.52 \text{ L} \cdot \text{hr}^{-1}$	44.6429
$u_{L,max}$	$4 \text{ m} \cdot \text{s}^{-1}$	$997.05 \text{ kg} \cdot \text{m}^{-3}$	$4 \cdot 10^{-3} \text{ kg} \cdot \text{s}^{-1}$	$14.40 \text{ L} \cdot \text{hr}^{-1}$	4481.12
$u_{G,max}$	$2 \text{ m} \cdot \text{s}^{-1}$	$1.1839 \text{ kg} \cdot \text{m}^{-3}$	$2.4082 \cdot 10^{-6} \text{ kg} \cdot \text{s}^{-1}$	$7.2 \text{ L} \cdot \text{hr}^{-1}$	127.55
$u_{L,min}$	$1 \cdot 10^{-1} \text{ m} \cdot \text{s}^{-1}$	$997.05 \text{ kg} \cdot \text{m}^{-3}$	$9.9821 \cdot 10^{-5} \text{ kg} \cdot \text{s}^{-1}$	$0.36 \text{ L} \cdot \text{hr}^{-1}$	112.02
$u_{G,min}$	$4 \cdot 10^{-2} \text{ m} \cdot \text{s}^{-1}$	$1.1839 \text{ kg} \cdot \text{m}^{-3}$	$4.8164 \cdot 10^{-8} \text{ kg} \cdot \text{s}^{-1}$	$0.144 \text{ L} \cdot \text{hr}^{-1}$	2.55

As seen from table 1.3 the base scenario is in the middle of the region of interest, which is between $14.4 \text{ L} \cdot \text{hr}^{-1} \geq \dot{V}_L \geq 0.36 \text{ L} \cdot \text{hr}^{-1}$ for the liquid phase and $7.2 \text{ L} \cdot \text{hr}^{-1} \geq \dot{V}_G \geq 0.144 \text{ L} \cdot \text{hr}^{-1}$ for the gas phase.

However, due to experimental constraints on the flow regulators of the liquid and gaseous phase, the liquid phase will be kept between $4 \text{ L} \cdot \text{hr}^{-1} \geq \dot{V}_L \geq 0.4 \text{ L} \cdot \text{hr}^{-1}$, which corresponds to superficial velocities of the liquid phase between $1.11 \text{ m/s} \geq V_L \geq 1.11 \cdot 10^{-1} \text{ m/s}$. The gaseous phase will be kept between $2.37 \text{ L} \cdot \text{hr}^{-1} \leq \dot{V}_G \leq 7.2 \text{ L} \cdot \text{hr}^{-1}$, which corresponds to superficial velocities of the liquid phase between $0.66 \text{ m/s} \leq V_G \leq 2 \text{ m/s}$. Based on the set restrictions, a new area of interest have been set from figure 1.7. The newly set operation area and the plotted base case is seen in figure 1.9.

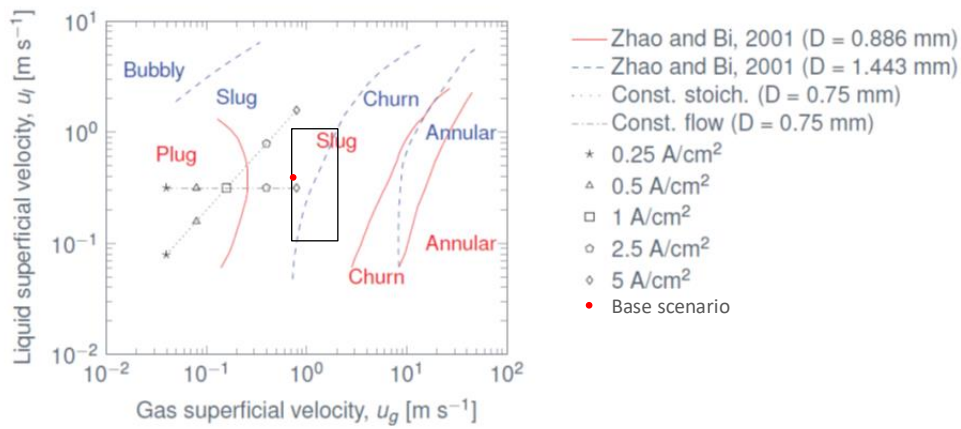


Figure 1.9: Two-phase flow regime map with mapped region of interest and case points [Olesen et al., 2016].

1.3.2 Experimental and Numerical geometry

In order to put the different numerical models into use, first a geometry of the test-setup needed to be setup. Based on the short review in chapter 1, a T-junction geometry have been chosen, as it is a simple, easy to draw, scaleable and fulfill the necessary requirements of two-phase flow mixing in mini-channels. As most numerical and experimental work on two-phase flow have been made on circular mini-channels, this thesis will instead focus on square mini-channels out of academic interest. Furthermore, square mini-channels should further simplify the meshing of the domain, as a structured hex mesh can be utilized across all faces of the geometry. Figure 1.10 show the proposed T-junction geometry for the experimental work of this thesis. Here water is fed from the bottom and air from the side and after the T-junction a two-phase flow emerge towards the outlet in the top. Due to the assumption of a fully developed flow explained in section 1.3, only a segment of the T-junction geometry is necessary for the setup of a numerical domain. Figure 1.11 show a segment of the proposed T-junction geometry for numerical work in OpenFOAM throughout this thesis.

Due to the complexity of the different numerical models and limitations imposed on ANSYS CFX for students, the Two-fluid model will be done using ANSYS CFX and the VOF modelling will be done using OpenFOAM. However as the programs use different interfaces, the meshing of the numerical geometry likewise follows different approaches, which will be described more in-depth in the following chapter.

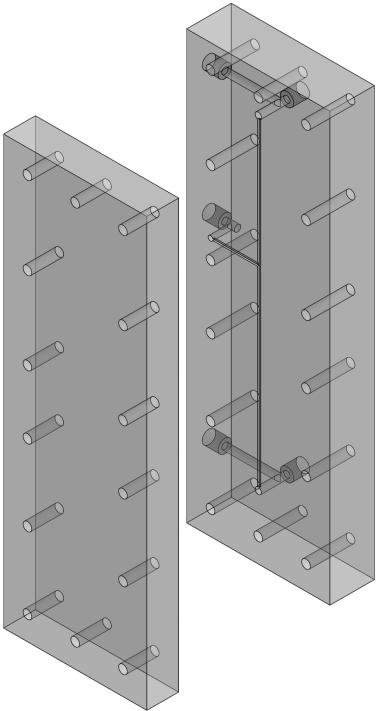


Figure 1.10: Geometry of T-junction for experimental work throughout the thesis.

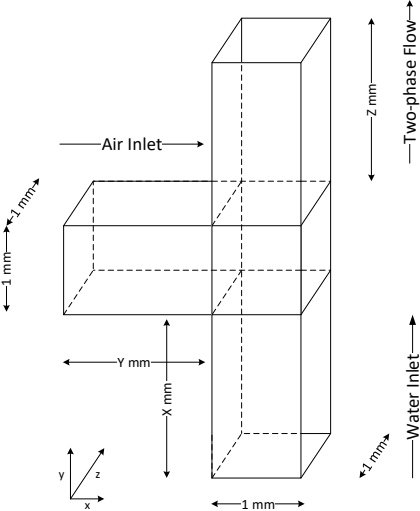


Figure 1.11: Segment of T-junction geometry for numerical work throughout the thesis.

Problem statement

Based on the topics covered in the preceding text, this chapter outlines the objectives of this thesis.

The main objective of this thesis will be to numerically and experimentally represent two-phase flows in mini-channels. As mentioned in chapter 1, scientific work on validation between experimental and numerical VOF and Two-fluid model work on mini-channels is lacking. Thus to gain further insight on CFD modelling of mini-channels a experimental and numerical approach will be examined. The purpose of this thesis will be to investigate the accuracy of available commercial CFD-codes, e.g. VOF and Two-fluid model, on two-phase flows in mini-channels compared against a experimental approach. This will be done using some general two-phase flow parameters, discussed further in the bottom of this chapter.

Some of the tasks needed to satisfactorily examine the purpose of the thesis, is described more in-depth in the following chapters. These include, among others, detailed descriptions of the theory behind the utilized numerical models and the experimental methodologies used for data acquisition. The detailed analysis of the utilized methodologies is done to form a basis of evaluation.

2.1 Parameters of validation between the models

In order to compare relations between the tested numerical models and the experimental work, different parameters of validations are examined. Among the most evident parameters of validation are the volume fractions, pressure loss across the channel and visual inspection of the bubble formation.

The volume fractions of gas and liquid in the mini-channel can be determined by both utilized numerical methods and image processing of the experimental work. However, due to a size constraint on the computational domain of the VOF-modelling and a visual size constraint on the camera used for the experiment, a limited section of 21 mm in the VOF modelling and 30 mm in the experiment after the T-junction can be modelled and inspected. Based on set sections, average values of the examined parameters will be determined.

By use of image processing operations the liquid phase of the two-phase flow can be subtracted from the taken images. Thus, leaving only the gaseous phase in the image. Hence, the area and volume fractions of bubbles can be determined and compared to the numerical work. The methodology behind image processing operations will be explained more in-depth in section 5.3.

In the VOF modelling, the volume fraction can be determined across planes and volumes inside the geometry as average values for a given time step, but also as averaged means of the examined time steps. As the VOF modelling is transient, this thesis will use the averaged means as a steady-state

solution for comparison with the Two-fluid modelling and experimental results.

As with the VOF modelling, the volume fractions in the Two-fluid modelling can be determined across planes and volumes inside the geometry as steady-state average values.

Pressure transducers in the experiment, determines the pressure loss across the channel length and both numerical models resolves the pressure drop across the mini-channel as well. However, due to computational demand, the calculated pressure loss in the VOF modelling will only be compared with the Two-fluid model. Thus, the pressure loss across is used as further grounds of validation between the numerical models and the Two-fluid model and the experimental results.

Visual inspection of the fluid regime and bubble formation is the last parameter, which will be used as a validation between the VOF-model and experiment. From the experiment, images of the fluid mixing and bubble formation is obtainable and can be directly compared with the VOF-modelling. Quantities like bubble length and shape is obtainable through image processing of the experiment and can also be determined in the VOF-modelling. As the Two-fluid model is not capable of resolving the interface between the fluids, this numerical model can not be used for validation of these patterns.

Numerical methodologies

This chapter presents the numerical methodology and setup used for the analysis of two-phase flow inside mini-channels. Throughout this chapter, the numerical background of VOF- and two-phase modelling for mini-channels will be presented. Furthermore, it will be presented how to utilize the Two-fluid model on a found geometry in the commercial available CFD program ANSYS CFX and the VOF-model in the open-source program OpenFOAM. Lastly, grid in-dependency studies of the numerical models will be conducted, in order to determine the necessary computational grid for numerical independence. In addition to grid in-dependency study of the Two-fluid model, a model study of the Two-fluid model will be conducted. This is done to determine how additional physics affect the Two-fluid model and its computational demand.

3.1 Computational Fluid Dynamics (CFD)

CFD is a numerical method for solving, among others, fluid dynamics and fluid mechanics problems and if utilized correctly a very powerful tool. The method can be based on several different numerical schemes like the finite element method (FEM) and finite volume method (FVM) and seeks to solve the governing equations of fluid flows, also known as the general transport equation, which is defined in equation (3.1). Here a general flow variable ϕ , e.g. a pressure component, is conserved and described within a finite CV (control volume) [Versteeg and Malalasekera, 2007].

$$\underbrace{\frac{\partial(\rho\phi)}{\partial t}}_{\text{Transient}} + \underbrace{\text{div}(\rho\phi\mathbf{U})}_{\text{Convective}} = \underbrace{\text{div}(\Gamma\nabla\phi)}_{\text{Diffusion}} + \underbrace{S_\phi}_{\text{Source}} \quad (3.1)$$

Here ρ is the density of the fluid, div is the divergence of the term, U is the velocity of the fluid, Γ is the diffusion, ∇ is the gradient and ϕ is the variable in question.

A typical CFD code consist of three basic parts: A pre-processor, a solver and a post-processor and operates as shown in the flowchart in figure 3.1.

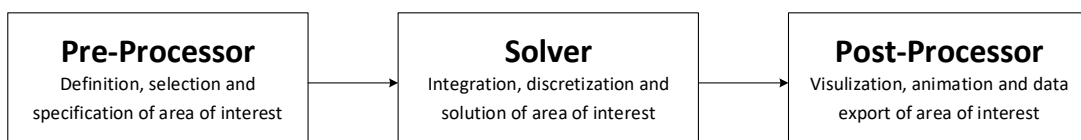


Figure 3.1: Flowchart of typical CFD code operation [Versteeg and Malalasekera, 2007].

As seen in the flowchart the pre-processor defines and specifies the input of the problem and transforms it into a solvable numerical problem. In this step the computational domain and geometry is set and discretized into smaller sub-domains known as grids or a mesh of cells. The amount of cells and their internal coherence has the largest influence on the total computational time of the domain. However, generally a higher amount of cells also increases the accuracy of the solution. Thus the crossover between accuracy and computational time is often of great importance and tested by a grid in-dependency study, which examines the accuracy of the solution against the mesh size.

Once defined the different boundary, inlet and outlet conditions surrounding the geometry is set. Furthermore the fluid properties of interest and physical phenomenons that are to be modelled are specified.

Following comes the solver. The solver sets the numerical scheme for the geometry, in most commercial CFD programs the FVM, and specifies additional models used on the fluid flow. The solver consists of integration, discretization and solution. First, equation (3.1) is integrated across each cell of the mesh. Next the integrated equations are discretised into a set of algebraic equations, which is solved using an iterative method to obtain a solution [Versteeg and Malalasekera, 2007].

Lastly the solution is loaded into the post-processor. The post-processor contains different data visualization tools, which create an overview of the results using vector contours and surface plots in 2D and 3D. If a transient solver is used, the post-processor can also make dynamic results as animations.

Accurate numerical work using CFD on two-phase flow in mini-channels can decrease experimental costs and give a deeper insight on the fluid dynamics and flow phenomenons occurring inside mini-channels and their effects. Thus a deeper insight in the VOF and Euler-Euler code will be described in the following sections.

3.1.1 Mesh quality parameters

The following section is written with a basis in [ANSYS].

The quality of the computational grid, also known as mesh, is of great importance for the solution accuracy and stability of the numerical model. Thus, regardless of the type of mesh, variables like the cell count, cell skewness and aspect ratio of the mesh are important indicators to check that the quality of the mesh is satisfactory. Hence the most used indicators will be described more in-depth in the following sections.

Orthogonal quality

The first important mesh quality variable is the orthogonal quality. The orthogonal quality of each cell in the mesh range between values 0-1 and is a measure of how well each cells fit to its neighboring cells. Thus, a cell with a perpendicular connection to its neighboring cells would obtain a perfect value of 1, whereas high angles between the cells would give a lower value. Both ANSYS and OpenFOAM have tools to determine the overall orthogonal quality of the mesh, which determines the orthogonal quality of each face using the following equation.

$$\text{Orthogonal quality} = \min \left(\frac{\overline{A}_i \cdot \overline{f}_i}{|\overline{A}_i| |\overline{f}_i|} , \frac{\overline{A}_i \cdot \overline{c}_i}{|\overline{A}_i| |\overline{c}_i|} \right) \quad (3.2)$$

In equation 3.2, \overline{A}_i is a normal vector to the face, \overline{f}_i is a vector pointing from the cell center to the middle of the cell face and lastly \overline{c}_i is a vector from the cell center to the center of an interconnected cell.

Aspect ratio

Next important mesh quality variable is the aspect ratio. The aspect ratio is a measure of the stretching of a cell. Thus, the aspect ratio is given as the ratio between the longest edge length of the cell to the short edge length of the cell. An ideal case for the aspect ratio is hard to determine, as it is the change in flow field gradients between the cells, which determine what is acceptable. Strong gradients require low aspect ratios, whereas low gradients allow for higher aspect ratios. For a simple geometry, like the T-junction, it can prove valuable at certain parts of the computational domain where no notable flow field changes occur, as it can reduce the needed number of cells in the mesh and computational work.

Cell Skewness

Cell skewness is an important mesh quality parameter as it describes the distortion between cells and is defined from the shape of the cell, compared to an equal-sided cell with equivalent volume. If a mesh have highly skewed cells it can diverge and decrease the accuracy of the solution. The skewness of the cells are calculated following equation 3.3.

$$\text{Skewness} = \max \left(\frac{\theta_{max} - \theta_e}{180 - \theta_e}, \frac{\theta_e - \theta_{min}}{\theta_e} \right) \quad (3.3)$$

Here θ_{max} is the largest angle of the cell, while θ_{min} is the smallest. θ_e is a normalized angle, which is 90° for quadrilaterals and 60° for triangles. The normalized angles are the reference to describe the degree of skewness of the cells. Typically high aspect ratios will affect the skewness of the cells, as they are stretched between each other. The range of skewness varies between 0-1, where 0 corresponds to a non skewed cell, while a skewness of 1 corresponds to a highly skewed cell. A general rule for the maximum skewness of a cell in the computational grid is below 0.95. However, the average value of the entire mesh should be well below this value and as close to 0 as possible for stability and accuracy of the computational grid. The spectrum for skewness mesh metrics can be seen in table 3.1.

Table 3.1: Skewness metrics for CFD practice [ANSYS].

Excellent	Very Good	Good	Acceptable	Bad	Unacceptable
0-0.25	0.25-0.50	0.50-0.80	0.80-0.95	0.95-0.97	0.97-1.00

For a simple geometry, like the T-junction, use of quadrilateral cells should render a low overall skewness of the mesh, as fixed cells with low aspect ratios should make relative clean angles between the cells.

Courant Number

The Courant number is a stability parameter of numerical work and is defined as a dimensionless quantity which compares the time step of the numerical scheme to the time it takes a fluid element

to move across a control volume. Thus it determines and set a boundary for a necessary condition of convergence for the utilized numerical scheme across the geometry. The formulation of the Courant number is shown in equation 3.4.

$$Co = \Delta t \cdot \sum_{i=1}^n \frac{u_x^i}{\Delta x_i} \leq Co_{max} \quad (3.4)$$

In equation 3.4 Δt is the time step, u is the velocity and Δx is the length of the control volume both in x,y,z -direction. Furthermore it is seen from 3.4 that it is the user who sets the upper limit of the Courant number. However, for simulations with eddy structures, as could be expected from the simulation of two-phase flows during its mixing, it is required to have a low Courant number ($Co \leq 1$) [Yin, 2016]. With a Courant number boundary imposed on the problem, the time step will self regulate in order to meet the criterion. Thus for high velocity or small cell problems, the time step will typically be low. The use of Courant number is something which have to be thought into the computational work of the thesis, as it could show to influence the computational work.

Near wall treatment of the T-junction geometry

For mini-channels it is known than the flow field will be dominated by surface tension effects. Thus, being able to accurately model the flow near the walls of the T-junction is important, as the walls significantly affects the boundary layer and gradients of the flow field. With no-slip conditions at the walls, the velocity is seen to increase from zero at the edge of the wall towards the free-stream velocity (U_0) in the middle of the channel. The near surface boundary layer, with its velocity profile can be seen in figure 3.2

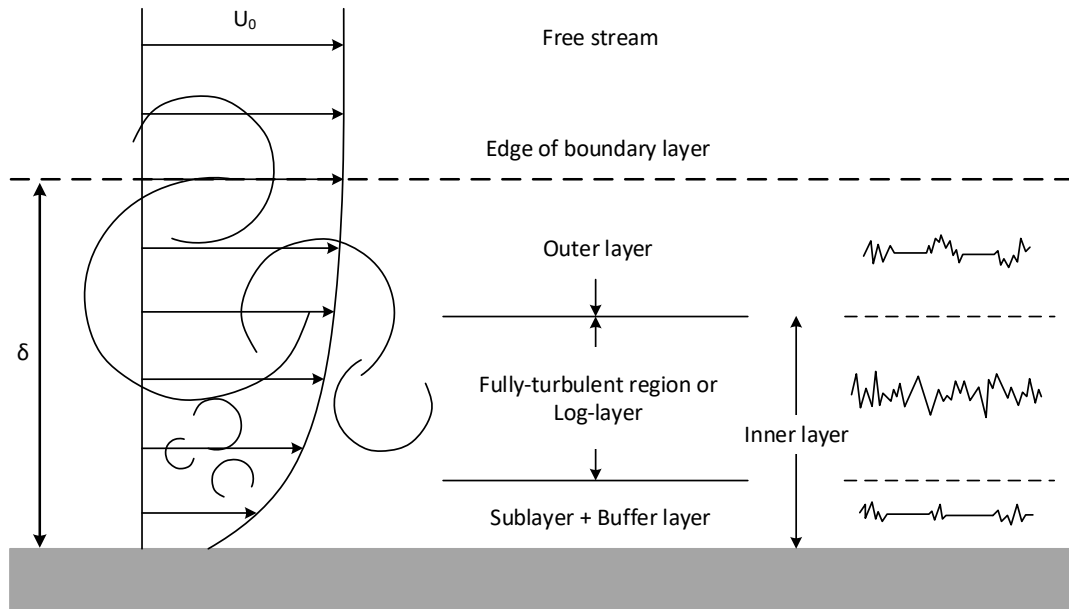


Figure 3.2: Boundary layer structure and velocity profile near the wall, U_0 is the free-stream velocity and δ is the boundary layer thickness. Made with inspiration from [Yin, 2016]

As seen in figure 3.2 the boundary layer can be split into three different regions, before reaching the free-stream velocity namely the viscous sublayer / buffer layer, the fully turbulent region and outer layer. In the viscous sublayer, turbulence is suppressed due to the shear stresses close to the wall, which strongly affect the velocity of the fluid. Moving away from the wall the shear stresses decreases and velocity starts to rise. As velocity increase more turbulence effects arise within the boundary layer. Here the turbulence will stir the different layers and eddie structures are seen within the flow. Throughout the fully-turbulent region the velocity is seen to increase. Throughout the outer layer the eddie structures increases in size but the overall turbulence of the flow decreases and the velocity of the flow increases [Versteeg and Malalasekera, 2007].

It should be noticed that the boundary layer height changes with the Reynolds number (Re). Thus, the height from the wall surface to the nodal point of the first cell (y), does not necessarily tell or resolve information about the region it is placed in. Instead a dimensionless distance y^+ can be used to determine the dimensionless height of the first cell and is defined in equation 3.5 and seen in figure 3.3.

$$y^+ = \frac{y \cdot \rho \cdot u_\tau}{\mu} \quad (3.5)$$

In equation 3.5 u_τ is the wall friction velocity, which is further defined as:

$$u_\tau = \sqrt{\frac{\tau_w}{\rho}} \quad (3.6)$$

Here τ_w is the wall shear stresses.

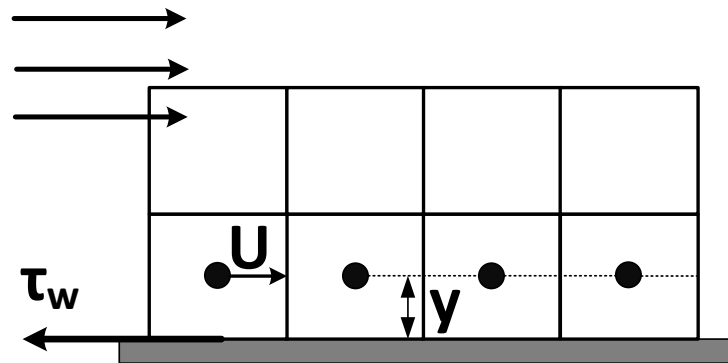


Figure 3.3: Grid profile near the wall and its definitions. Made with inspiration from [Yin, 2016]

Near-wall modelling options

CFD modelling near the walls of the channels can operate from the two different options, namely Wall Functions (WF) and Enhanced Wall Treatment (EWT). An overview of how the two different models operate can be seen in figure 3.4.

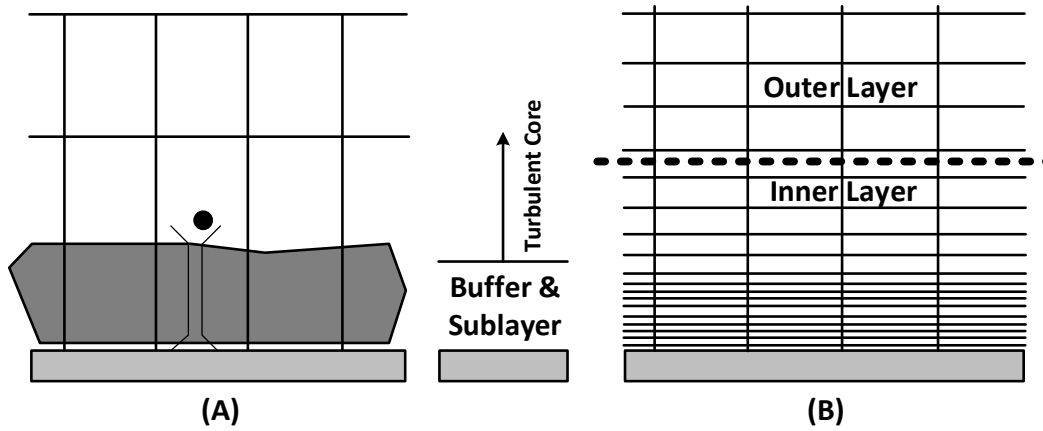


Figure 3.4: Overview of how the different wall functions operate. A is the Wall Function (WF) and B is the Enhanced Wall Treatment (EWT). Made with inspiration from [Yin, 2016]

As seen from the figure 3.4 (A) shows the WF and (B) shows the EWT. WF is often used when the focus of the computational work are mixing in the middle of the domain, rather than fluid dynamic occurrences at the walls. Thus, WF are used when the computational grid near the wall is ($y^+ \geq 5$) and the near wall modelling transitions from the viscous sublayer to the buffer layer $30 \leq y^+ \leq 5$ [Von karman, 1931]. EWT combines a two-layer model with an enhanced wall function and divides the boundary layer into a turbulent and laminar part. Thus, if the computational grid near the wall is fine enough, the EWT is able to resolve the viscous sub-layers. However, the use of EWT also imposes larger computational requirements, as the computational grid needs to be sufficiently fine near the wall ($y^+ \leq 5$). EWT is especially advantageous in low Re- and complex near-wall phenomena flows, as it give more accurate estimations of the flow parameters near the walls [ANSYS]. Inside the buffer layer, the subjecting law of the walls correlations, which both the WF and EWT is based on, have some uncertainties which potentially can induce errors on the estimation of the numerical work. This is due to a change in correlation describing the frictional velocity. However, as the utilized functions average across the numerical calculation, this should not induce a large potential error on the results.

The definition of y^+ and its usage in near wall modelling will conclude the study of mesh quality parameters. Throughout the numerical work of this thesis, the above described parameters will be utilized as a measure of sufficient CFD quality/practice [Yin, 2016].

3.1.2 Modelling of multi-phase flow

When modelling the complex nature of a multi-phase flow, there are currently two approaches available; namely the Euler-Lagrange approach and the Euler-Euler. In the Euler-Lagrange approach the dispersed fluid particles is marked and tracked through the fluid phase. The particles position, velocity and other parameters are then described as a function over time. This approach is simplified if it is possible to neglect the particle-particle interactions, however this assumptions only holds if volume fraction of the dispersed phase is low (i.e $\leq 10\%$) [ANSYS].

In the Euler-Euler approach a control volume is identified and the governing equation is solved at each of these control volumes. The pressure, velocity and other fluid flow properties is then given as fields and they are then described as a function over time and space. Compared to the Euler-Lagrange approach the Euler-Euler approach is not concerned with the location and velocity of an individual particle, but rather with any particle's properties at an given location (here control volume) at an given time. In the Euler-Euler approach the different phases of the multiphase flow are evaluated as an interpenetrating continua and the volume fraction concept of phases is utilized, as the volume of a phase cannot be filled by the other phases. The sum of the volume fractions is equal to one and, as with the other fluid properties, they are considered to a be continuous function of time and space [ANSYS; Stenmark, 2013].

Apart from the surface tension between the participating phases, the wall adhesion phenomenon also occurs as a result of the forces between the molecules of a liquid and the molecules of a solid which forms a adhesion between them. Whenever the cohesion forces among the liquid molecules is smaller then the adhesion forces, the liquid molecules gathers toward the wall and creates a contact area between liquid and solid, which tends to increase as the difference between cohesion and adhesion forces increases - and vice versa. At fluid interfaces in contact with the solid, the wall adhesion effects is estimated by introducing a term called *contact angle*, θ_w , into the two-phase modelling framework. The contact angle is estimated as the angle between the tangent to the fluid interface and the wall, where it is measured from inside the fluid - see figure 3.5 [Yeoh, 2010].

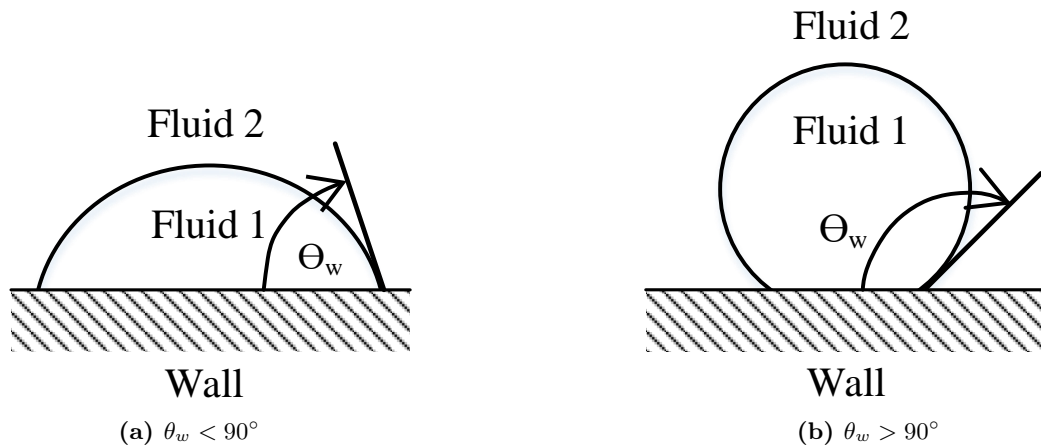


Figure 3.5: Contact angles between the fluid and wall [Bracco and Holst, 2013]

When the contact angle is $\theta_w < 90$ deg the fluid wets the wall with a large contact area. As the contact angle increases the contact area decreases and at $\theta = 90^\circ$ the fluid interface is normal to the wall. The contact angle depends on the surface roughness of the wall and the nature of the fluid in contact with the wall and it is usually determined experimentally.

As the combination of superficial velocities for the gas and liquid phase are situated around the slug- and plug-flow, see figure 1.7, large volume fractions are expected and the Euler-Lagrange approach will be disregarded and focus will be on the Euler-Euler framework and specifically the Two-fluid model and Volume-Of-Fluid model.

Two-Fluid Flow Model

First numerical methodology of interest is the Two-fluid method. The Two-fluid multi-phase model simulates bubbles or droplets of a secondary phase, which is dispersed in the primary continuous fluid phase, by treating each phase as continuous following the Euler-Euler methodology.

The Two-fluid model allows for interpenetration between the phases and solves the momentum, energy and continuity equations for each phase separately, while tracking the volume fractions. The volume fractions are modelled as a part of the transport equations such that the sum of all phases within the flow are 1. Thus, the phase equations are averaged across each control volume to achieve the mean fields of the two-phased flow. Through shared pressure and inter-phase exchange coefficients of the phases a coupling between them is reached [Stenmark, 2013].

The continuity, momentum and enthalpy equations respectively are given in equation 3.7, 3.8 and 3.9.

$$\frac{d}{dt}(\alpha_q \cdot \rho_q) + \nabla \cdot (\alpha_q \cdot \rho_q \cdot \vec{V}_q) = \sum_{p=1}^n (\dot{m}_{pq} - \dot{m}_{qp}) + S_q \quad (3.7)$$

In the continuity equation, equation 3.7, α is the volume fraction, ρ is the density, V is the velocity vector, \dot{m} is the mass transfer and S is the source term of the given phase q or p and subscripts qp indicate a transfer from phase q to p. The continuity equation handles the conversation of mass transfer between the fluids of flow.

$$\begin{aligned} \frac{d}{dt}(\alpha_q \cdot \rho_q \cdot \vec{V}_q + \nabla \cdot (\alpha_q \cdot \rho_q \cdot \vec{V}_q \cdot \vec{V}_q) = -\alpha_q \cdot \nabla P + \nabla \cdot \bar{\tau}_q + \alpha_q \cdot \rho_q \cdot \vec{g} \\ + \sum_{p=1}^n (\vec{R}_{pq} + \dot{m}_{pq} \cdot \vec{V}_{pq} - \dot{m}_{qp} \cdot \vec{V}_{qp}) + (\vec{F}_q + F_{lift,q} + F_{wl,q} + F_{vm,q} + F_{td,q}) \end{aligned} \quad (3.8)$$

In the momentum equation, equation 3.8, ∇P is the pressure gradient of the phases, $\bar{\tau}$ is the phase stress-strain tensor, \vec{g} is the gravitational velocity vector, \vec{R} is the interaction forces between the phases, which, among others, depends on pressure and friction, and lastly is used to describe different forces acting on the flow, like lift - and virtual mass forces. The momentum equations handles the conservation of momentum for the multi-phase flow.

$$\begin{aligned} \frac{d}{dt}(\alpha_q \cdot \rho_q \cdot h_q) + \nabla \cdot (\alpha_q \cdot \rho_q \cdot \vec{U}_q \cdot h_q) = \alpha_q \cdot \frac{dP_q}{dt} + \bar{\tau} : \nabla \vec{U}_q - \nabla \cdot \vec{q}_q \\ + S_q + \sum_{p=1}^n (Q_{pq} + \dot{m}_{pq} \cdot h_{pq} - \dot{m}_{qp} \cdot h_{qp}) \end{aligned} \quad (3.9)$$

Lastly in the enthalpy equation, equation 3.9, h is the enthalpy, \vec{q} is a heat flux vector and Q_{pq} is the intensity of heat exchange between the phases. The enthalpy equation ensures that the heat exchange between the different phases. These are the basic equations solved in the Two-fluid model and is the most simplistic way of modelling two-phased flows.

However, the Two-fluid model can be expanded, according to the flow conditions, to include additional physics, which better capture the fluid dynamics of the multi-phase flow. However, the additional physics also increase the computational efforts of the model, though not to the same degree as the VOF-modelling. For this thesis, the basic Two-fluid model is gradually expanded

with buoyancy, turbulence and fluid pair models, e.g. interphase transfer and momentum transfer forces, to examine how these different models affect the results of the multi-phase fluid flow. The set cases can be seen in table 3.2. Furthermore, the increase in computational effects will be discussed against the accuracy of the solution.

The buoyancy model is introduced to examine how gravitational forces affect the fluid flow and mixing. The buoyancy model induces a source term on the momentum equation, which is defined as [ANS, 2006]:

$$S_{M,buoy} = (\rho - \rho_{ref}) \cdot g \quad (3.10)$$

Where ρ_{ref} is the density of the continuous fluid and the density difference determine the gravitational effects on the multi-phase flow. When the buoyancy model is active, the absolute pressure is furthermore affected as the hydrostatic pressure gradient gets precluded from the momentum equation. Thus the absolute pressure is given as:

$$P_{abs} = P + P_{ref} + \rho_{ref} \cdot g \cdot (r - r_{ref}) \quad (3.11)$$

Where r and r_{ref} is locations inside geometry.

Turbulence models are introduced to examine the degree of turbulence effects from the Reynolds number of the fluid flow and the mixing of the fluids. As turbulence effects become more significant at high Reynolds number flows and the tested scenarios are in the laminar or close to turbulence region flows, Reynolds induced turbulence effects are not expected to highly influence the multi-phase flow. However, turbulence effects due to mixing of the fluids are unknown and could be interesting to examine. Thus, turbulence models are included as a part of the last two cases of the Two-fluid modelling.

Following a short literature study on the available turbulence models, the Shear-Stress Transport (SST) $k - \omega$ model have been chosen for the turbulence modelling in this thesis. The model was chosen above the k-epsilon model, due to its higher robustness, accuracy in the near-wall region and far-field region and its reliability across a wider range of fluid flow. The SST $k - \omega$ turbulence model solves the two transport equations given as:

$$\frac{d}{dt}(\rho \cdot k) + \frac{d}{dx_i}(\rho \cdot k \cdot U_i) = \frac{d}{dx_j} \cdot \left(\Gamma_k \cdot \frac{dk}{dx_j} \right) + G_k - Y_k + S_k \quad (3.12)$$

In equation 3.12, ρ is the density of the fluid and k is the turbulence kinetic energy, U_i is the velocity in the i^{th} direction, Γ is the effective diffusivity of k , G_k is the formed turbulence kinetic energy, Y_k is the dissipation of k and S_k is a user-defined source term. The k-equation solves the

Table 3.2: Overview of added physics in case modelling.

Case	Bouyancy	SST	Drag	Lift	Virtual Mass	Wall Lubrication.	Turbulent Dispersion	Sato
Base	X	X	X					
Case 1	X	X	X	X	X			
Case 2	X	X	X	X	X	X	X	
Case 3	X	X	X	X	X	X	X	X

formation of turbulence kinetic energy throughout the computational domain.

$$\frac{d}{dt}(\rho \cdot \omega) + \frac{d}{dx_j}(\rho \cdot \omega \cdot U_j) = \frac{d}{dx_j} \cdot \left(\Gamma_\omega \cdot \frac{d\omega}{dx_j} \right) + G_\omega - Y_\omega + D_\omega + S_\omega \quad (3.13)$$

In equation 3.13 several variables recur. However, the turbulence kinetic energy is exchanged with the specific dissipation rate ω , which describes how the produced turbulence kinetic energy is dispersed in the multi-phase fluid flow as thermal energy. Furthermore, the cross-diffusion term D_ω is added to the equation.

Fluid pair models are also included in the Two-fluid model. Fluid pair models are used to resolve how a continuous fluid, e.g. water, interact with a dispersed fluid, e.g. air. The fluid pair models cover additional physics, like drag laws. Furthermore a interface model between the two fluids are set. Here the particle model is chosen as the air is dispersed into the water flow in the mini-channel. The particle model assumes spherical particles of the dispersed phase, in order to calculate the interphase contact area for the interfacial transfer of momentum between the phases. The interphase contact area is given as [ANS, 2006]:

$$A_{w,a} = \frac{6 \cdot \alpha_w}{d_w} \quad (3.14)$$

In equation 3.14 α_w is the volume fraction of water and d_w is the mean diameter of water particles, in this thesis defined as 0.25 mm.

In order to properly examine the momentum and turbulence transfer effects drag/lift, virtual mass, wall lubrication, turbulent dispersion and Sato enhanced Eddy viscosity forces are gradually included in the Two-fluid model. These are gradually added to determine their influence on the results of the multi-phase fluid flow in the mini-channel.

Due to the low Reynolds number fluid flow scenarios the Schiller and Neumann model have been chosen as drag model for the Eulerian simulation. The Schiller and Neumann model determines the drag coefficient on the particles based on the Reynolds number of the flow as:

$$C_D = \max\left(\frac{24}{Re} \cdot (1 + 0.15 \cdot Re^{0.687}), 0.44\right) \quad (3.15)$$

Where the first formulation is used for Reynold flow < 1000 and $0.44 > 1000$.

The lift forces on the two phases is calculated following the Tomiyama lift force model as it is functional in the expected flow regimes of slug and plug. The Tomiyama lift force model is based on the Eötvös number and defines the lift coefficient as following:

$$C_L = \min[0.288 \cdot \tanh(0.121 \cdot Re_p, f(Eo'))] Eo' \leq 4 \quad (3.16)$$

$$f(Eo') 4 < Eo' \leq 10$$

$$-0.2710 < Eo'$$

Where Eo' is a modified Eötvös, including the long axis of the deformed bubble and $f(Eo')$ is a function given as:

$$f(Eo') = 0.00105 \cdot Eo'^3 - 0.0159 \cdot Eo'^2 - 0.0204 \cdot Eo' + 0.$$

The virtual mass force is furthermore added to the model with a standard value of 0.5 for inviscid flow around isolated spheres to model its effect in mini-channels.

The wall lubrication force models the forces induced on the dispersed phase when it gets pushed away from the wall of the mini-channel. Here the Tomiyama model is utilized due its dependence of channel diameter, surface tension coefficient and Eötvös number. The Tomiyama model gives the wall lubrication force coefficient as:

$$C_{WL} = C_W \cdot (Eo) \cdot \frac{d_p}{2} \cdot \left(\frac{1}{y_W^2} - \frac{1}{(D - y_W)^2} \right) \quad (3.17)$$

Where C_W is a coefficient depending on the Eötvös number, d_b is the diameter of the bubble, y_w is the distance to the nearest wall and D is the diameter of the pipe.

The turbulent dispersion force handles the interphase turbulent momentum transfer between the fluids and acts on the dispersed phase of the fluid flow. Throughout the thesis the Favre averaged drag model is used to model this force and is based on a weighted average of the interphase drag force, set as 1 in the modelling [ANS, 2006].

Lastly the Sato Enhanced Eddy Viscosity model is used to model the particle induced turbulence between the phases. The model is given as:

$$\mu_{tc} = C_{\mu p} \cdot \rho_c \cdot r_p \cdot d_p \cdot |U_d - U_c| \quad (3.18)$$

Where μ_{tp} is a particle induced Eddy viscosity, $C_{\mu p}$ is a constant of value 0.6, $|U_d - U_c|$ is the relative velocity between the phases, r_p is the particle diameter and ρ_c is the density of the fluid flow.

Volume of Fluid Model

As the VOF model treats all phases as continuous it belongs under the Euler-Euler approach, but compared to the Two-Phase flow model it does not let the phases be interpenetrating. Instead the VOF model is a surface-tracking routine and is designed to track the interface between two or more immiscible fluids.

The VOF model solves a single set of continuity (eq. 3.19) and momentum equations (eq. 3.21), where the pressure and velocity fields are shared by all participating fluids, along with an transport equation (eq. 3.20) for the phasic volume fraction, which makes it possible to track the volume fraction of the phases and the potential fluid interface in each control volume throughout the computational domain [ANSYS; Damián, 2012].

$$\nabla \cdot \mathbf{U} = 0 \quad (3.19)$$

$$\frac{\partial \alpha}{\partial t} + \nabla \cdot (\mathbf{U}\alpha) = 0 \quad (3.20)$$

$$\frac{\partial(\rho\mathbf{U})}{\partial t} + \nabla \cdot (\rho\mathbf{U}\mathbf{U}) = -\nabla p + \nabla \cdot \mathbf{T} + \rho\mathbf{f}_b \quad (3.21)$$

The volume fraction, α , is equal to 1 if a cell is fully occupied of phase 1 and equal to 0 if the cell is fully occupied of phase 2. Cells that contain the interface will take values within the range of $0 < \alpha < 1$, depending on the distribution of each phase within that cell.

Throughout equations 3.19-3.21 \mathbf{U} denotes the velocity vector, \mathbf{g} is the gravity vector, ρ is the density, p is the pressure and \mathbf{f}_b are body forces, which in VOF simulations involve effects of surface tension at the phase interface and gravity. The viscous stress tensor is denoted as \mathbf{T} (eq. 3.22a) with a mean rate of strain tensor \mathbf{S} (eq. 3.22b) and $\mathbf{I} \equiv \delta_{ij}$ as the identity matrix [Damián, 2012].

$$\mathbf{T} = 2\mu\mathbf{S} - \frac{2}{3}\mu(\nabla \cdot \mathbf{U})\mathbf{I} \quad (3.22a)$$

$$\mathbf{S} = \frac{1}{2}[\nabla\mathbf{U} + (\nabla\mathbf{U})^T] \quad (3.22b)$$

Assuming that both fluids are Newtonian and incompressible ($\nabla \cdot \mathbf{U} = 0$) the viscous stress tensor, \mathbf{T} , can be simplified to:

$$\begin{aligned} \mathbf{T} &= 2\mu\left(\frac{1}{2}[\nabla\mathbf{U} + (\nabla\mathbf{U})^T]\right) - \cancel{\frac{2}{3}\mu(\nabla \cdot \mathbf{U})\mathbf{I}}^0 \\ &= \mu[\nabla\mathbf{U} + (\nabla\mathbf{U})^T] \end{aligned} \quad (3.23)$$

As the VOF method/model considers the participating fluids as one fluid throughout the computational domain, the fluid properties in eq. 3.21 and 3.23 are calculated as weighted averages on the volume fraction. For example in a two-phase gas-liquid flow this corresponds to:

$$\rho = \alpha\rho_l + (1 - \alpha)\rho_g \quad (3.24a)$$

$$\mu = \alpha\mu_l + (1 - \alpha)\mu_g \quad (3.24b)$$

Where the subscripts l and g corresponds liquid and gas. This also ensures that the density and viscosity only varies across the interface and that they attain the corresponding liquid or gas properties, if the control volume only contains either of the fluids, i.e. $\alpha = 1$ or $\alpha = 0$.

In flows with a large difference in fluid densities, the conservation of the phasic volume fraction is a important subject as even small deviations in the volume fraction can result in considerable errors in the computation of the physical properties as density and viscosity. Accurate computation of the volume fraction is also important when the surface curvature of the interface is evaluated, as this greatly influences the surface tension force and the related pressure gradient across the phase interface [Berberović et al., 2009].

Typically the fluid interface is only spread over a few grid cells and the sharp interface can be difficult to capture properly by the tracking method - figure 3.6 shows a example on how the interface can be insufficiently tracked.

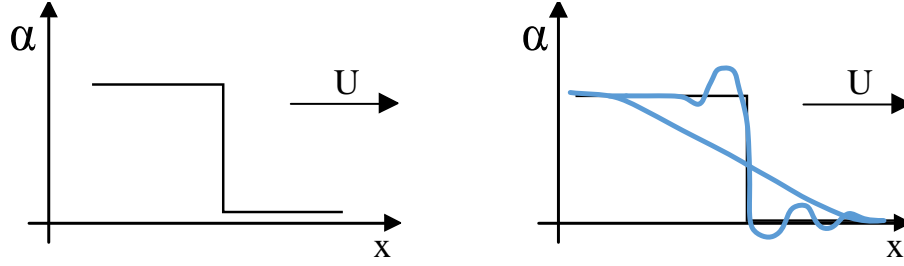


Figure 3.6: Example of numerical problems related to a sharp jump in the volume fraction, [Landet and Ridder, 2014].

The OpenFOAM `interFoam` solver utilizes an approach proposed in [Weller, 2008], where an additional convection term is introduced in the transport equation in order to contribute towards a sharper interface resolution. By assuming that the effective fluid velocity vector can be modelled as a weighted average of the corresponding volume fraction (eq. 3.25)

$$\mathbf{U} = \alpha \mathbf{U}_l + (1 - \alpha) \mathbf{U}_g \quad (3.25)$$

The derivation of the added convection term is then based on the approach of the Two-Fluid Flow model, where the phasic volume fraction is solved individually for each phase - replicated here in eq. 3.26.

$$\frac{\partial \alpha}{\partial t} + \nabla \cdot (\mathbf{U}_l \alpha) = 0 \quad (3.26a)$$

$$\frac{\partial (1 - \alpha)}{\partial t} + \nabla \cdot [\mathbf{U}_g (1 - \alpha)] = 0 \quad (3.26b)$$

Utilizing eq. 3.25 and 3.26, the transport equation (eq. 3.20) can be rearranged to eq. 3.27 with the added convection/advection term.

$$\frac{\partial \alpha}{\partial t} + \nabla \cdot (\mathbf{U} \alpha) + \nabla \cdot [\mathbf{U}_c \alpha (1 - \alpha)] = 0 \quad (3.27)$$

The additional term is called the *compression term* and its role is to ensure and maintain a sharp interface between the phases. Its an artificial term and, despite its name, it got no relation to the compressibility of the flow - it is merely a name. The term $\alpha(1 - \alpha)$ ensures that the compression term is only active within the interface region and that it vanishes in cells with only one phase.

The compression velocity, U_c , is an artificial interface velocity and is calculated as:

$$\mathbf{U}_c = \min(C_\alpha |\mathbf{U}|, \max(|\mathbf{U}|)) \mathbf{n} \quad (3.28)$$

Where $\mathbf{n} = \nabla \alpha / |\nabla \alpha|$ is the unit normal vector for the interface and the coefficient, C_α , is the user-adjusted parameter used to control the effect of the interfacial sharpening. The magnitude of the local velocity, $|\mathbf{U}|$, is used in the calculation of the compression velocity, as the dispersion of the phase interface (which the compression velocity is counteracting) can only happen as fast as the local velocity itself. If the coefficient C_α is restricted to $C_\alpha \leq 1$, equation 3.28 reduces to:

$$\mathbf{U}_c = C_\alpha |\mathbf{U}| \frac{\nabla \alpha}{|\nabla \alpha|} \quad (3.29)$$

and C_α now switches the interface on or off [E. Wardle and G. Weller, 2013].

The effects of the surface tension at the liquid-gas interface is an pressure gradient across the interface, which appears as a extra force in the momentum equation (eq. 3.21). The calculation of the additional force is based on the contiuum surface force (CSF) model [Brackbill et al., 1992]:

$$\mathbf{f}_s = \sigma \kappa \nabla \alpha \quad (3.30a)$$

$$\kappa = -\nabla \cdot \mathbf{n} \quad (3.30b)$$

where σ is the surface tension coefficient, κ is the mean curvature of the free surface and \mathbf{n} is the unit normal to the surface. Equations 3.30 are only applicable when the surface tension at the interface is constant and not with a variable distributed surface tension, as a surface tension gradients will give rise to extra shear stresses at the phase interface.

To account for the wall adhesion between the liquid and the wall (illustrated in 3.5), the contact angle, θ_w is specified in the calculations and this expected angle between the gas-liquid interface and the wall is then modified to the unit surface normal in cells neighbouring the wall. In the framework of the CSF-model by [Brackbill et al., 1992] the unit normal to the interface surface, \mathbf{n} , can be defined at the wall to account for the wall adhesion as:

$$\mathbf{n} = \mathbf{n}_w \cos \theta_w + \mathbf{t}_w \sin \theta_w \quad (3.31)$$

where \mathbf{n}_w is the unit normal vector to the wall and \mathbf{t}_w is the unit tangential vector pointing towards the fluid [Yeoh, 2010].

The pressure term on the r.h.s of the momentum equation (eq. 3.21) is often interchanged with a modified pressure term in order to simplify the pressure boundary conditions. The modified pressure is defined as:

$$p^* = p - \rho \mathbf{g} \cdot \mathbf{x} \quad (3.32)$$

The gradient of the modified pressure is then given as:

$$\begin{aligned} \nabla p^* &= \nabla p - \nabla(\rho \mathbf{g} \cdot \mathbf{x}) \\ &= \nabla p - \mathbf{g} \cdot \mathbf{x} \nabla \rho \end{aligned} \quad (3.33)$$

where \mathbf{g} is the gravity vector and \mathbf{x} is the position vector [Rusche, 2012]. The momentum equation is then rearranged (with eq. 3.23, 3.30a and 3.33) to read:

$$\frac{\partial(\rho \mathbf{U})}{\partial t} + \nabla \cdot (\rho \mathbf{U} \mathbf{U}) = -\nabla p^* + \nabla \cdot (\mu[\nabla \mathbf{U} + (\nabla \mathbf{U})^T]) - \mathbf{g} \cdot \mathbf{x} \nabla \rho + \sigma \kappa \nabla \alpha \quad (3.34)$$

The mathematical model is then given by the continuity equation (eq. 3.19), the transport equation for the phasic volume fraction (eq. 3.27) and the rearranged momentum equation (eq. 3.34).

The OpenFOAM multiphase solvers use a adaptive time step control in order to manage changing velocities in the computational domain and to achieve stability of the solution procedure calculations. The self-adapting time step is based on the Courant number and adapted at the beginning

of the time iteration. The local Courant number at a cell face is defined as:

$$Co = \Delta t \frac{\mathbf{U}_f \cdot \mathbf{S}_f}{\mathbf{d} \cdot \mathbf{S}_f} \quad (3.35)$$

where Δt is the timestep and \mathbf{d} is a vector between the calculation points of two control volumes which are sharing a face - e.g $\mathbf{d} = \overline{PN}$ in fig 3.7. The subscript f implies the value of the variable (here the velocity vector \mathbf{U}) in the middle of the shared face and S_f is the face area vector which is outward-pointing from P , if f is owned by P [Damián, 2012].

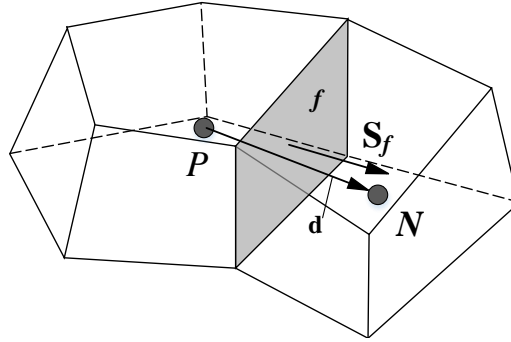


Figure 3.7: A control volume and its neighbouring volume where the shared face, f , is showed in grey [Berberović et al., 2009]

With values of U_f and Δt from a previous time step the local maximum Courant number, Co^0 , is calculated and the new time step is then determined from the expression in eq 3.36:

$$\Delta t^n = \min \left\{ \frac{Co_{max}}{Co^0} \Delta t^0, \left(1 + \lambda_1 \frac{Co_{max}}{Co^0} \right) \Delta t^0, \lambda_2 \Delta t^0, \Delta t_{max} \right\} \quad (3.36)$$

Where Co_{max} and Δt_{max} are user-defined limit values for the time step and Courant number and λ_1 and λ_2 are damping factors to avoid instability caused by time step oscillations. This ensures a smooth adjustment of the new time step and keeps the local maximum Courant number around the predefined target value [Rusche, 2012].

3.1.3 Configuration of mesh and solver in ANSYS CFX

ANSYS CFX is a solver which emanates from the ANSYS Workbench. The ANSYS Workbench have integrated solvers, geometry and meshing functionality for creating various applications. The CFX solver differs from the other solvers, as the user can define its own equations, for instance on drag laws. As for this thesis, the experimental and numerical investigation are done through inspection of two-phase flow parameters around the T-junction, e.g. air and water volume fractions at different lengths of the outlet part of the mini-channel and the pressure loss throughout the mini-channel. The computational domain of the Two-fluid model is made as following. First the geometry is designed and discretized into a number of specific control volumes and sub-domains. Following the CFX Pre-solver sets the numerical boundaries, inlet and outlet conditions and properties of the geometric problem. Next the solver calculates the problem, including real time residuals of the examined parameters. The real time residuals allows the user to check if the numerical

model behaves as wanted and faster correct potential errors. Lastly the solution can be loaded into a post-program for data processing. The computational domain of the Two-fluid CFX modelling, used in the preliminary studies of this thesis, is seen in figure 3.8.

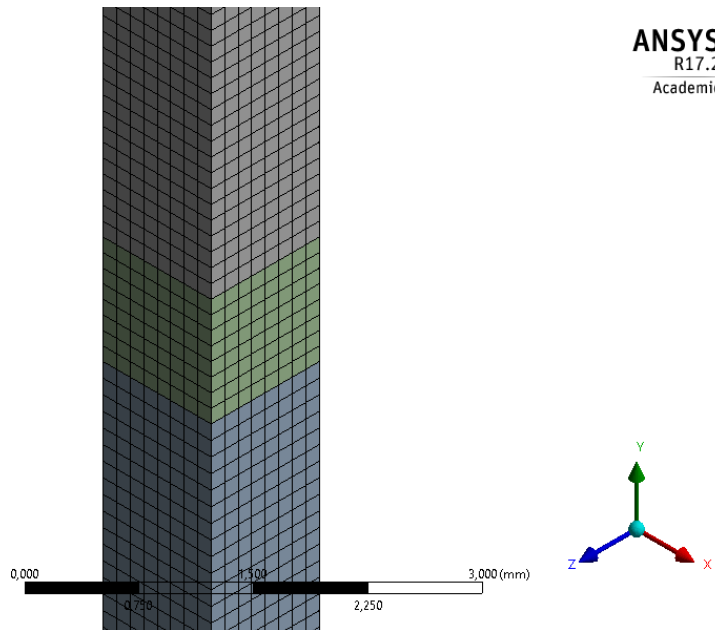


Figure 3.8: View of the build computational grid around the T-junction of the geometry of the Two-fluid modelling.

The Two-fluid geometry for simulation is made up of three sections: a water inlet section of $1 \text{ mm} \times 42 \text{ mm} \times 1 \text{ mm}$, a mixing region of $1 \text{ mm} \times 1 \text{ mm} \times 1 \text{ mm}$ and a two-phase outlet section of $1 \text{ mm} \times 40 \text{ mm} \times 1 \text{ mm}$. Following initial model studies the Two-fluid domain will be expanded to the experimental measurements. This is done to accurately numerically determine the pressure drop across the mini-channel. As the Two-fluid model does not resolve the interface between the fluids, the air inlet is cut off the initial geometry, seen in figure 1.11, and the air conditions is applied directly to the mixing section. This is done to reduce the size of the computational domain and demand. Based on the known superficial velocities, mass flows of the phases are calculated and used as inlet conditions across the whole inlet surface. Due to conservation of mass the outlet mass flow is also specified. This is done in order to calculate overall mass imbalances of the phases and further used as a criteria of convergence throughout the Two-fluid modelling. The set inlet and outlet parameters can be seen in table 3.3.

Furthermore it is seen from figure 3.8 that the Two-fluid modelling is done using a uniform mesh. This was chosen with an emphasis on constant aspect ratios, ranging between 1-1.6 for all examined domain sizes, and low skewness of the computational domain. Furthermore, an examination of how the y-plus value affects the turbulence modelling is possible, as a more refined computational grid should encapture the boundary layer around the walls more accurately through the applied wall functions.

Although the Reynolds numbers of the fluid phases are laminar, turbulence models, e.g. dispersion

Table 3.3: Inlet and outlet mass flow values of the gas-liquid multi-phase scenario.

Mass flow ($kg \cdot s^{-1}$)	Base Scenario
\dot{m}_L	$3.9928 \cdot 10^{-4}$
\dot{m}_G	$8.4287 \cdot 10^{-7}$
\dot{m}_{GL}	$4.0013 \cdot 10^{-4}$

and Sato forces, are included in the last two cases of the Two-fluid modelling. These turbulent effects are included in order to determine the influence of fluid and particle turbulence on the two-phase flow parameters between laminar and turbulence modelling.

3.1.4 Configuration of mesh and solver in OpenFOAM

The VOF-modelling is done using OpenFOAM, which is an open source CFD-program for Linux. In OpenFOAM the necessary functions and solvers are applied directly in a scenario folder and initialized via the terminal using text files. Opposed to the simplistic mesh generator in ANSYS Workbench, OpenFOAM uses 3-D coordinate points and vectors to generate a mesh through a block structure. This thesis initialize 2-D coordinate points of the geometry and then expands these with 3-D coordinate points. The coordinate points are set as nodal points for the geometry. Blocks describing the geometry are configured from specific nodal points and interconnected to complete the geometry. Following, details regarding the cell types, number of cells and grading on x,y,z directions of the blocks are specified and checked for consistency throughout the computational grid. Lastly boundary conditions- and type are set and patched together to form the computational domain. At the inlet boundaries, the superficial velocities of air and water are set as inlet conditions for the numerical calculations. Thus water is supplied to the computational domain with a superficial velocity of $0.4m/s$ and air with a superficial velocity of $0.7m/s$. A sketch of the 3-D geometry, its nodal points and a section of the final mesh of the VOF-modelling is seen in figure 3.9 and 3.10. Setup of the mesh code can be seen in appendix A.

As seen in figure 3.9 the geometry is build out of four blocks, an air- and water inlet section, a mixing region and a two-phase outlet section. However, due to the computational demand of the VOF model the inlet and outlet channels have been shortened, compared to the real T-junction. Thus, fully developed flow can not be assumed from the beginning of the VOF simulation. However, this is circumvented by letting the smallest case run initially for an extended period of time, creating a fully developed flow inside the computational domain, and copying it upon the remaining cases as initial conditions.

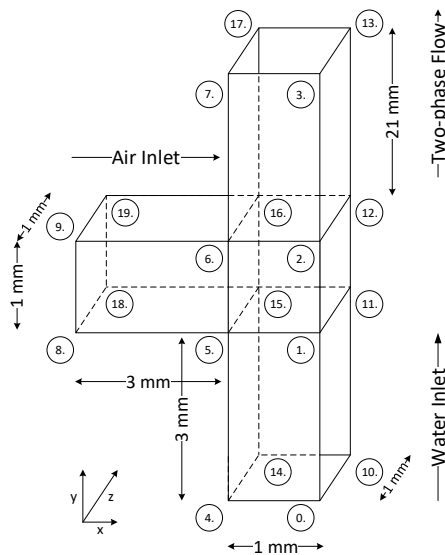


Figure 3.9: 3-D geometry with domain points. Scale of T-junction is not fitting.

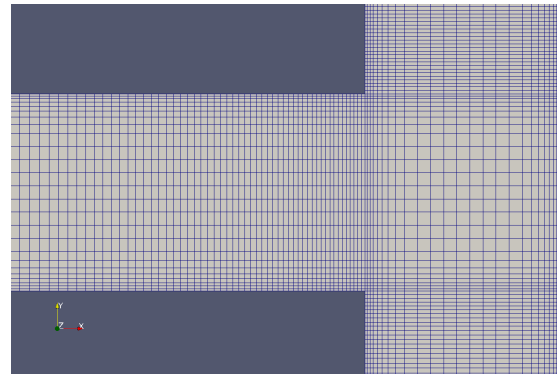


Figure 3.10: View of OpenFOAM T-junction mesh.

Block zero is the water inlet and measure $1\text{ mm} \times 3\text{ mm} \times 1\text{ mm}$. Block one is the mixing region and measure $1\text{ mm} \times 1\text{ mm} \times 1\text{ mm}$. Block two is the air inlet and measure $3\text{ mm} \times 3\text{ mm} \times 1\text{ mm}$. Lastly block three defines the two-phase outlet and measure $1\text{ mm} \times 21\text{ mm} \times 1\text{ mm}$. On figure 3.10 the final mesh profile around the T-junction of the base case is seen. As seen from figure 3.10, a grading have been applied on the x,y and z-coordinates of the mesh. The grading is applied so that cells around walls and the edges of the mixing region are refined by a factor of four compared to those around the middle and outgoing areas of the mesh. This have been made in order to obtain a higher resolution of the computational grid around the walls and edges of the T-junction without increasing the overall number cells in the computational domain excessively. This is justified as the bubble formation of the two-phase flow around the T-junction require a high computational resolution to properly be captured. Furthermore the two-phase flow in the upstream areas of the computational grid is assumed steady and reoccurring after an extended period of simulation.

However, some restrictions also apply on the VOF-modelling. Due to the VOF models complexity and boundedness to the Courant number, described in section 3.1.1, high fluid phase velocities and small cell lengths in the near wall areas impose low time steps, making the simulation computationally demanding. Thus, the VOF modelling of the examined computational domains in the grid in-dependency study will be restricted to 0.025 s. Furthermore, in order to lower the computational demand a bit, turbulence effects, e.g. fluid and particle mixing, will not be taken into consideration as a part of the VOF modelling. Thus, the two-phase flow will be modelled as a laminar flow field. The VOF-modelling will be done using the InterFOAM solver in OpenFOAM. InterFoam is a standard multi-phase solver in OpenFOAM, which operates on two incompressible, isothermal and immiscible fluids and utilize the PIMPLE scheme to numerically predict the interface between the examined fluids from the VOF approach.

The above described computational grid will be used for a grid in-dependency study of the VOF-model, but will not be expanded due to computational demand. The pressure drop across the mini-channel will be made comparable to the Two-fluid model using accumulated mean values. However the pressure drop will not be made comparable with the experimental results, as a simulation of the full geometry would require a very high computational demand, which is unobtainable in this thesis.

3.2 Grid in-dependency study of the Two-fluid model

Next a grid in-dependency study will be conducted. This is made in order to determine the needed computational domain to secure numerical independence throughout the final Two-fluid modelling of the thesis. The grid in-dependency study will be conducted on the base case and the fully extended case. Both are tested on an interval between 5000-160000 cells, where the cell count is increased simultaneously in all directions and doubled after each simulation. The tested parameters is the overall pressure loss throughout the mini-channel and the volume fractions of air at 0.0, 0.2, 0.4, 0.6, 0.8 and 1.0 characteristic length of the outlet channel. A convergence criteria was set with a residual target of $1e^{-4}$ on the examined mass and momentum variables. In addition, the residuals of the variables was tracked throughout the simulation for large fluctuations, as this could indicate a too high time step. In case the time step proved insufficient, it was lowered by a factor of ten. Furthermore, mass and momentum imbalances of the examined variables was tracked. This was done in order to determine if the residual target should be lowered in future Two-fluid modelling. A physical time step on the simulations between 5024-10125 cells was set at $1e^{-3}$ s, by default. For the simulations between 20016-80000 cells, the physical time step was set at $1e^{-4}$ s and for the 160024 cells simulation, the physical time step was set at $1e^{-5}$ s.

First the base case is examined on the given interval. The results of the simulations are seen in table 3.4 and shown in figure 3.11 and 3.12.

Table 3.4: Parametric results of base case grid in-dependency study

Cells [-]	ΔP [Pa]	α_a 0L [-]	α_a 0.2L [-]	α_a 0.4L [-]	α_a 0.6L [-]	α_a 0.8L [-]	α_a 1L [-]	y^+ [-]	m imb_a [%]
5024	515.68	0.389	0.418	0.478	0.483	0.485	0.482	26.816	-1.33
10125	484.43	0.352	0.397	0.441	0.443	0.443	0.449	20.616	-9.87
20016	547.25	0.325	0.391	0.411	0.408	0.399	0.405	18.384	-0.27
40192	532.68	0.3	0.346	0.364	0.354	0.371	0.368	14.029	-8.4
80000	557.18	0.281	0.32	0.337	0.331	0.337	0.348	12.29	-12.47
160024	558.865	0.263	0.284	0.306	0.3	0.303	0.305	10.087	-0.21

In figure 3.11 the calculated pressure loss across the two-phase outlet as a function of the cell count in the base case is seen. From the figure it is seen that between 5024-80000 the predicted pressure fluctuates. For a higher cell count, the predicted pressure is seen to stabilize with a negligible change in pressure towards 160024 cells. This indicates a stable solution around 80000 cells of the computational domain. Furthermore, the volume fractions across six planes of the two-phase outlet is seen in figure 3.12.

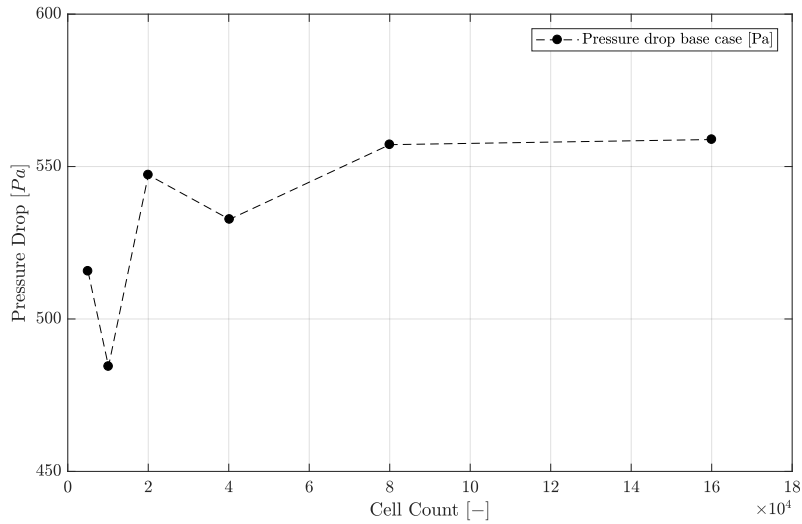


Figure 3.11: Pressure drop across mini-channel in base case.

From figure 3.12 it is seen that as the cell count within the computational domain is increased, the air volume fractions across all planes decrease. Furthermore, it is seen that the parametric decrease becomes smaller for each rise in cell count, dropping in average around 10 % per increase in cell count. However, the calculated air volume fractions have not shown to become fully independent of cell count by end of simulation, as the solution still decreases asymptotically. Though, the solution indicates the simulation is going towards a numeric stable solution. Thus, a larger number of cells

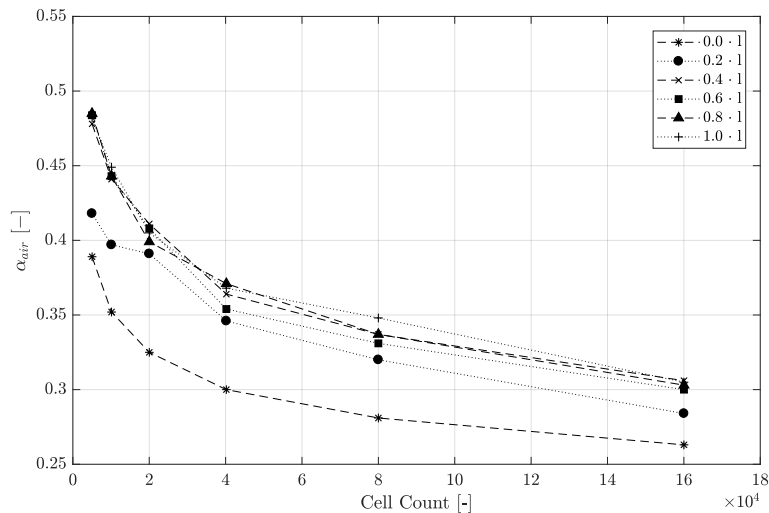


Figure 3.12: Volume fractions within the mini-channel in base case as a function of position and cell count.

would be needed to ensure numerical in-dependency of the volume fraction. A further increase of the computational grid was attempt by the authors. However, as the convergence criterion's could not be reached, even at lowered time steps around $1e^{-6}$ s, and excessive computational demands, around eight hours, arise. This was deemed unsuccessful and unfeasible within the time constraints of this thesis.

The y^+ values, seen in table 3.4, shows that the near wall modelling is in the buffer layer. However as fluid and particle turbulence is not a part of the base case, these are thought to have a low impact on the results.

Due to the overall trends seen in figure 3.11 and 3.12 and the extent of computational demand, a computational domain of 80000 cells is set for the base case as numerically stable. Though, due to the numerical predicted mass imbalance of air at the examined number of cells, the time step in the final modelling will be lowered to $1e^{-5}$ s.

Next the fully extended case is examined. The results of this examination is seen in table 3.5.

Table 3.5: Parametric results of fully extended case grid in-dependency study

Cells [-]	ΔP [Pa]	α_a 0L [-]	α_a 0.2L [-]	α_a 0.4L [-]	α_a 0.6L [-]	α_a 0.8L [-]	α_a 1L [-]	y^+ [-]	m <i>imb</i> _a [%]
5024	644.84	0.446	0.573	0.627	0.638	0.636	0.637	28.18	0.14
10125	677.29	0.424	0.561	0.623	0.636	0.636	0.637	23.78	0.24
20016	725.98	0.409	0.566	0.626	0.636	0.634	0.637	20.66	0.35
40192	805.54	0.392	0.584	0.629	0.635	0.636	0.637	16.39	0.24
80000	893.88	0.389	0.596	0.627	0.635	0.636	0.636	14.15	0.24
160024	988.304	0.404	0.601	0.628	0.635	0.637	0.637	12.66	-0.24

In figure 3.13 the calculated pressure loss across the mini-channel as a function of the cell count in the base case is seen. From the figure it is seen, that as the cell count is increased, so is the pressure drop across the mini-channel. The increase in pressure drop lies within approximately 5-10 % per increase in computational domain. Thus, the pressure drop of the fully extended case resembles the air volume fractions of the base case and can not be deemed numerically independent on a basis of the examined computational domains. Thus, further simulation was deemed unfeasible within the time restrictions of this thesis.

From figure 3.14 it is seen that as the cell count is increased, the air volume fractions across the planes look consistent. Only the air volume fractions at the 0 and 0.2 length of the two-phase outlet change at bit as the computational domain is increased. However, both are seen to settle with low changes around 80000 cells.

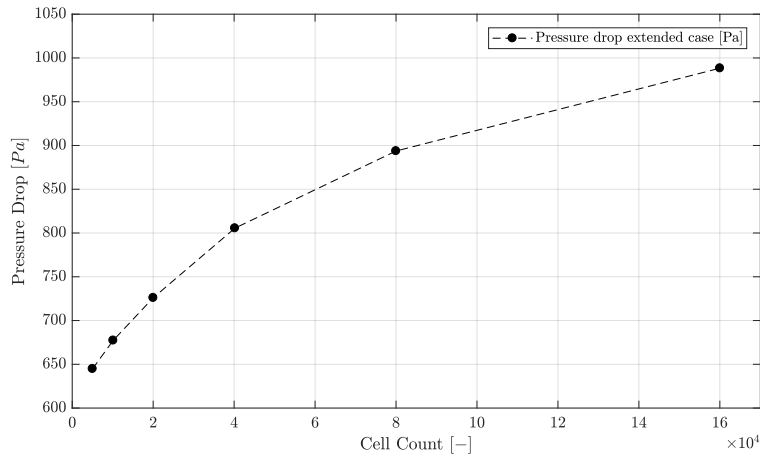


Figure 3.13: Pressure drop across mini-channel in extended case.

Like the base case, the y^+ values of the fully extended case is seen to be within the buffer layer. Thus, the viscous sub-layer has not been fully resolved through the modelling. The viscous sub-layer could possibly be resolved by adding more cells to the numerical grid, or by grading the cells around wall areas of the computational grid. As an increase in cell count was unsuccessfully attempted in the base case, grading on the cells near the walls of the computational grid was attempted by the authors. This was attempted in order to lower the overall y^+ values of the fully extended case sufficiently, to include the modelling of the viscous sub-layer. However, as the convergence criterion's could not be reached and excessive computational demands arise. This was deemed unsuccessful and unfeasible within the time constraints of this thesis.

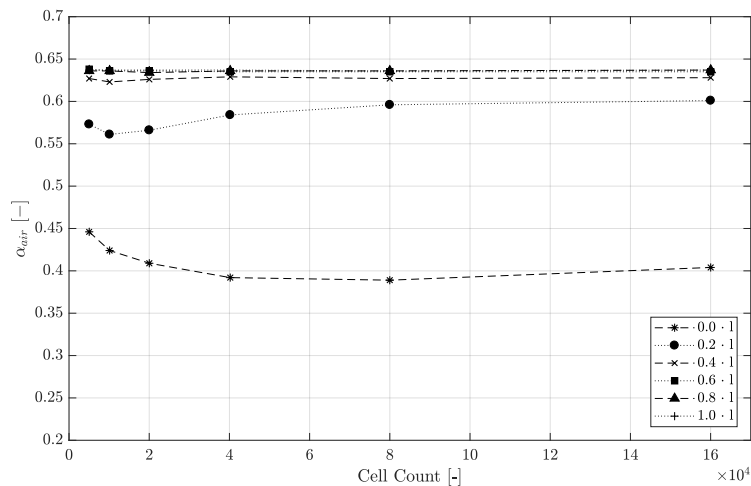


Figure 3.14: Volume fractions across the two-phase outlet of the mini-channel in extended case.

Due to the overall trends seen in figure 3.13 and 3.14 and the extent of computational demand, a computational domain of 80000 cells is set for the fully extended case as numerically stable. Despite low mass imbalances at the computational domain, the fully extended case will utilize the same time step as the base case.

3.3 Investigation of additional physics models in the Two-fluid model

As described in section 3.1.2, the additional physics in the Two-fluid modelling will be tested against a base case with buoyancy, SST turbulence model and the Schiller Neumann drag model effects included. This will be done following the overview given in table 3.2. This is done to determine the overall influence of each additional models on the base case, how they behave according to the numerical theory and if they are useful, despite a higher computational demand. Thus, a base Two-fluid simulation case with 80000 cells has been determined from the grid in-dependency study and will gradually be expanded with additional physics. Furthermore, the iteration number of convergence and mass imbalances of air is noted to examine the change in computational demand and accuracy. Lastly, the formation of the volume fraction around the T-junction is examined, in order to see if the additional models induce a significant change in the distribution of the volume fraction. Table 3.2 show the examined cases of additional physics added to the Two-phase model.

With the examined parameters set in section 3.2, the review of applying additional physics can be started. The results of the simulated cases can be seen in table 3.6. In figure 3.15 and 3.16 the pressure drop and the volume fraction across the length of the mini-channel is seen.

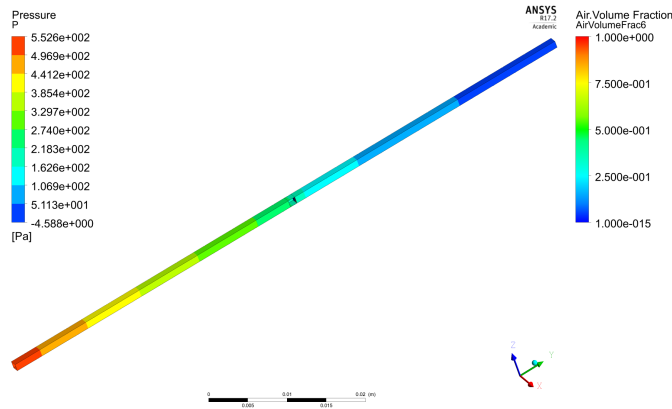


Figure 3.15: Pressure drop across the mini-channel in the base case.

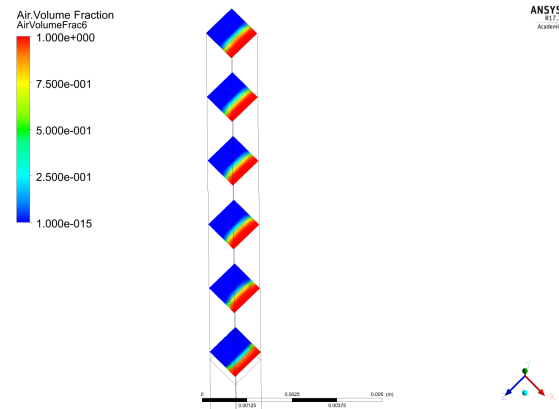


Figure 3.16: Volume fraction across sample points inside the mini-channel of the base case.

From figure 3.15 it is seen that the pressure is highest at the water inlet and drops steadily throughout the mini-channel. The total pressure drop across the channel is calculated using min/max of the whole channel. From figure 3.16 it is seen that the volume fraction of air gradually decrease from the wall and across the planes of the mini-channel. Furthermore, it is seen that the interface color of the volume fraction between the water and air changes throughout the outlet channel from green to yellow, indicating a higher volume fraction at the interface towards the outlet than at the T-junction. The volume fraction across the plane is calculated using an area

average function. The results of the volume fractions, pressure drop across the channel, iteration number and air mass imbalance in percentage is seen in table 3.6.

Table 3.6: Results of the examined case

Case	ΔP [Pa]	α_{a1}	α_{a2}	α_{a3}	α_{a4}	α_{a5}	α_{a6}	Ite. num.	$m_{a\text{imb.}}[\%]$
Base	557.18	0.281	0.323	0.337	0.331	0.338	0.348	393	-12.47
Case 1	661.21	0.324	0.357	0.398	0.388	0.394	0.387	373	-0.02
Case 2	746.98	0.329	0.373	0.47	0.591	0.562	0.602	349	0.55
Case 3	893.88	0.389	0.596	0.627	0.635	0.636	0.636	179	0.24

As seen in table 3.6, the pressure drop across the mini-channel is calculated to be 557.18 Pa. Furthermore, it is seen that the volume fraction of air increases downstream of the mini-channel, reaching a max value of 0.3448. From the second plane, the volume fractions are close to constant across the last planes of the two-phase outlet channel. Lastly, it took the simulation 393 iterations to converge, with a mass imbalance of air at -12.47 %. As written in section 3.2, the time step in the final base modelling will be lowered, in order to decrease the mass imbalance of air.

Another interesting point of examination is how the volume fraction of air is formed around the T-junction. Figure 3.17 shows how the volume fraction of air forms from the T-junction.

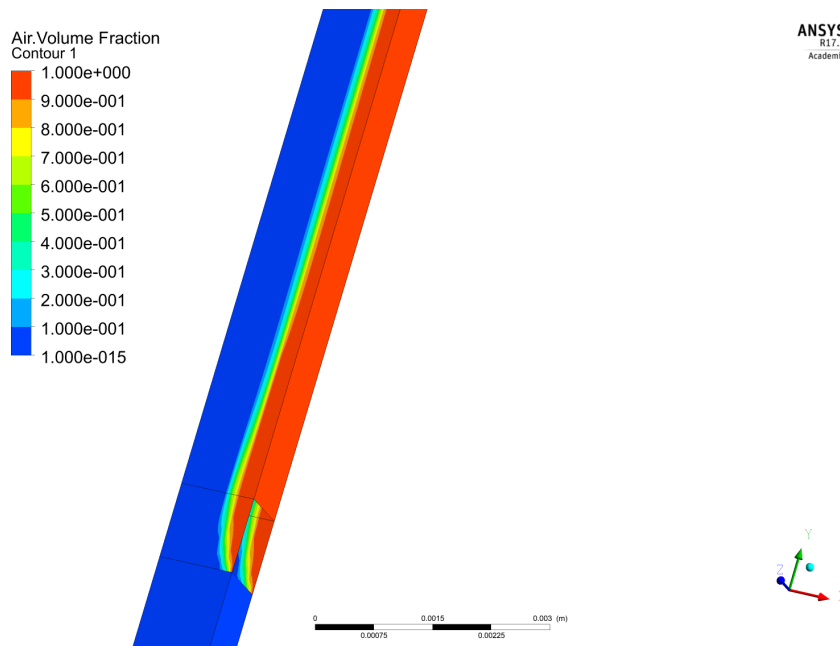


Figure 3.17: Volume fraction development around T-junction for base case.

In figure 3.17 it is seen that the air volume fraction sticks along boundary wall of the two-phase outlet section and behaves rather constant downstream the two-phase outlet section. This is probably due to the included physics, which have no fluid or particle mixing included. From the boundary wall, the air volume fraction profile is seen to decrease across the width of the two-phase

channel section to being fully water on the opposite wall. This balances nicely with the results shown in table 3.6 and the theory of the Two-fluid model, as the air volume fractions are solved from the transport equation, which do not take fluid mixing and the fluid inter-phase into account.

Next, the Tomiyama lift model and virtual mass forces are added to the model. Figures of the examined pressure and volume fractions imitate those of 3.15 and 3.16 and will therefore not be presented. A simulation with these additional models yielded the results seen as case 1 in table 3.6.

With the additional models included, the pressure drop across the mini-channel, is now 661.21 Pa, whilst the air volume fraction across the planes are calculated between 0.324 and 0.398. Thus, the additional models are seen to increase the volume fraction throughout the channel section containing the two-phase flow. As seen, the iteration number has decreased to 373 for convergence, with a mass imbalance of the air of -0.02 %. Thus, the additional models have decreased the mass imbalance, indicating a higher accuracy solution. Thus, all examined parameters have increased, compared to the base case. The additional physics should have increased the accuracy of the model, as more physical effects have been modeled.

Next the Tomiyama wall lubrication and Favre turbulent dispersion forces are included in the Two-fluid modelling. As for the previous case, the figure of the pressure drop does not change significantly and will thus not be shown. However, the distribution of the volume fraction across the planes have changed as seen in figure 3.18.

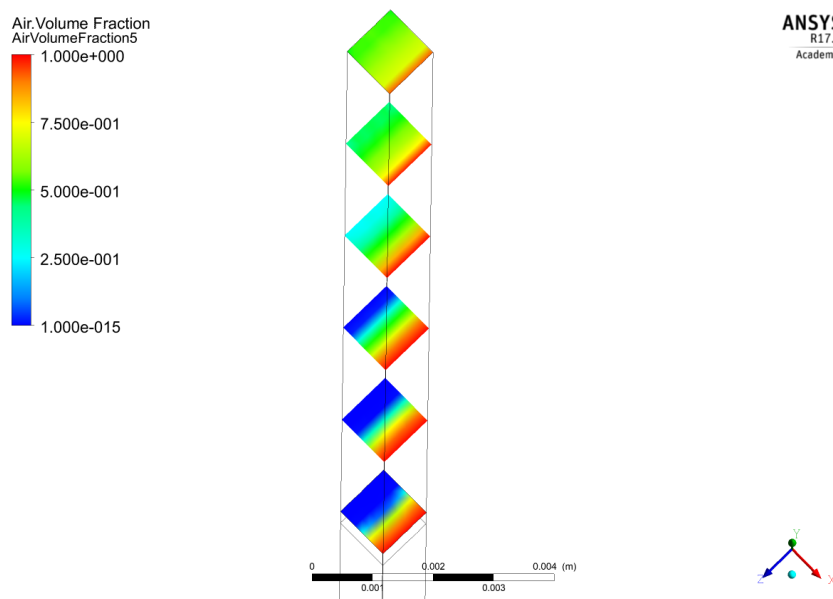


Figure 3.18: Volume fraction across the set planes for Tomiyama and Favre extended case.

From figure 3.18 it is seen that as the flow develops throughout the two-phase channel section, the volume fractions of air get more evenly distributed across the planes. Furthermore, it is seen that the layer of high air volume fraction along the wall slowly is dispersed across the planes moving

towards the outlet. This is due to the introduction of the disperse turbulence physics, which allows turbulent momentum transfer on the interface between the fluids and expected from the theory. The results of the Tomiyama and Favre extended case are seen as case 2 in table 3.6.

With the additional included models the results have increased even further. The pressure drop across the model is calculated to 746.98 Pa and the volume fraction between 0.329 and 0.602 at the inlet and outlet of the two-phase channel section. The increased results is due to the additional models which allow a much greater turbulent mixing between the fluids and thus higher average air volume fractions across the planes. This turbulent mixing also induces a higher pressure drop across the mini-channel and evens out the distribution of air across the width and height of the mini-channel towards the exit of the two-phase section. The induced mixing was expected from the additional applied models. The simulation took 349 iterations to converge and had a air mass imbalance of 0.55 %. Thus, the computational demand is much like the previous cases.

Lastly, the Sato enhanced eddy viscosity transfer was written into the Two-fluid simulation. As for previous cases, the pressure distribution of the mini-channel does not change considerably and will thus not be shown. However, the introduction of further turbulence between the fluid particles have affected the volume fractions of air throughout the mini-channel, which can be seen in figure 3.19.

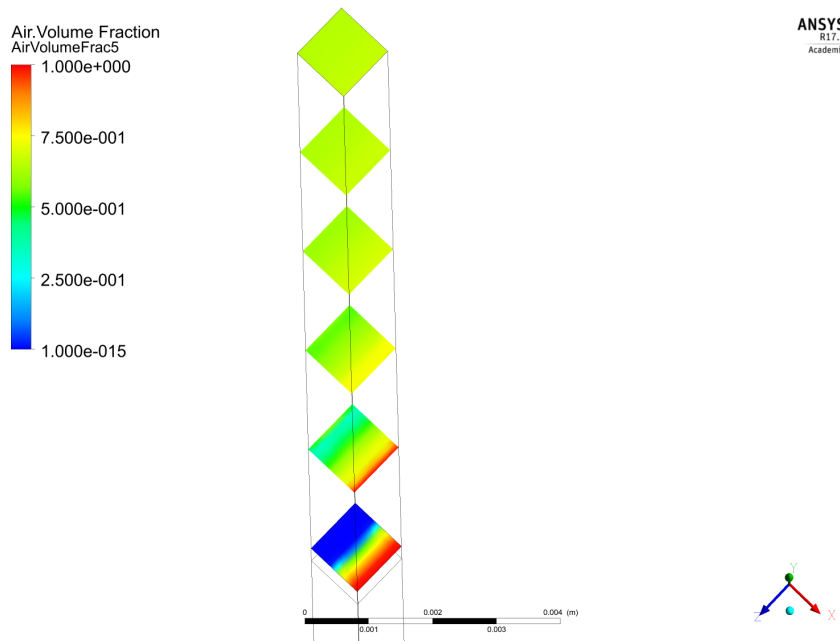


Figure 3.19: Volume fraction across the set planes for Sato extended case.

From figure 3.19, it is seen that the additional Sato model further increases the mixing between the liquid and gas phase throughout the two-phase outlet, compared to the previous cases. This was expected as the model introduces particle induced turbulence. At the exit of the two-phase channel section the air volume fraction looks constant across the whole plane, indicating a fully mixed fluid. The results of the Sato case is seen as case 3 in table 3.6.

From table ??, it is seen that the pressure drop have increased to 893.88 Pa. The air volume fractions across all planes have also increased, most notably at the second plane. Here, it should be noted that the increase in air volume fraction is seen significantly earlier than the other cases. This is due to the additional particle induced mixing from the Sato model. Furthermore, it is seen that from around $2/5$ of the characteristic length of the two-phase section of the mini-channel, the value of the air volume fraction changes marginally, indicating a close to fully mixed flow after this point of the mini-channel. The case took 179 iterations to converge, with a mass imbalance of air of 0.24 %. Lastly, in order to compare, the formation of the air volume fraction around the T-junction, of the fully extended case, is examined. This can be seen in figure 3.20.

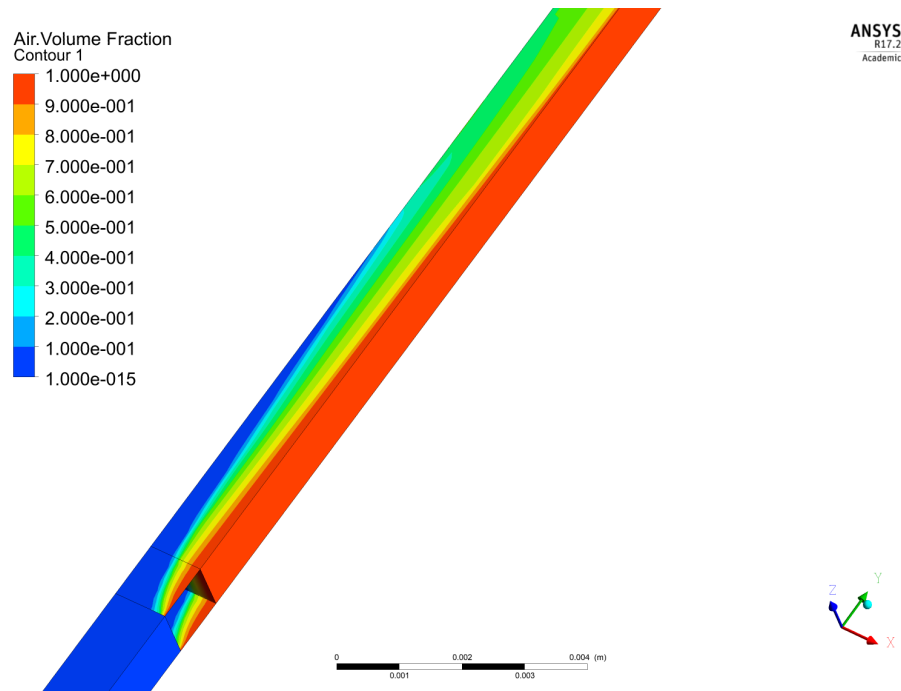


Figure 3.20: Volume fraction development around T-junction for fully extended case.

Compared to the base case, seen in 3.17, the development of the air volume fractions in the fully extended case, seen in figure 3.20, behaves different. Whereas the volume fraction of the air in the base case sticks to the wall and along its length steadily decrease across width of two-phase outlet section of the mini-channel, the volume fraction of the air in the extended case increasingly develops and smooths out across the mini-channel. This is due to the additional amount of physics in the extended modelling. Thus, the inclusion of these additional models greatly affect the two-phase flow in the outlet of the mini-channel. Thus both the base and fully extended case will be tested against the experimental results, in order to determine the accuracy of the model.

3.4 Grid in-dependency study of the VOF model

A grid in-dependency study has also been conducted on the VOF model. The model has been tested on an interval of 224000-1200500 cells, where the cell count has been increased following

each simulation with the same ratio of cells on all directions and edges. As the VOF model utilizes a transient solver, identical initial conditions was set to ensure a frame of reference. The initial conditions have been determined from running the coarsest test case for an extended period of time, in order to obtain a stable flow field inside the mini-channel. Once done, the flow field and its parameters was copied on top of the finer test cases as initial conditions. The initial volume fractions inside the mini-channel can be seen in figure 3.21.

Conversion criterion's was set specifically for the individual parameter. Thus the volume fraction has a tolerance target of $1e^{-6}$, whilst the tolerance target of the pressure was set at $1e^{-4}$ for conversion. Furthermore, in order to increase the accuracy of the solution, three correctors was added on the used scheme for the simulations. The correctors determines the number of times the numerical scheme solves the subjacent equations for each calculation. Lastly, the time step of the VOF modelling is bound to the Courant number criterions and will adjust accordingly throughout the simulations.

The examined parameters will be taken as accumulated mean values of each written interval across the simulation length. An example of this calculation for the averaged mean pressure field would be as in equation 3.37.

$$\bar{P}_n = \frac{\sum P_n}{n} \quad (3.37)$$

The written interval length are set as 0.0005 s and the initial simulation length have been set as 0.025 s, due to computational demand of the numerical model. This simulation length create 49 data collections and ensure the initial flow field has enough time to exit the channel, the finer flow field can develop and a steady-state solution of the flow can be obtained, based on the data collections. If the examined mean parameters are close to or similar at the end of the simulation of the different grid sizes, the computational domain is seen as numerically independent and will be used for further simulation to increase the accuracy of the steady-state solution.

The examined parameters will be the overall pressure loss throughout the mini-channel and the volume fractions of water at 0 mm, 6 mm, 12 mm, 18 mm and 21 mm length of the outlet channel. Furthermore, images of the bubble formation inside the mini-channel at the last examined time-step will be compared. The overall results of the examined parameters can be seen in table 3.7 and figure 3.22 and 3.23.

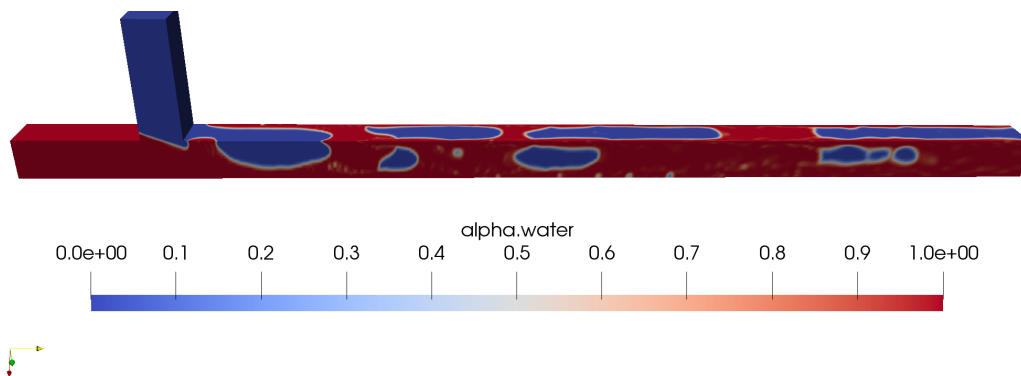
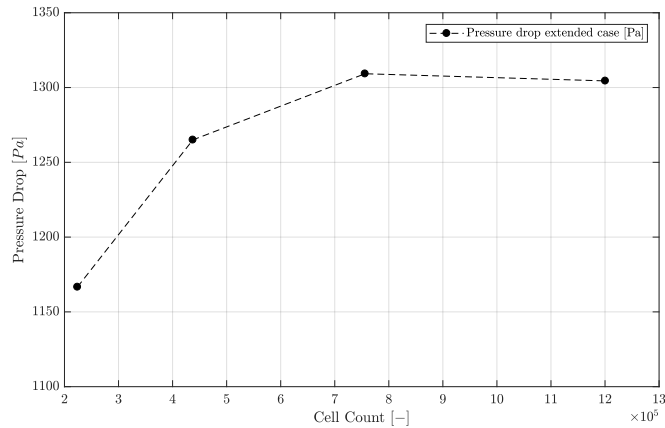


Figure 3.21: Initial volume fractions inside the mini-channel for the grid in-dependency study.

Table 3.7: Parametric results of VOF grid in-dependency study

Cell count [-]	ΔP [Pa]	$\bar{\alpha}_w - 0L$ [-]	$\bar{\alpha}_w - 0.2L$ [-]	$\bar{\alpha}_w - 0.4L$ [-]	$\bar{\alpha}_w - 0.6L$ [-]	$\bar{\alpha}_w - 0.7L$ [-]
224000	1166.628	0.795	0.475	0.533	0.525	0.387
437500	1264.994	0.787	0.478	0.501	0.521	0.383
756000	1309.217	0.794	0.504	0.515	0.514	0.399
1200500	1304.44	0.781	0.483	0.536	0.519	0.398

**Figure 3.22:** Pressure drop across the mini-channel as a function of cell count for the VOF modelling.

As seen in table 3.7 the mean volume fractions across the different planes does not change significantly as the cell count is increased. This is further confirmed by figure 3.23. However, the mean pressure drop across the mini-channel is seen to increase with the cell count until 756000 cells, where it settles. Thus, based on the parametric results and the figures, the VOF modelling indicates to be numerically independent at 756000 cells.

Furthermore, an examination of images of the bubble formation at 437500, 756000 and 1200500 cells after 0.025 s of modelling was conducted. These images are seen in figure 3.24.

Taking a further look at images of the bubble formation of air between 437500 and 756000 a clear difference is seen. From figure 3.24 it is seen that a higher resolution of the mesh more accurately capture how the bubble move around the corner of the T-junction. Furthermore the edge of the bubbles are more clearly capture at 756000 cells, than at 437500 cells. This is expected as the higher solution on the mesh should increase the accuracy of the bubble interface around the edges and the movement within the mini-channel. Thus, compared with the parametric results, the numeric case of 756000 cells is preferred. Furthermore, compared to the bubble formation at 1200500 cells, no significant change in the bubble formation is seen at a higher computational resolution. Thus, the VOF modelling is deemed numerical independent at 756000 cells, and will be used prospectively.

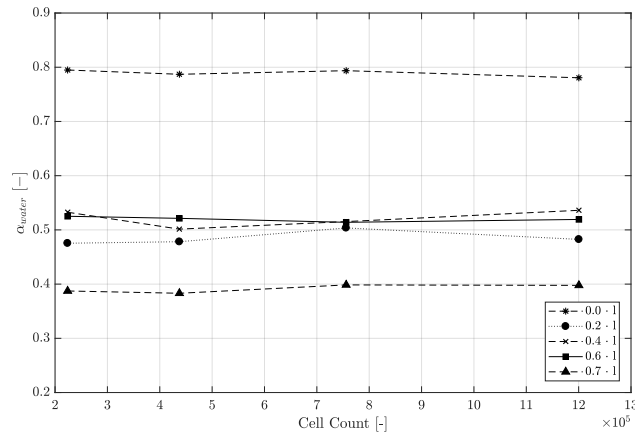


Figure 3.23: Volume fractions across the mini-channel as a function of cell count for the VOF modelling.

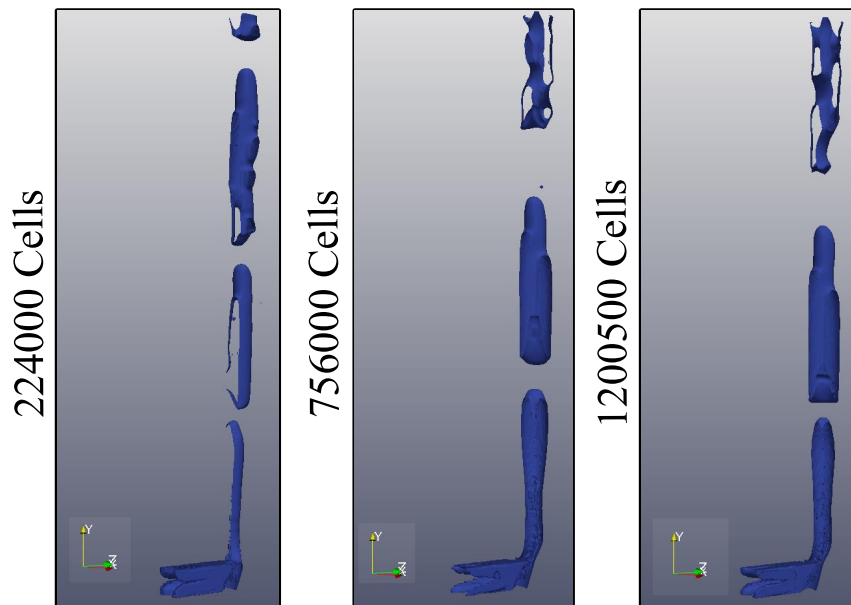


Figure 3.24: Volume fractions of air inside the mini-channel for the last written interval of the grid in-dependency study.

This chapter presents the experimental methodology and test-setup. Throughout the chapter, an in-depth description and determination of the applicable methods for obtaining clear images and information of two-phase flow in mini-channels.

4.1 Flow Measurement Techniques

There are many different flow measurement techniques with various pros and cons which are applicable to different scenarios depending on what flow information needs to be extracted. The extracted fluid flow properties should be the gas-liquid flow pattern along with, if possible, the velocities of the different phases and the void fraction. Based on these requirements different measurement techniques are considered and evaluated.

Intrusive measurement methods, like hot wire, will be difficult to implement because of the geometrical constraints, since it is a closed channel and only has a cross-sectional area of $1 \cdot 10^{-6} mm^2$. Thus intrusive methods will be discarded and will not be considered as a potential measurement technique.

4.1.1 Electrical Capacitance Tomography

Electrical Capacitance Tomography (ECT) is one of the measurements techniques which involve the measurement of electrical properties of the fluid, where some of others include measurement of the resistance, impedance, and its behavior under the influence of a magnetic field. The ECT technique is based on the difference of the dielectric constant between the two phases and the measured capacitance of the sensors depicts both the amount and the contour of the phases in the sensors vicinity - see figure 4.1 [Ismail et al., 2005].

The method is non-invasive and non-intrusive as the electrodes do not need to be in contact with the fluids, but can be placed on the outside of the pipe in which the fluids are flowing. Apart from that, it can also cope with high temperatures and pressures, is relatively inexpensive and has a fast response. However, the method does require a sophisticated and complicated image reconstruction algorithm to associate the measurements with the distribution of the two phases. Furthermore, the values of the measured capacitance for gas-liquid flow are rather small and in the range of $0.1 - 10 pF$ and to work with these small values, a decent signal to noise ratio and an appropriate shielding against stray capacitances are needed [Bertola, 2003; Ismail et al., 2005].

In [Ji et al., 2009] the authors utilize a ECT setup on a two-phase gas-liquid flow in micro-channels with a diameter of $1.8 mm$, $3.1 mm$ and $4.0 mm$, where the participating fluids are nitrogen and deionized water. Despite the small diameters of the pipes, the authors are able to contrive and

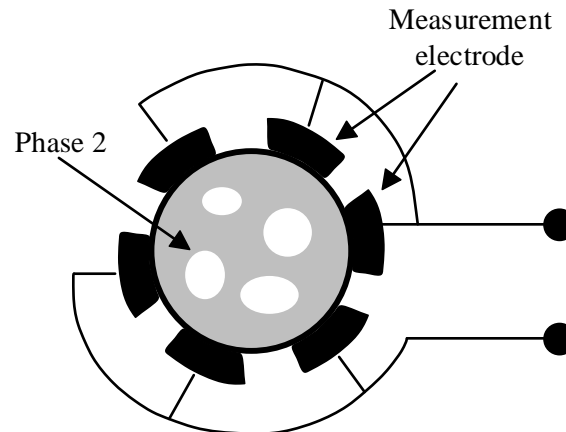


Figure 4.1: Example of a ECT setup with 6 measurement electrodes, [Ismail et al., 2005]

manufacture an usable ECT setup for the specified pipe diameters. Comparing the results with a laser based optical system, where disturbances in the laser sheet are measured by photoelectric cells, the authors conclude that a capacitance measurement method is viable for micro-channels, when the setup is designed properly.

The flow pattern is not visualized directly, but via the measurement of the capacitance and the related voltage signal of the electrode; thus a correlation between instantaneous voltage signal and the actually flow pattern would need to be made in order to identify a flow pattern's signature output signal.

Particle Image Velocimetry

Particle Image Velocimetry (PIV) is a non-intrusive optical measurement technique for fluid flow velocity. It measures the velocity indirectly via tracer particles inserted into the fluid flow which are illuminated by a laser sheet. Two pulses with a known time difference is sent from the laser and by recording the displacement of the small tracer particles, the fluid flow velocity can be estimated. The technique provides an instantaneous velocity field for a cross-section of the flow. This is a proven method for measuring the fluid velocity of a one-phase flow, but it can also be used for investigations of multiphase flows if the different phases can be clearly distinguished. To ensure visual separation of the two-phase fluid, different tracer particles with different reactions to the laser sheet can be used along with two cameras, where one camera is fitted with a filter to distinguish the different tracer particles - see figure 4.2. However, when using a laser sheet for illumination, the gas-liquid interface can create false optical effects, which will result in virtual particles that does not exist in the real flow. These virtual particles will then require sophisticated software to properly compensate for the optical effects [Bertola, 2003].

This method is able to measure fluid velocity for one-phase flows without disturbing the fluid itself, as it is a non-intrusive technique. However, the utilization of PIV for velocity estimation in two-phase flow is impeded due to the optical effects created at the gas-liquid interface. Thus, a secondary technique would be recommended for determination of the gas-liquid interface as the PIV image can contain virtual particles [Bertola, 2003].

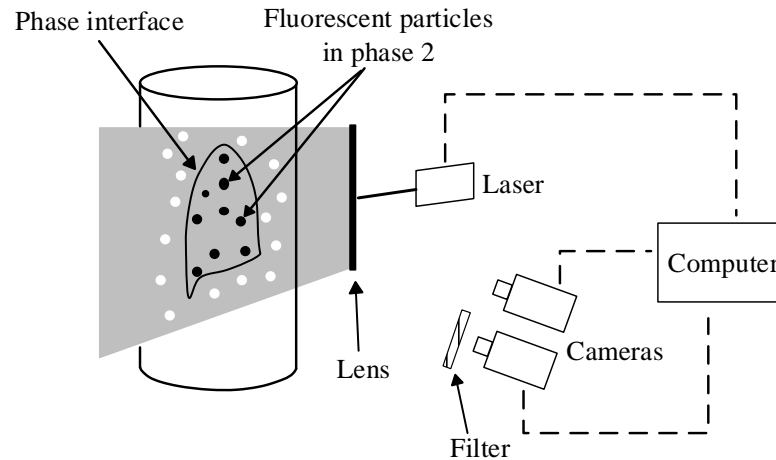


Figure 4.2: PIV setup to distinguish two-phase flow, [Bertola, 2003]

Shadowgraph technique

¹The shadowgraph technique is a simple method for optical measurements. A shadow effect is generated because light rays get refracted in an inhomogeneous medium. The differences in the refractive index between the gas and liquid phase distort the light ray and produce variations in the light intensity, which can be visualized with a image sensor placed on the other side of the medium. A homogeneous illumination source with a parallel alignment and a decent intensity is required to obtain clear images of the medium. For two-phase fluid flows the refraction will be strongest at the gas/liquid interface and the bubble periphery will be marked by a dark shadow. A disadvantage of the shadowgraph technique is that all particles between the light source and the image sensor will cast a shadow, and bubbles which are out of focus will also cast a shadow. This can create errors when measurements of bubble sizes and void fraction are made, since the bubbles out of focus could potentially cast a shadow larger than their real size. However in mini-channels the depth of the channel will limit the measuring volume and the possibility of bubble overlaps will depend on the two-phase flow regime [Mohammadi and Sharp, 2013].

This method can be used to visualize the two-phase gas-liquid flow and measure the bubble sizes along with the void fraction of the flow. The velocity can also be estimated if the bubble motion is sufficiently fixed by a fast image acquisition apparatus.

Choice of technique

In table 4.1 the different evaluation parameters and considerations, which will be used to choose a measurement technique for the experimental work, are listed. All of the techniques are able to give the flow pattern, void fraction or phase velocities in some way or the other, albeit it will require the right setup and equipment. For example the ECT will require a comparison between the measured voltage output of the electrodes and the actual fluid flow in order to identify the signature of the flow patterns.

¹FiXme Note: Måske ændre navnet til Brightfield technique (Synes Henrik nævner dette en gang imellem)

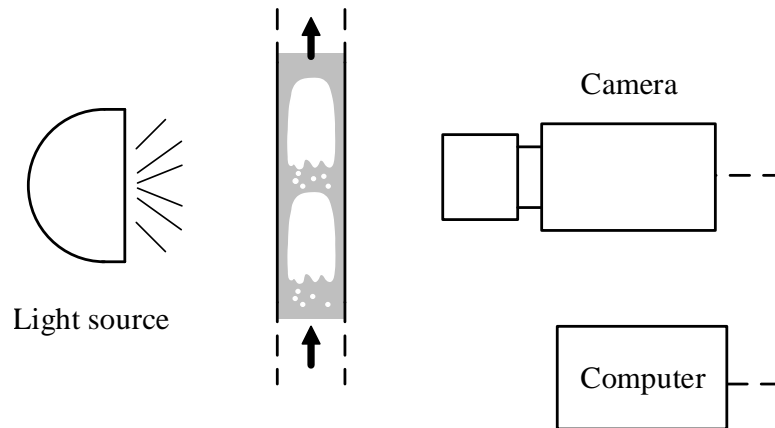


Figure 4.3: A setup where the channel is illuminated from behind.

	Flow Pattern	Void fraction	Phase Velocities	Cost of equipment	Special considerations
ECT	No (only indirectly)	Yes	Yes	High	Additional sensor shielding against stray capacitance is required to handle small (10^{-12}) measurement values.
PIV	Yes ⁽¹⁾	Yes ⁽¹⁾	Yes	High	High level of safety requirements when working with laser sheets and beams.
Shadowgraph	Yes	Yes	Yes (if fast enough image acquisition system)	Low	

Table 4.1: Comparison of potential measurement techniques for experiment.

⁽¹⁾ requires the addition of additional techniques, like Planar Laser-Induced Fluorescence for flow visualization

The ECT is the only one of the three techniques which gives measurements in the cross-sectional plane of the channel and if the sensor electrodes were extended along the channel, it would give a 3D view of the flow behavior within the channel. However, it does require a sophisticated image reconstruction algorithm to extract any viable information about the flow. On top of that, it also requires additional shielding against stray capacitances as the measurement values of two-phase gas-liquid flows are in the order of 10^{-12} . Additionally, a professional ECT system does not come cheaply and even a homemade one will be expensive and will require some knowledge regarding the setup and post-processing of measurement to acquire a acceptable image.

The PIV method might create some optical effects in the two-phase flow field, which can disturb some parts of the images and it will require additional processing to correct. However, nowadays manufactures (like Dantec Dynamics) are already offering professional solutions for PIV setups and they have a micro-PIV setup for microfluidics and flows in microchannels, which is able to handle two-phase flow with a attached droplet or bubble dispenser. As the PIV method is utilizing lasers for illumination, high level of safety arrangements is required to be in place. Apart from the

strict safety requirements, the laser and camera equipment is also quite expensive and a complete setup is even more expensive.

The shadowgraph technique is a simple, but effective method if proper equipment is utilized. Here the most expensive equipment is the camera and (if required) lens, as the lighting source can be supplied by an inexpensive LED lamp. This method does require post-processing of the images in order to get any usable information extracted from them - such as void fraction and velocities of the phases.

The authors have previously worked and obtained experience with a direct image method like shadowgraph, albeit the placement of the lighting equipment was different. In the work done by [Lafmejani et al., 2017] and the further development done by [Christensen and Rasmussen, 2017], the lighting was first placed in front of the channel and then above the channel - as the internal components limited the lighting placements.

The mini-channel has specifically been made in transparent Plexiglass, to provide an experimental setup with a clear visual accessibility of the fluid flow, in order to utilize the shadowgraph technique. The shadowgraph technique has been chosen as it gives access to the flow patterns with a relatively simple setup. Compared to the other measurements techniques, it is also considerably cheaper and the majority of the needed equipment was already available - along with a suitable software program for processing of the acquired images.

In order to properly track the bubble movement a low exposure time of the camera sensor is used, however this places a limit on the amount of light that can reach the sensor and as a result the image will be rather dark. A high intensity light source can generally improve the image quality when low exposure times are employed, since they allow more light to reach the image sensor during the exposure time [Mohammadi and Sharp, 2013]. A high-intensity widespread LED or a chain of diodes will consequently be utilized to illuminate the channel. The lighting source will be placed directly behind the cell, so it can be concentrated on the channel. This should create a high intensity lighting of the channel, which will make the separation of the gas-liquid phase clearer.

4.2 Experimental Setup

In the following section, the experimental setup and the equipment utilized for measurements in the two-phase channel flow will be introduced. An overview of the setup can be seen in figure 4.4.

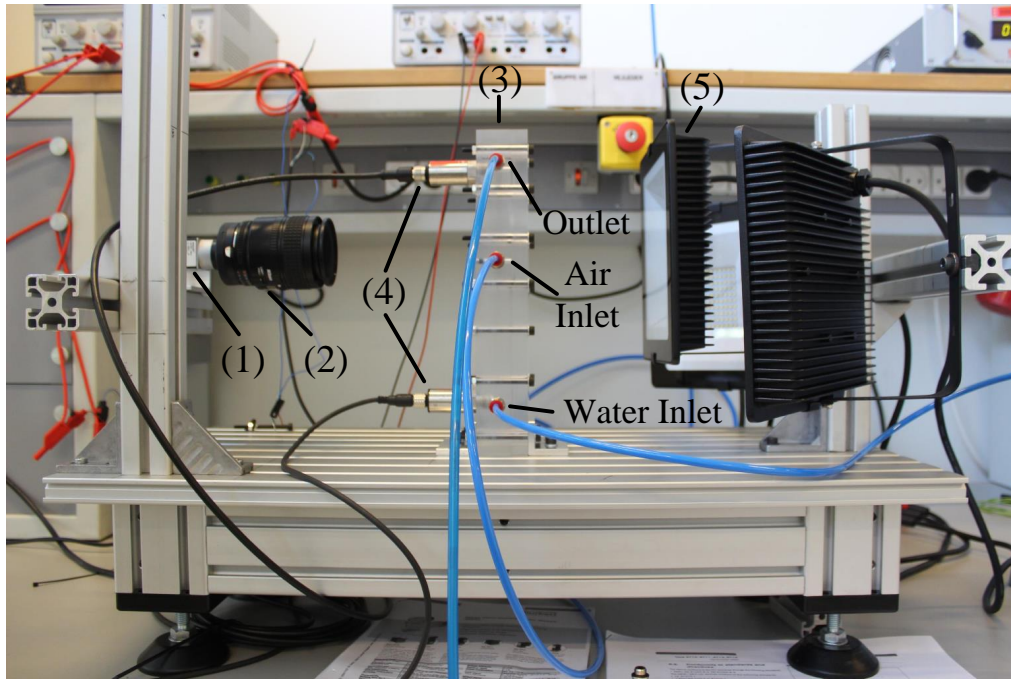


Figure 4.4: Experiment setup used for measurement

The setup consists of a camera (1) with attached lens(2), a transparent cell(3) with attached pressure transducers(4), a LED light(5), and outside the view of the figure, a water pump, a flowmeter and a flow controller for air. The camera, transparent cell and LED lamp are all mounted on a aluminum frame, which makes it possible to quickly move and fasten the components relative to each other. Furthermore, the camera and LED lamp have been mounted on transverse aluminum bars, so they easily can be adjusted more precisely in relation to the mini-channel of the transparent cell.

In figure 4.5 a conceptual drawing of the experimental setup is shown. This illustrates the position of the LED lamp and camera relative to the transparent cell, where the internal distances between the components are given in table 4.2.

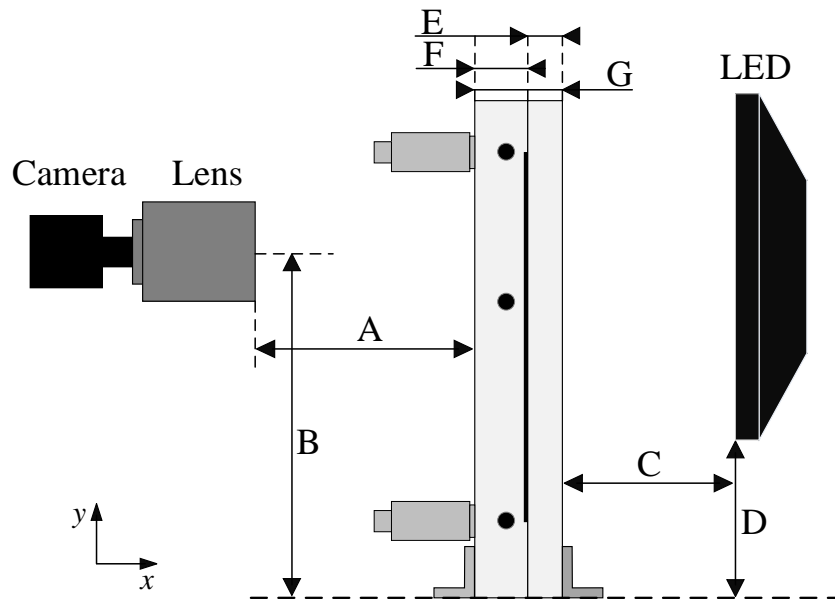


Figure 4.5: Illustration of the experimental setup mounted on the aluminum frame. The sketch is not to scale

Besides the distances given in table 4.2 of the camera and lens, they were also adjusted in the z -direction to align the mini-channel with the center of the image. The additional aluminum bar was attached specifically for this purpose, so the camera could be adjusted freely in the z -direction and was not confined to the predefined tracks in the aluminum frame.

Table 4.2: Distances for components associated with figure 4.5

	Description	Distance [mm]
A	Length from lens to front of cell	139
B	Vertical distance to middle of camera and lens	185
C	Length from back of cell to LED lamp	119
D	Vertical distance for LED lamp	85
E	Distance from mini-channel to back of cell	20
F	Distance from front of cell to mini-channel	30
G	Total thickness of transparent cell	51

The aluminum bar for the LED lamp was added to the experimental setup, as a problem was identified with the lighting during the early stages of experimentation. The lighting source of the lamp consisted of 10×7 small LEDs that had been configured in a rectangular wire-mesh configuration with some free space between each LED (Appendix A.2). This created a visible variation of light intensity on the camera, when it was viewed through an optic lens, and the LED lamp had to be adjusted to align a column of LEDs with the mini-channel.

As lighting source a LED lamp from Flash light was used with a rated power consumption at 50

W with standard 220V AC power supply. Naturally, this created a problem as the alternating current of the power supply became visibly when the camera was operated at a $\text{fps} \gtrsim 20$. To circumvent this problem the LED lamp was connected to a DC power supply. Thus, eliminating the light flicker and the voltage was carefully increase to an appropriately level of light intensity.

The supply of water was controlled with a Comet 12V pump with a maximum discharge flow of 10 L/min and a Tecfluid flowmeter with a measurable flow rate range of 0.4-4.0 L/hr ((Appendix A.4 and A.5). A Bürkert mass flow controller with a maximum flow rate of 2 L/min was utilized for the supply of air to the mini-channel (Appendix A.3). For pressure measurements two pressure transducers from Bürkert was utilized, where each measured the relative pressure in the pressure range of 0-1 bar (A.1). For operation of the mass flow controller for air and logging of the measurements from the pressure transducers, a myRIO from National Instruments (NI) with an appertaining LabVIEW program was used. The appertaining LabVIEW program can be seen in Appendix 5.3.

4.2.1 Image Acquisition and Camera Settings

To capture the fast motion and formation of bubbles and slugs in the mini-channel, an appropriate camera with a high acquisition rate was utilized. A camera from Basler fitted with a micro-lens from Nikon, made it possible to magnify a section of the mini-channel along with the two-phase flow. Some relevant specifications for the camera is listed in table 4.4

Table 4.3: Specifications for Basler acA1920-155um

Resolution (H x V)	1920 px x 1200 px
Resolution	2.3 MP
Max frame rate	164 fps (@ full resolution)
Pixel Size (H x V)	5.86 μm x 5.86 μm
Interface	USB 3.0

The large resolution area is not needed, as the mini-channel won't occupy the entire image area, but only a part of it, and can be trimmed to only accommodate the mini-channel. The changes in resolution will also affect the possible maximum frame rate, as this can increase when the resolution decreases. The decrease in resolution have effectively increased the maximum limit of the frame rate, which now have attained a value of 1100 fps . The utilized settings of the camera is listed in table 4.4

Table 4.4: Settings for Basler acA1920-155um

Resolution (H x V)	1920 px x 150 px
Resolution	0.288 MP
Max frame rate	1100 fps (@full resolution)
Exposure time	34 μs

Two different acquisition scenarios have been formed, where different information will be extracted and processed. The first scenario is a series of pictures taken at a low frame rate and over three minutes. The information, which will be extracted during this scenario, is the average length of

observed slugs and the cross-sectional volume fraction at fixed positions along the mini-channel. The fixed extraction points of experimental setup is 0 mm, 6 mm, 12 mm, 18 mm and 21 mm, in order to compare the experimental and numerical results. The second scenario will be a series of pictures taken at a high frame rate and only for a short amount of time. Here, no information will be extracted as only the visual slug formation will be compared to the simulated two-phase flow of the VOF-simulation. The specific frame rate, sample time, and number of images can be seen in table 4.5 for each scenario.

Table 4.5: Settings for the two scenarios.

	Scenario 1	Scenario 2
Frame rate	10 <i>fps</i>	400 <i>fps</i>
Exposure time	34 μs	34 μs
Sample time	180 <i>s</i>	3 <i>s</i>
Number of images	1800	1200

The cross-sectional volume fraction in scenario 1, is estimated at 5 different places along the outlet channel of the mini-channel - shown explicit in figure 4.6.

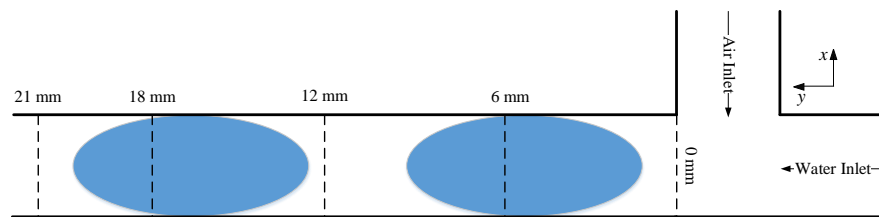


Figure 4.6: Illustration of mini-channel where the 5 places for volume fraction are highlighted. The sketch is not to scale.

4.2.2 Digital Image Processing

The image processing is only applied to the images acquired in scenario 1, as the images from scenario 2 is used for visually comparison with the VOF-simulation. However, two different approaches will be utilized to extract the different information. In figure 4.7, an untreated picture from the image sampling of scenario 1 is shown and will be used to visualize the two different extraction approaches.



Figure 4.7: A untreated picture of the mini-channel where only a coordinate has been added for reference.

As seen from figure 4.7, the edge of the slug is very clearly highlighted as dark. This was a result of a good visual combination between a low exposure time and a high intensity light from the LED. However, the air pocket in the middle of the slug is seen as white, as there is no gas-liquid interface here. Thus, no refraction of light on the air bubbles are created in these regions. This could cause problems during estimation of the air volume fraction across the mini-channel, as it would be flagged as another phase (i.e. liquid).

The software program NI Vision Assistant is used to develop a image processing script, that easily can be implemented into a LabVIEW program for image processing of multiple images. The following figures 4.7, 4.9, 4.10,4.11, and 4.12 will visually show the processing steps of script for volume fraction estimations.

In (1) the original unprocessed image is seen and in figure 4.8 the histogram of the image is shown. The histogram counts and graphs the number of pixels at each level of the greyscale. From the histogram, it is possible to determine if the image holds any distinctive regions of certain gray-level values.

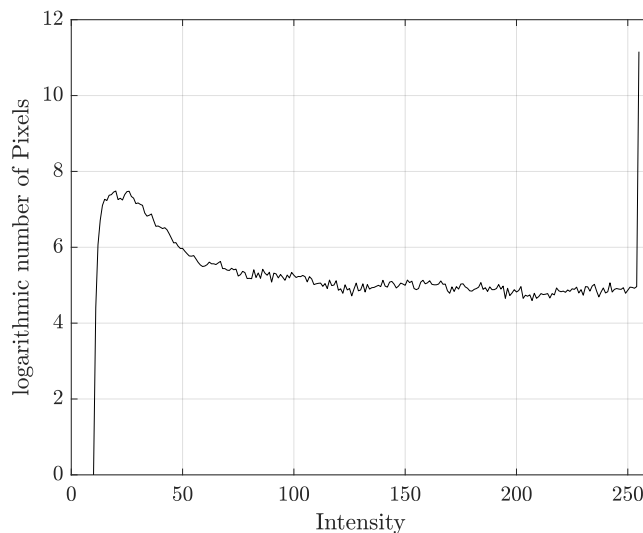


Figure 4.8: Logarithmic pixel distribution over each grayscale value.

In figure 4.9 the image is subjected to a threshold function, which involves a separation of the image into two regions - a background region and a particle region. Depending on the threshold interval, all pixels with a value inside this interval will be reassigned a value of 1 and the rest of the pixels will be given a value of 0. A threshold interval of 1-80 was used in this case to highlight the black edge of the slug. As mentioned earlier, the air-pocket in the middle of the slug would prove troublesome and it was not possible to separate this inside the threshold range. This is most noticeable in the formatting slug, were the lower part close to the wall and the T-junction falls outside the threshold range.



Figure 4.9: Picture after thresholding.

In figure 4.10 an advanced morphology operation is utilized. The operation where small particles (which might have been leftover particles from the threshold step) will be removed. The examined image does not have a lot of leftover particles. However, just above the upper slug, a very small bubble is seen. This bubble has been removed using this operation.



Figure 4.10: Picture after small particles are removed.

In figure 4.11 another advanced morphology operation is used. However, this operation enables a convex hull function. This function is used for filling out particles, even though the contour of the particle is discontinuous. It calculates a convex envelope around each particle, closing eventual holes in the particle. This function fills out the hole within the upper slug very cleanly. However, the lower slug is again proving troublesome, as the slim middle part of the slug is overestimated and made thicker, than it really is. This is due to the convex envelope, which draws around the outermost points of the slug, where the middle part falls within.



Figure 4.11: Picture after the particles have been closed.

Lastly in figure 4.12, the five extraction planes are shown and imposed on the last picture of ???. NI Vision is then able to read the pixel value (now white = 1 and black = 0) of each individual pixel along the line and give a mean value, which reflects the volume fraction along the same line. Taking an average of these 1 or 0 values across the whole data sample, can be used to calculate a mean volume fraction of air and water across the extraction planes.



Figure 4.12: Picture after the five planes have been placed across the channel.

The procedure for the estimation of slug lengths is the same up until figure 4.12. After figure 4.11 a another advanced morphology is imposed on the image, which will remove any particles in touch with the border of the picture. Figure 4.13 shows the picture after removal of border particles. However, as the previously picture did not contain any particles that where in touch with the border, the picture will remain untreated.



Figure 4.13: Picture after border particles have been removed.

In figure 4.14, a particle filter is imposed on the picture, where the compactness factor will be evaluated. The equation for the compactness factor is shown in eq. 4.1

$$\text{Compactness Factor} = \frac{A}{W \cdot H} \quad (4.1)$$



Figure 4.14: Picture after particle filtering have been removed.

Here the particle area, (A), is divided by the product of the width (W) and height (H) of a bounding rectangle - where the bounding rectangle is an automatic generated rectangle that fully encloses the particle under investigation. The compactness factor ranges from $[0, 1]$ and a lower limit of 0.6 was found to work well, where it would throw away the slugs under formation and only allow fully developed slugs to stay in the image.

From figure 4.14 the length of the bounding rectangle around a particle is utilized to estimated a length of the slug.

Experimental and Numerical Results

5

In the following chapter the experimental and numeric results will be presented and shortly interpreted. Throughout the chapter, the numerical model results will be displayed and illustrated in figures as conjunctures of the examined parameters across sections of interest within the mini-channel. In continuation, the experimental results will be displayed and likewise illustrated in graphs and figures to create a better overview of the results.

5.1 Two-fluid model results

Based on the grid in-dependency study, made in section 3.2, a numerically independent grid size of the Two-fluid modelling was determined for both the base- and fully extended case as 80000 cells. Following, the computational geometry of the Two-fluid modelling has been extended to the size of the experimental domain, with an equally large increase in cell count on the affected edges as a consequence. The geometry was expanded, in order to more accurately determine the pressure loss across the mini-channel. Thus, the computational geometry now consist of a water inlet section of $1\text{ mm} \times 125.26\text{ mm} \times 1\text{ mm}$, a mixing region of $1\text{ mm} \times 1\text{ mm} \times 1\text{ mm}$ and a two-phase outlet section of $1\text{ mm} \times 84.56\text{ mm} \times 1\text{ mm}$, with a total cell count of 197835 cells.

As stated in section 3.2, the simulations was attempted at a lower convergence criteria, where the residual targets was set at $1e^{-6}$. Furthermore, both the simulations of the base- and fully extended case was conducted with a physical time step of $1e^{-5}$ s. However, with the new set convergence criteria, the simulations could not converge and was deemed unfeasible within the time constraints of this thesis. Thus, the convergence criteria was reduced to its original value of $1e^{-4}$. Furthermore, the mass and momentum imbalances of the examined variables was tracked. In order to compare the results of the Two-fluid model with the VOF and experimental work, the volume fractions of air will be calculated as average values across planes 0 mm , 6 mm , 12 mm , 18 mm and 21 mm downstream the two-phase outlet section. The parametric results of the simulations is seen in table 5.1.

Table 5.1: Parametric results of final case simulation of the Two-fluid models.

Case [-]	ΔP [Pa]	α_a 0 mm [-]	α_a 6 mm [-]	α_a 12 mm [-]	α_a 18 mm [-]	α_a 21 mm [-]	m imb_a [%]	Ite. Nu. [-]
Base	1329.29	0.278	0.303	0.307	0.31	0.311	6.08	1847
Full	1819.57	0.397	0.582	0.622	0.631	0.634	-0.11	228

From table 5.1, a lot of the same parametric tendencies, described in section 3.3, according to

the case modelling is seen. Overall, the parametric results of the fully extended case is higher than those of the base case. The pressure drop across the mini-channel have been numerically determined to 1329.29 Pa for the base case and 1819.57 Pa for the fully extended case. Thus, the fully extended Two-fluid model numerically predicts a pressure loss which is 26.95 % higher than the base case. Contours of the pressure distribution across the examined cases are seen in figure 5.1 and 5.2.

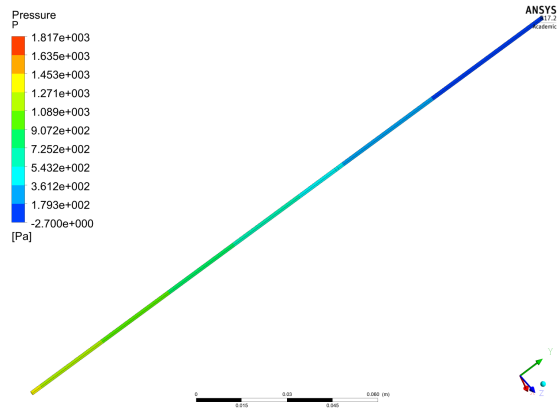


Figure 5.1: Contour of pressure drop across the mini-channel in the base case.

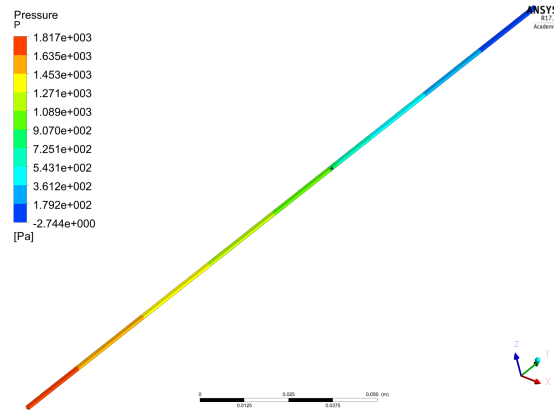


Figure 5.2: Contour of pressure drop across the mini-channel in the fully extended case.

As seen from figure 5.1 and 5.2, the overall contours of the pressure drop of the two examined cases behave similarly. However, due to lower pressures in the base case, the pressure contours stretch across larger areas in the base case. Thus, the increased pressure drop of the fully extended case must derive from the additional turbulence and model effects added.

Next, the volume fractions across the five planes is examined. As with the pressure drop, the air volume fractions across all examined planes are higher in the fully extended case. In average, the numerically predicted air volume fraction was around 50 % higher than the base case. This was determined, in section 3.2, to derive from the additional induced turbulence modelling effects in the fully extended case. Contours of the air volume fractions across the five examined planes of the two-phase outlet section of the mini-channel is seen in figure 5.3 and 5.4.

As the air volume fraction contours, seen in figure 5.3 and 5.4, behave similarly as explained in section 3.2, these will not be explained further.

The last two columns of table 5.1, show the numerical determined mass imbalance of air and iteration number for convergence of the simulations. In the base case convergence was obtained after 1847 iterations and 5.5 hours, with a mass imbalance of air of 6.08%. Compared, the fully extended case only needed 228 iterations and 45 minutes to converge, with a mass imbalance of air of -0.11 %. This indicate, that the fully extended case perform better and quicker than the base case on two-phase flow modelling in mini-channels. Though, the results have to be compared with the other models to determine the overall accuracy of the different cases.

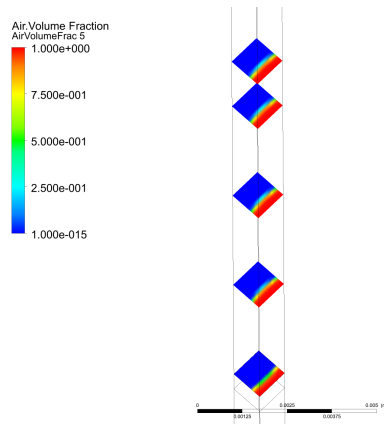


Figure 5.3: Contour of air volume fractions across the five examined planes in the base case.

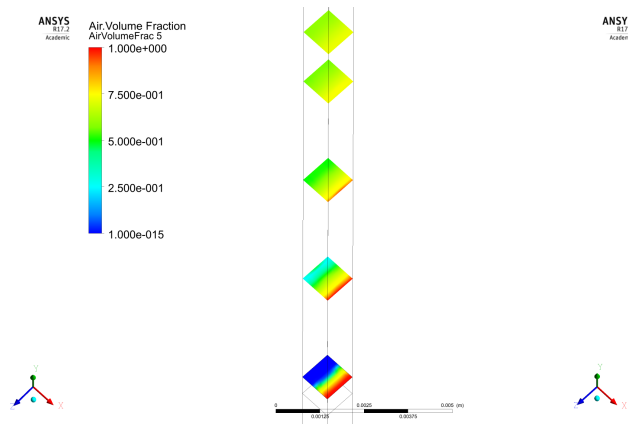


Figure 5.4: Contour of air volume fractions across the five examined planes in the fully extended case.

5.2 VOF model results

Based on the grid in-dependency study, conducted in section 3.4, a numerically independent grid size of the VOF modelling was determined as 756000 cells. Due to computational demand of the VOF model, the geometric domain of the VOF modelling was kept similar to the one used in section 3.4. Following the grid in-dependency study, the VOF modelling was continued for an extended period of time (four days), in order to obtain a better steady-state solution of the accumulated calculated mean values. By end of the final simulation, the VOF-modelling had run for 0.49 s and extracted results across 97 time steps. The numerically calculated accumulated mean parameters of the final VOF modelling, is seen in table 5.2.

Table 5.2: Final parametric results of VOF numerical study

Cell count [-]	ΔP [Pa]	$\bar{\alpha}_a - 0$ mm [-]	$\bar{\alpha}_a - 6$ mm [-]	$\bar{\alpha}_a - 12$ mm [-]	$\bar{\alpha}_a - 18$ mm [-]	$\bar{\alpha}_a - 21$ mm [-]
756000	1297.27	0.208	0.489	0.507	0.493	0.614

The numerically predicted accumulated mean pressure loss across the segment of T-junction using the VOF model is calculated to 1297.28 Pa. Thus, the accumulated mean pressure loss have not changed much from the initial VOF grid in-dependency study value of 1309.22 Pa. A figure of how the accumulated pressure develops through the numerical segment of the VOF simulation at the last time step is seen in figure 5.5.

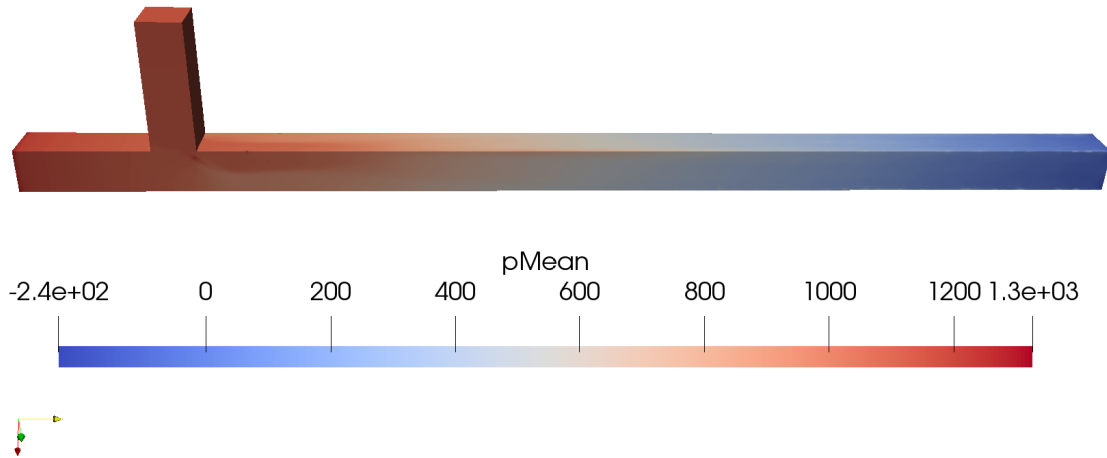


Figure 5.5: Accumulated mean pressure distribution inside segment of T-junction for final VOF simulation.

From figure 5.5, it is seen that the accumulated mean pressures are highest at around the T-junction of the segment. Furthermore, it is seen that the bubble formation around corner of the T-junction induce a small area of higher pressure, where the bubble sticks to the surface of the wall, than opposed to the opposite wall. Furthermore, across the examined time steps, the pressures was seen to change rather heavily during the detachment of the bubbles from the air inlet channel section.

Next, the air and water volume fractions across the five planes is examined. From the results, in table 5.2, it is generally seen that the accumulated mean volume fraction of air increases downstream the two-phase outlet section. The accumulated mean water volume fractions across five planes inside the mini-channel are seen in figure 5.6. The accumulated mean water volume fraction are taken at 0 mm , 6 mm , 12 mm , 18 mm and 21 mm downstream the two-phase outlet section of the T-junction segment, as integrated values across the examined plane in question.

In figure 5.6, it is seen that the accumulated mean water volume fraction on average is much higher on the front side of the T-junction segment, compared to the back side of the segment. In the front side part of the figure, it is seen how the air bends around the corner of the T-junction, sticking to the connecting wall of the air inlet section. On the back side part of the figure, it is contrary seen that almost no air sticks to the surface of the wall around the bend of the T-junction and no air reach the back wall of the mixing region. Thus, the VOF simulation show, that a layer of water is build up at back wall of T-junction, whilst the bubble formation develop inside the two-phase outlet section of the mini-channel. Towards the end of the two-phase outlet section, small occurrences of water starts to occur on the conjunctures of the back side of the T-junction segment. This indicate that the bubbles are starting to occupy a larger cross-section of the two-phase outlet section. Thus, this is further examined across six planes inside the T-junction, seen in figure 5.7.

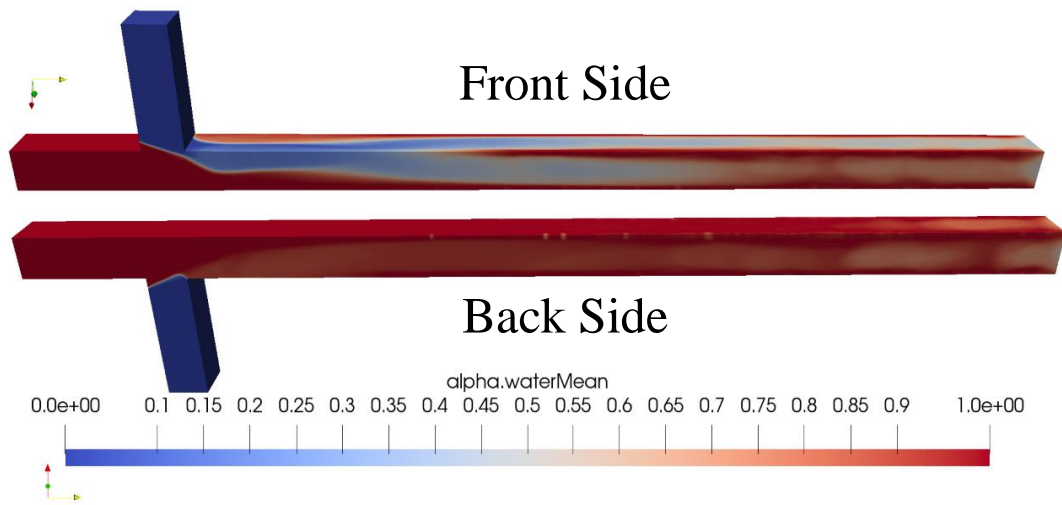


Figure 5.6: Accumulated mean water volume fractions across the front- and back side of the T-junction segment.

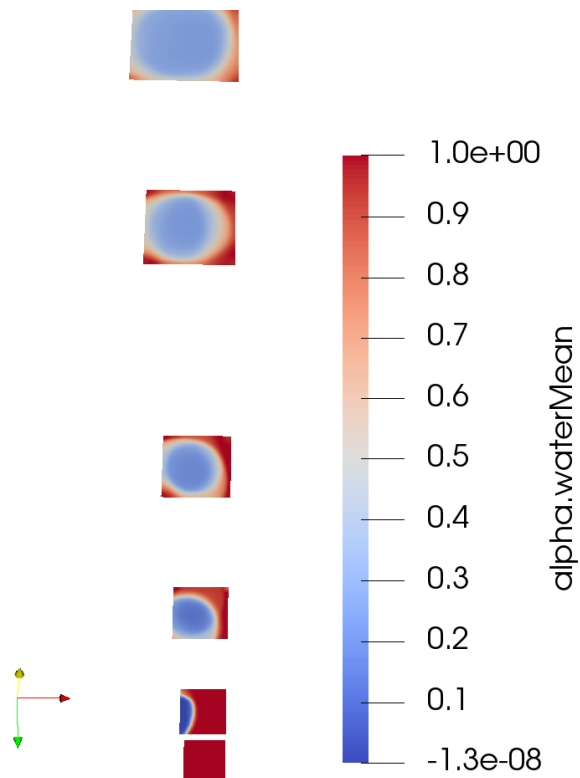


Figure 5.7: Accumulated mean water volume fractions across the examined planes of VOF T-junction segment.

Figure 5.7 show how the bubbles pass inside the two-phase outlet section of the VOF T-junction section. The first plane from the bottom is the water inlet, which is fully filled with water. In the second plane from the bottom, it is seen how the air sticks to the connecting wall of the air inlet section. In the third plane, the bubbles are formatting inside two-phase outlet. On this plane, it is seen that the bubble still sticks to the connecting inlet walls of the air inlet. However, the bubbles are also expanding across the width of the mini-channel inside the two-phase mini-channel section, occupying a larger part of the mini-channel segment. In the fourth plane, transitions in the water volume fractions along the wall starts to form. This indicates that the bubbles have detached from the air inlet section of the T-junction segment and started passing independently in the two-phase outlet section. From this plane it is further seen, that the bubbles does not come in contact with the corner edges and opposite walls inside the two-phase outlet section. This indicate, that a small film layer of water is present along the walls of the two-phase outlet segment. Across the last plane inside the two-phase outlet section, the bubbles are seen to expand in width and occupy a larger part of the outlet section. However, the corner edges of the walls are still occupied by water, indicating that the front shape of the bubble is curved.

5.3 Experimental results

The different results and measurements obtained from the experiment and the following image processing will be presented in the following text. The procedure for the image processing was introduced and covered in section 4.2.2. To get information about the slug length in real measurement units, a pixel to mm first needs to be determine. As the measurements of the mini-channel is $1\text{ mm} \times 1\text{ mm}$, this can then be used to estimate a ratio by reading the pixel length of the the channel. From the picture of the mini-channel in figure 4.7, the pixel length across the channel is read at five different places yielding -shown in table

Table 5.3: Estimation of ratio between pixels and mm

	Pixel length
Line#1	58 px
Line#2	56 px
Line#3	57 px
Line#4	60 px
Line#5	56 px
Average	57 px

A ratio of $57\text{ px}/mm$ will then be used to related the pixel measurements of the slugs to real units.

When looking at 3D-object from a 2D point-of-view, which is normal on the plane, it is difficult to estimate the depth of the object. This is also the case with the acquired images from the experimental part (see figure 4.7), where the point of view is normal on the vertical surface of the mini-channel. From this view, it is not possible to determine whether the slug fills out the whole cross-sectional area or not. However, the sphere-like shape of the slug-front indicates (along with no-slip conditions along the wall), that the slug will leave a pocket of water in the corners.

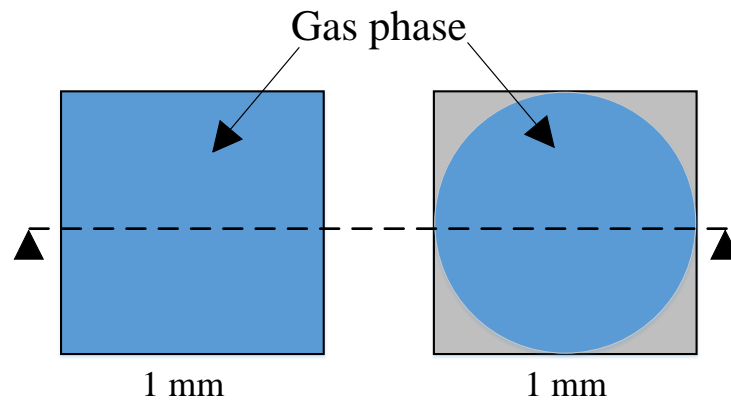


Figure 5.8: Illustration of the cross-sectional view of mini-channel with indicated plane of the experimental view.

Figure 5.8 shows the cross-sectional area of the mini-channel, where it is first filled with gas and then a circle indicating the slug seen from above. The ratio between the two areas will be used to correct the estimation of the volume fraction from the experimental images.

$$\begin{aligned} \text{Ratio} &= \frac{\text{Circle area}}{\text{Square area}} \\ &= \frac{(\pi/4) \cdot (1\text{mm})^2}{(1\text{mm})^2} = 0.785 \end{aligned}$$

All volume fraction estimations from the image processing will then be multiplied by a ratio of 0.785 to give a more accurate estimation of the volume fraction.

5.3.1 Volume fraction

The volume fraction was determined at five different places (see figure 4.6) along the outlet channel for 1800 frames which was taken over over 180 s. The volume fraction of each image is shown for plane 2 and plane 4 in figure 5.9 and figure 5.10.

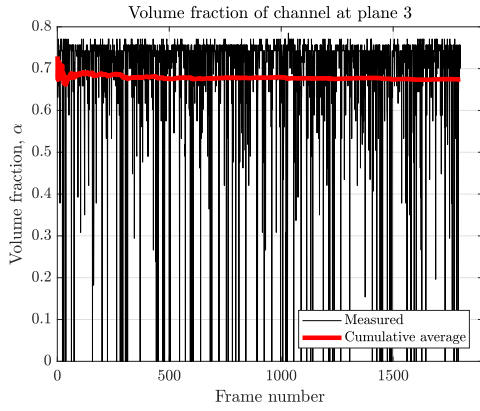


Figure 5.9: Volume fraction at plane 3 for 1800 frames

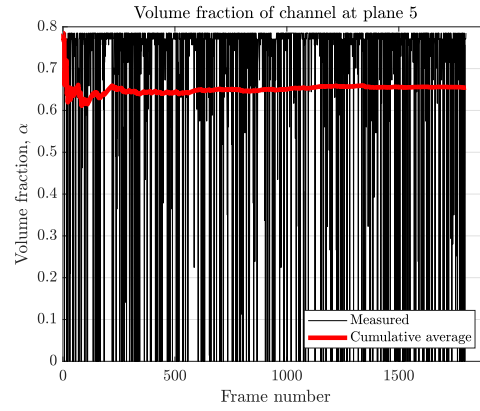


Figure 5.10: Volume fraction at plane 5 for 1800 frames

The red line is the cumulative average of the volume fraction for the plane in question and it has been calculated as:

$$\text{Average} = \frac{a_{T+1} + TA}{T + 1} \quad (5.1)$$

where A is the current average value, T the number of values, and a_{T+1} the new value. From the figures it is seen, that the cumulative average of the volume fraction have reached an approximately steady value after 300-400 images. Similar graphs have been made for plane 1,2, and 4, and though they are not shown here, the cumulative average of the volume fraction have been extracted and plotted against the cumulative average from figure 5.9 and figure 5.10. Figure 5.11 shows all the cumulative averages from all five planes.

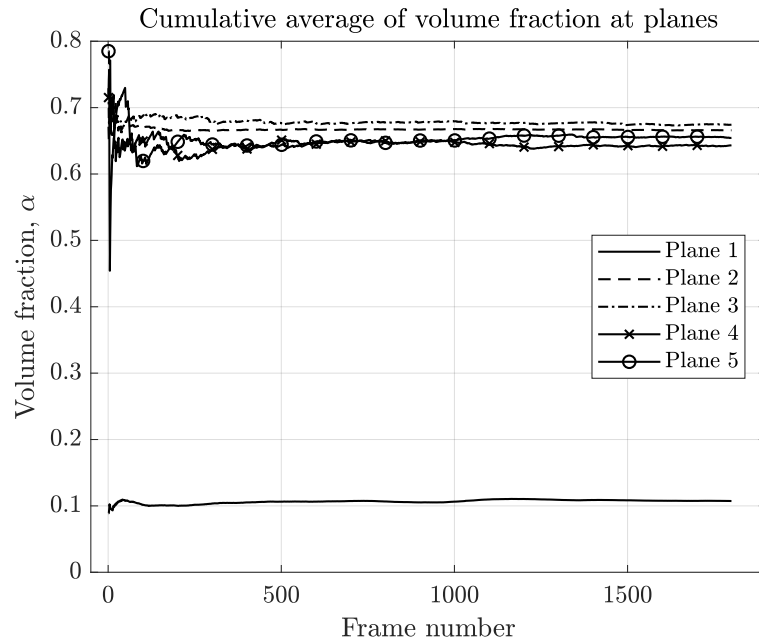


Figure 5.11: Cumulative volume fraction average of all five planes.

Again, all the lines seem to have reached an approximately steady value after 300-400 images, though plane 1 have reached it after only 100-150 images. The total average values of the volume fraction for the five planes are listed in table 5.4.

Table 5.4: Average values of the volume fraction for all five planes

	Plane 1	Plane 2	Plane 3	Plane 4	Plane 5
Final average value of α	0.1073	0.6659	0.6743	0.6433	0.6545

5.3.2 Slug Length

During the image processing of the 1800 images, the observed slugs (if any) was identified and the length of each slug was estimated. Of the 1800 images, 2303 slugs was identified following the image processing steps and filtering introduced in section 5.3.1.

In figure 5.12 the estimated length of each individual slug is shown - along with the cumulative average of the observed slug lengths, which is calculated by equation 5.1. As seen in the figure, plotting each slug length resembles a scatter plot, but with a slight majority of the lengths being plotted between in the range of $[0-5]$ mm. The minimum and maximum of the observed lengths are 0.25 and 17.8 mm, respectively.

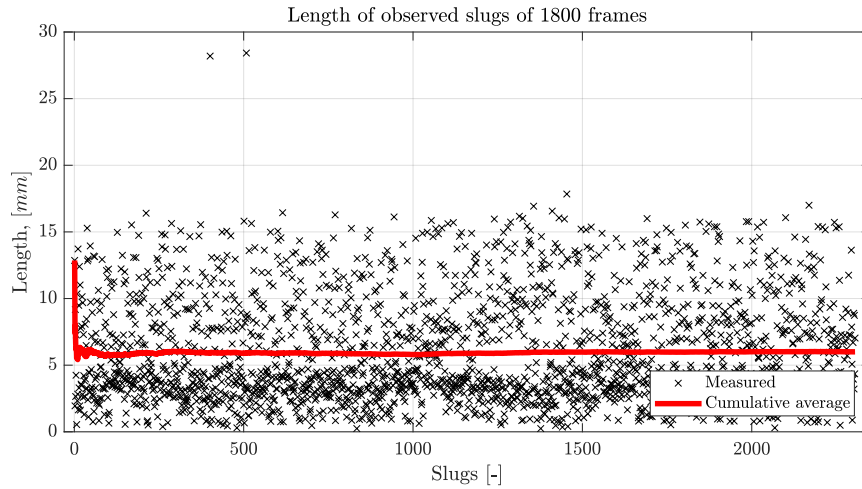


Figure 5.12: Length and cumulative average length of observed slugs.

Figure 5.13 shows the normalized frequency distribution of the observed slug lengths and, as was seen in figure 5.12, the majority of the observed lengths falls within the range of $[0-5]$ mm . The mean length of the slugs was estimated to be 5.98 mm

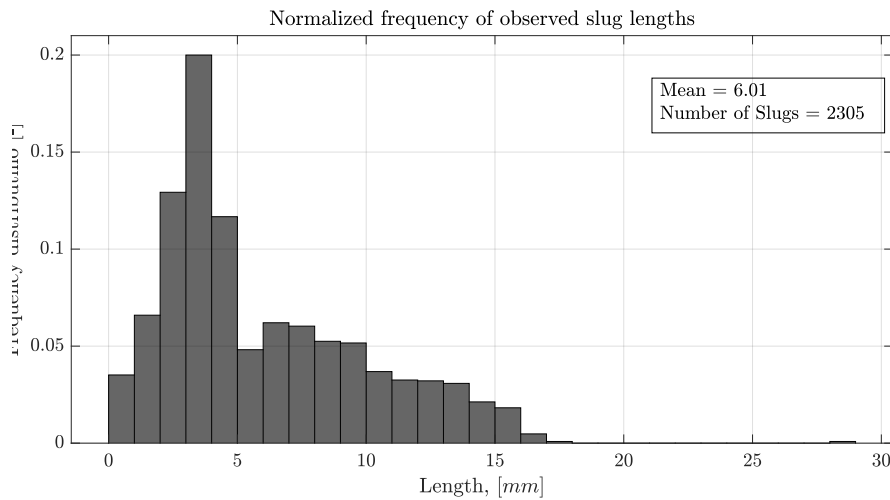


Figure 5.13: Normalized histogram of observed slug lengths.

5.3.3 Pressure Loss

During the image acquisition, the pressure was logged simultaneously at the water inlet of the mini-channel and at the two-phase outlet of the mini-channel. The placement of these is at the bottom and top of the mini-channel, respectively. However, as the image acquisition and the pressure logging was executed in different programs, the logging was initialized with a unknown

time difference between them. Nonetheless, the pressure logging was started before and stopped after the image acquisition had terminated.

Figure 5.14 shows the measured pressure at the bottom and top of the mini-channel, respectively.

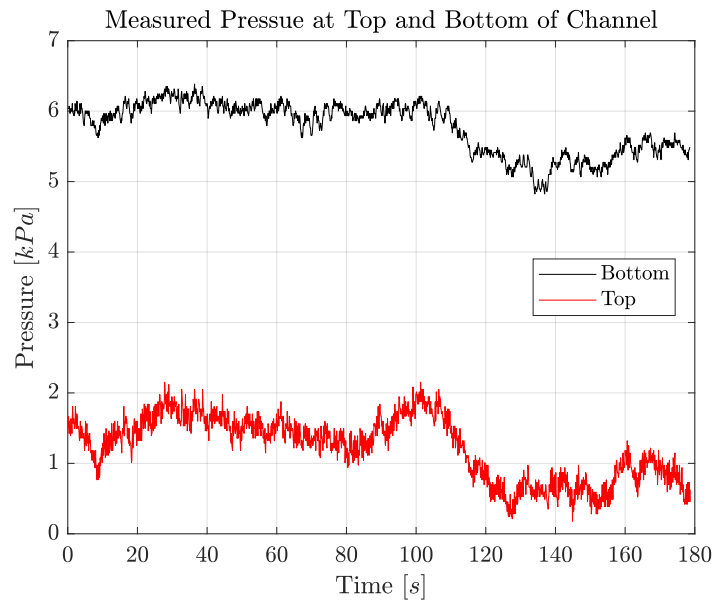


Figure 5.14: Cumulative volume fraction average of all five planes.

Figure 5.15 shows the difference in the measured pressure between top- and bottom-position. Overlaid on the graph is the cumulative average of the difference in pressure, where the cumulative average is estimated by equation 5.1.

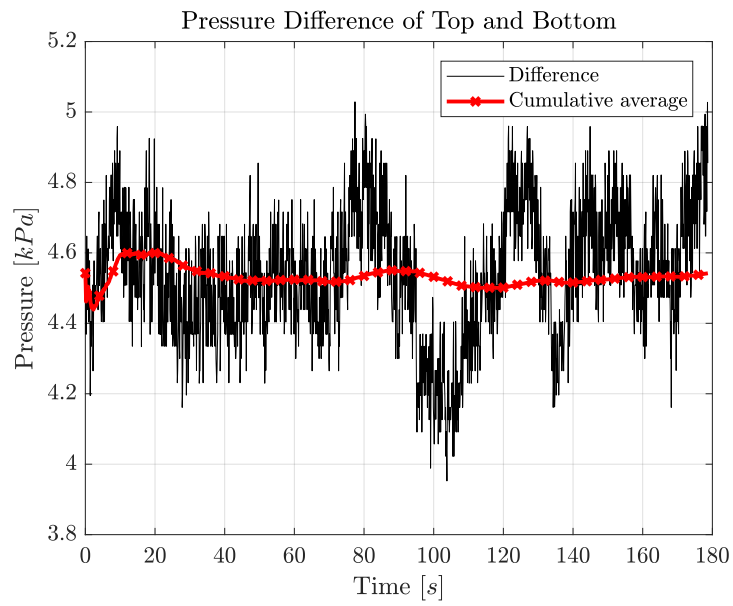


Figure 5.15: Cumulative volume fraction average of all five planes.

The total average of the measure pressure difference during a sampling period of 180 s is at 3.634 kPa.

In the following chapter, the different numerical model results and experimental results will be compared and discussed. Firstly, the pressure loss between the experimental results and the Two-fluid models will be compared and discussed. Following, the pressure loss between the Two-fluid and VOF models will be compared, discussed and put in relation to the experimental work. Next, the volume fractions across set planes of the different methodologies will be compared and discussed. Lastly, slug inspection of the experimental results and VOF modeling will be compared and discussed, in order to determine if similarities between bubble length occur.

6.1 Comparison of pressure drop between the Two-fluid and experimental approach

As it was possible to expand the computational domain of the Two-fluid model, without going on a compromise with the computational stability and demand, a comparison of the total pressure loss across the full experimental geometry, between the Two-fluid models and the experimental work, was obtainable. For this comparison, the two-fluid models were expanded to a cell count of 197835 cells and simulated following the convergence criterion's stated in section 3.2. The numerically predicted- and experimentally measured pressure losses across the mini-channel are seen in table 6.1.

Table 6.1: Total pressure loss across Two-fluid and experimental geometries

Used Approach	ΔP [Pa]
Two-fluid base	1329.64
Two-fluid fully extended	1819.57
Experimental mean	4550

As seen from table 6.2, the experimental measurements show a much higher pressure loss across the numerical geometry than both Two-fluid models. Percentage-wise the pressure loss of the Two-fluid base case is -70.77 % lower than the experimental results, whilst the pressure loss in the fully extended Two-fluid model is -60.01 % lower. Thus, indicating that the Two-fluid models have not predicted the pressure loss correctly. Some of these large errors are probably due to the authors choice of calculation models. For instance, the Schiller Neumann drag law, which is typically used to model sparsely distributed spherical particles, was used, even though slug flow was expected from the scenarios calculations in section 1.3.1. Thus, a drag law using a slug flow correlation could probably have decreased the error to some degree. This reasoning could

likewise be extended to some of the other additional numerical models used and participating to the overall error of the modelling. However, the experimental cell was also seen to leak air, from the air inlet, during experimental operation. This has probably also induced a higher pressure loss, inside the experimental cell, than expected. Thus, the actual error between the Two-fluid model and experimental could be lower than found in this thesis. Following, the authors have tried to reduce the leak of the experimental cell. However, without any improvements.

In addition to the total pressure losses across the mini-channel geometry, the pressure at 501 equally spaced points in the middle of mini-channels computational geometry, of the Two-fluid models, was extracted for further comparison of the pressure loss tendencies. This is seen in figure 6.1.

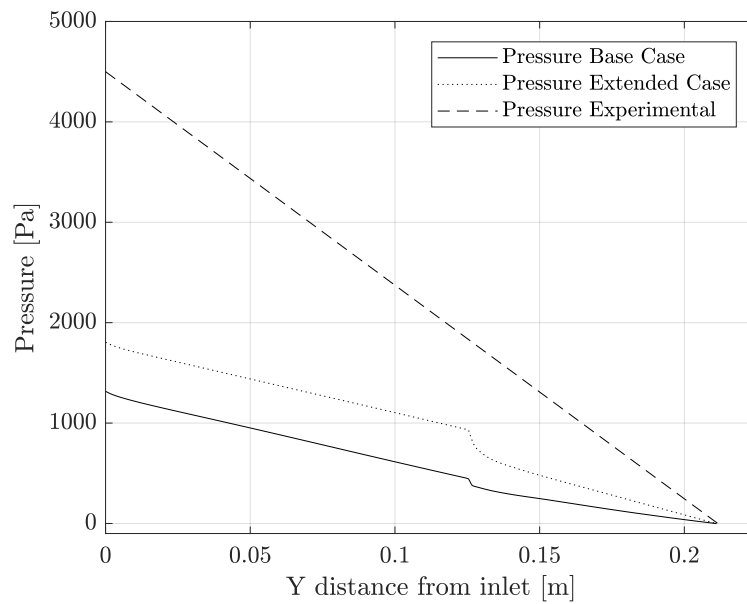


Figure 6.1: Pressure according to y-position in mini-channel geometry.

As the pressure loss inside the mini-channel of the experiment could not be determined, it is depicted as a linear decrease in figure 6.1. However, taking a closer look at the numerically predicted pressures as a function of the y-position inside the mini-channel, a sharp decrease in pressure is seen around approximately 0.125-127 m. At this y-position, the interface between the mixing region and the two-phase outlet section occurs. In this small section, the pressures drop with approximately 134.6 Pa for the fully extended Two-fluid model and 76.2 Pa for the base Two-fluid model. This strongly indicates, that transition from single phase flow to two-phase flow, induce large pressure gradients in, and right after, the mixing zone of the two fluids.

6.2 Comparison of pressure drop in the numerical approaches

One of the big points of interest regarding this thesis was the numerical difference and credibility between the Two-fluid- and VOF model on two-phase flow in mini-channels, compared to each numerical model's computational demand. As the pressure drop across the VOF T-junction segment was incomparable to final Two-fluid and experimental results, due to excessive computational demands for the full computational domain. The pressure drop of the VOF modelling will be compared and discussed against the Two-fluid model. For this purpose, the Two-fluid domain was restructured to the size of the VOF model and run until convergence. Following convergence, the total numerically predicted pressure losses of the different models across the whole geometry was noted. Table 6.2 shows the numerically predicted pressure losses of the numerical models.

Table 6.2: Total pressure loss across numeric geometries

Numerical Model	ΔP [Pa]
Two-fluid base	253.25
Two-fluid fully extended	389.65
VOF modelling	1304.44

As seen from table 6.2, the VOF numerically predict a much higher pressure loss across the numerical geometry than both Two-fluid models. Percentage-wise the pressure loss in the two-fluid base case is -80.59 % lower than the VOF modelling, whilst the pressure loss in the fully extended Two-fluid model is -70.13 % lower. Linking back to section 6.1, this could suggest that the VOF model more accurately predicts the total pressure loss compared to the experimental work. However, as the VOF model does not include turbulence effects between the fluids, the model can not be regarded as totally reliable.

In addition, to the total pressure losses across the mini-channel geometry, pressures at 101 equally spaced points in the middle of mini-channels computational geometry, of both the VOF and Two-fluid models, was noted for further comparison of the pressure loss tendencies. This is seen in figure 6.2.

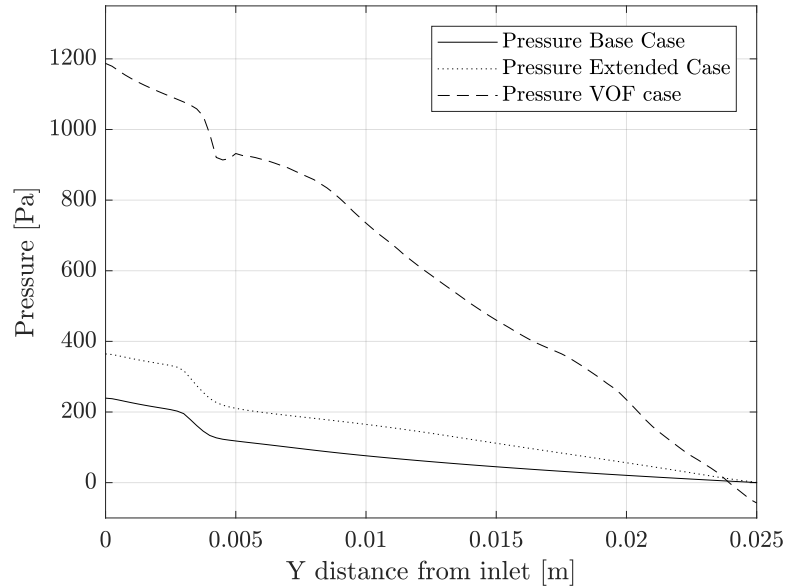


Figure 6.2: Pressure according to y-position in mini-channel geometry.

Interestingly, the tendencies of the pressure, seen in figure 6.2, as a function of the y-distance from the water inlet, behaves similarly across all three examined case. However, the decreasing trend of the VOF modelling is more explicit than the Two-fluid cases. In all examined cases, the pressures are seen to make a short steep decrease around the interface of the mixing region and two-phase outlet section between 4-4.5 *mm*. This indicates, that the bubble formation in all the examined numerical models, affects the internal pressure loss more than traditional pressure loss effects. Besides the interface region, the pressures, in all the examined cases, is seen to steadily drop. The drop is seen to follow a close to linearly regression. Thus, based on the trends seen in figure 6.2, the pressure estimations of the numerical models are seen to be calculated similarly.

6.3 Comparison of estimated slug lengths

As the VOF-method is able to simulate the formation of slugs during a two-phase gas-liquid flow, the average length of the observed slugs will be compared to the observed slugs during the experimental procedure. From a image sequence, consisting of 1800 images, the length of each observed slug was estimated and plotted in figure 5.12. The total number of observed slugs was 2305 and from figure 5.13, the mean slug length was calculated to be 6.01 *mm*.

From a VOF-simulation, with a total running-time of 0.049 *s*, 12 different slugs was identified and the length of each of them estimated. The length of each slug can be seen in figure 6.3

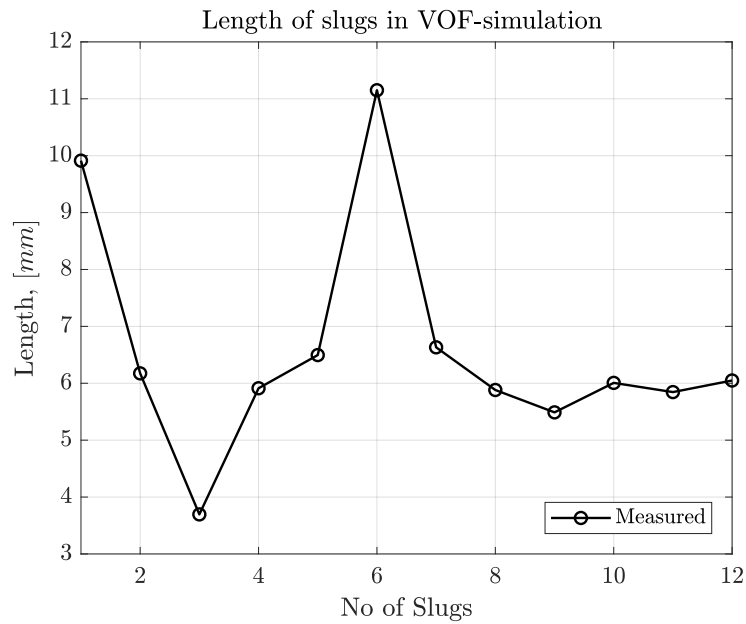


Figure 6.3: Length of observed slugs from the VOF-simulation.

The mean length of these 12 slugs was calculated to be 6.6035 mm and compared to the experimental mean length of 6.01 mm , the difference is only at 0.594 mm . Despite the short VOF-simulation time of 0.049 s , where there was only identified 12 different slugs, the difference between the two averages was relative low with per cent wise difference of 8.98% when compared to the experimental mean.

6.4 Comparison of volume fraction between numerical and experimental approaches

Five different cross-sectional planes was placed downstream of the T-junction, where the volume fraction of air for both VOF-model and Two-Fluid Flow model could be compared to the experimental obtained values. The five planes was place at 0mm , 6mm , 12mm , 18mm , and 21mm downstream of the T-junction - illustrated in figure 4.6. The experimental values was introduced and estimated in section 5.3.1 and the average volume fraction values for each plane will be replicated here in table 6.3:

Table 6.3: Average values of the volume fraction for all five planes

	Plane 1	Plane 2	Plane 3	Plane 4	Plane 5
Final average value of α	0.1073	0.6659	0.6743	0.6433	0.6545

In figure 6.4 the values from the Two-Fluid Base, Two-Fluid Extended, and VOF-model are plotted alongside the experimental values from table 6.3.

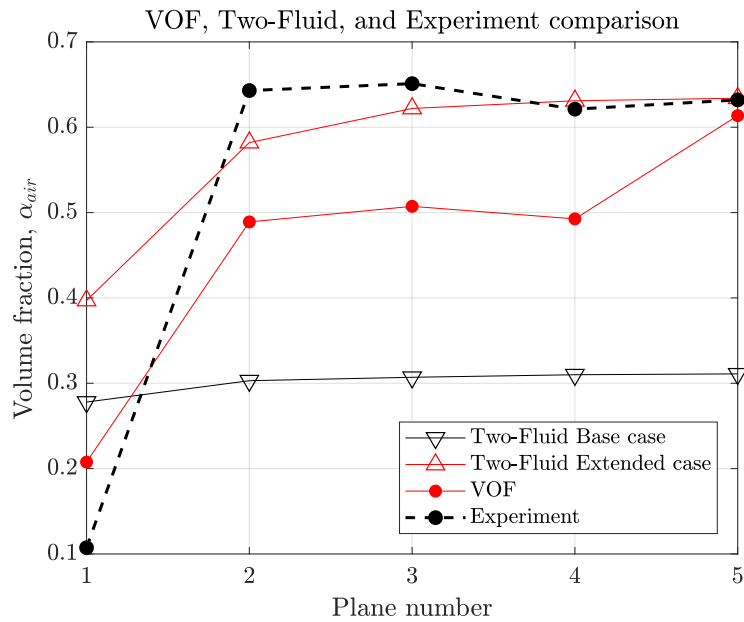


Figure 6.4: Volume fractions of the different cases at the different planes.

From figure 6.4 it can be seen, that neither one of the numerical models are able to estimated the same volume fraction as at plane 1 as what have been estimated from the experiment. For plane 2-4 the VOF-model and the Two-Fluid Extended model approximates the experimental values closer, but the Two-Fluid Base model is still quite far away.

Via equation 6.1, the percentage-wise difference have been estimated between the values from the numerical approaches and the experimental estimated values.

$$\frac{\alpha_i - \alpha_{EXP}}{\alpha_{EXP}} \cdot 100 \quad (6.1)$$

for $i = \text{VOF}$, Two-Fluid Base case, and Two-Fluid Extended case.

The differences are shown in table 6.4, where it is quite evident, that the CFD-models overestimates the volume fraction at plane 1 as much as up to 270 %

Table 6.4: Difference in volume fraction of VOF-simulation and CFX-simulations compared to experiment

α_{air}	Plane 1	Plane 2	Plane 3	Plane 4	Plane 5
VOF	93.5%	-23.9%	-22.1%	-20.7%	-2.9%
Two-Fluid Base Case	159%	-52.9%	-52.8%	-50.1%	-50.8%
Two-Fluid Extended Case	269.9%	-9.48%	-4.47%	1.58%	0.31%

If plane 1 is disregarded, it is quite clear, that it is the Two-Fluid Extended Case model that approximates closest to the values of the experiment - where the difference ranges from -9.48% to 1.58%.

Conclusions

This chapter presents this thesis key results and summarizes the projects findings in accordance with the problem statement in chapter 2 on page 27.

Two-phase flows properties in mini-channels are a topic of academic and industrial interest, especially within electrolyser technology, as these can prove valuable in the future energy grid. Hotspot formation, among others, arise from the formation of two-phase flows inside the mini-channels of the electrolysers and cause high decreases in efficiency. Thus this is sought mitigated through numerical modelling, to reduce costs. However, as the electro-chemical dynamics inside the electrolyser make it difficult to accurately simulate and predict fluid phenomenons, like flow regimes, inside the mini-channel. The authors of this thesis have decided to simplify the problem and utilize a fluid mechanical approach in order to examine two-phase flow characteristics in mini-channels, both numerically and experimentally.

As scientific work on validation between experimental and numerical VOF and Two-fluid model work on two-phase flows in squared mini-channels is lacking, this was chosen as the main focus of the thesis. A numerical and experimental two-phase test scenario was determined with air supplied at a constant superficial velocity of 0.7 m/s and water at a constant superficial velocity of 0.4 m/s. Based on the set test scenario, a experimental and numerical geometry was build and the volume fractions and pressure losses was chosen as the main parameters of validation.

The VOF and Two-fluid numerical models are both multi-phase numerical models, which is based on the Euler-Euler approach. However, the numerical models differ in modelling of the interface between the phases, as the Two-fluid model allows interpenetration between the fluid phases and solves the subjacent numerical equations as a steady-state solution. Contrary to the Two-fluid model, the VOF model does not allow interpenetration between the modeled fluid phases and solves the subjacent equations transiently. Academically, the VOF model is widely recognized as the most accurate methodology of modelling two-phase flow. However, the VOF model also have a high computational demand. Thus, due to its numerical simplicity and lower computational demand, the Two-fluid model is set against a VOF model and an experiment, in order to determine its usefulness as a numerical strategy of solving two-phase flows in mini-channels. Grid in-dependency studies showed a need of 197835 cells in the Two-fluid modelling and 756000 cells in the VOF modelling for numerical grid independence of the results. However, the VOF modelling was only conducted on a segment of the set geometry. Furthermore, a model study of the Two-fluid model resulted in two independent numerical cases, a base- and fully extended case, which was tested against the VOF and experimental work.

The experiment consisted of a Plexiglas T-junction cell, with optical access, where water was

supplied from the bottom and air was supplied from the side, in order to study the formation of two-phase flows inside the outlet section of the mini-channel. Furthermore, pressure transducers was added at the top and bottom of the cell, to measure the pressure loss across the mini-channel.

Results and comparisons of the different numerical and experimental methodologies was conducted. The comparison showed that the pressure loss of the Two-fluid base case was -70.77 % lower than the experimental results, whilst the pressure loss in the fully extended Two-fluid model was -60.01 % lower. Furthermore, compared to the VOF modelling, the base case of the two-fluid base case was -80.59 % lower than the VOF modelling, whilst the pressure loss in the fully extended Two-fluid model was -70.13 % lower. This indicated, that the VOF modelling and experimental results were in best correlation with each other. However, it was also reasoned in the discussion, that errors in the numerical settings by the authors and uncertainties in the experiment, could prove to lower the overall actual error between the different methodologies. Furthermore, the mean lengths of the experimental and VOF slugs was compared. These showed a difference of only 8.98 %. Lastly the air volume fractions between the numerical and experimental approaches was examined and compared. The comparison showed that the Two-fluid extended case closest approximated the values of the experiment, with differences ranging between -9.48% and 1.58% of the experimental results.

Bibliography

- Administration, 2017.** U.S. Energy Information Administration. *International Energy Outlook 2017*, 2017. URL <https://www.eia.gov/outlooks/ieo/>.
- Agarwal et al., 01 2010.** Gaurav Agarwal, Manoj Moharana and Sameer Khandekar. *Thermohydrodynamics of developing flow in a rectangular mini-channel array*. Conference Paper, 2010.
- , December 2006.** *ANSYS CFX-Solver Theory Guide*. ANSYS, 2006. URL https://www.researchgate.net/profile/Ghassan_Smaisim/post/How_to_solve_below_integral_numerically/attachment/59d6555f79197b80779ac936/AS%3A525446028115968%401502287503696/download/113+Ansys+CFX+Solver+Theory+Guide.pdf.
- ANSYS.** ANSYS. *ANSYS Fluent Theory Guide 15.0*.
- Berberović et al., 04 2009.** Edin Berberović, Nils Van Hinsberg, Suad Jakirlić, Ilia Roisman and Cameron Tropea. *Drop impact onto a liquid layer of finite thickness: Dynamics of the cavity evolution*. 79, 036306, 2009.
- Bertola, 2003.** V. (ed.) Bertola. *Modelling and Experimentation in Two-Phase Flow*. CISM Courses and Lectures. International Centre for Mechanical Science. Springer-Verlag, New York, 2003. ISBN 3211207570.
- Bi and Zhao, March 2001.** Q. C. Bi and T. S. Zhao. *Taylor bubbles in miniaturized circular and noncircular channels*. *Int. J. Multiphase Flow*, 27(3), 561–570, 2001. doi: 10.1016/S0301-9322(00)00027-6. URL <https://www.sciencedirect.com/science/article/pii/S0301932200000276>.
- Bracco and Holst, 2013.** Gianangelo Bracco and Bodil Holst. *Surface Science Techniques*. Springer Series in Surface Sciences. Springer Berlin Heidelberg, Berlin, Heidelberg, 2013. ISBN 9783642342431. URL <http://zorac.aub.aau.dk/login?url=http://dx.doi.org/10.1007/978-3-642-34243-1>.
- Brackbill et al., 1992.** J.U Brackbill, D.B Kothe and C Zemach. *A continuum method for modeling surface tension*. *Journal of Computational Physics*, 100(2), 335 – 354, 1992. ISSN 0021-9991. doi: [https://doi.org/10.1016/0021-9991\(92\)90240-Y](https://doi.org/10.1016/0021-9991(92)90240-Y). URL <http://www.sciencedirect.com/science/article/pii/002199919290240Y>.
- Bürkert.** Bürkert. *Operating Instructions Type 8314*. PDF Manual. URL <https://www.burkert.se/sv/type/8314>.
- Carmo et al., 2013.** Marcelo Carmo, David L. Fritz, Jürgen Mergel and Detlef Stolten. *A comprehensive review on PEM water electrolysis*. *Int. J. Hydrogen Energy*, 38(12), 4901 – 4934, 2013. ISSN 0360-3199. doi: <https://doi.org/10.1016/j.ijhydene.2013.01.151>. URL <http://www.sciencedirect.com/science/article/pii/S0360319913002607>.

- Cengel et al., 2017.** Yunus A Cengel, Cimbala John M. and Turner Robert H. *Fundamentals of Thermal Fluid Sciences*. McGraw-Hill Education / Asia, 5.ed edition, 2017. ISBN 9789814720953.
- M. K. Christensen and N. G. Rasmussen. Visualization and Characterization of Two-Phase Flow in PEM Water Electrolysis Cell: An Experimental study. Presented at Conference for Energy Students (CES) 2017, December 2017.
- Commision, 2003.** European Commision. *Hydrogen Energy and Fuel Cells: A vision of our future*, Directorate-General for Research - Energy Production and Distribution Systems, 2003. URL http://www.fch.europa.eu/sites/default/files/documents/hlg_vision_report_en.pdf.
- Crowe, September 2005.** C. T. Crowe. *Multiphase Flow Handbook*, volume 1 of *Mechanical and Aerospace Engineering Series*. CRC Press, 2005. ISBN 9780849312809. URL <https://www.amazon.com/Multiphase-Handbook-Mechanical-Aerospace-Engineering/dp/0849312809?SubscriptionId=0JYN1NVW651KCA56C102&tag=techkie-20&linkCode=xm2&camp=2025&creative=165953&creativeASIN=0849312809>.
- Damián, 2012.** Santiago Márquez Damián. *Description and utilization of interFoam multiphase solver*, 2012. URL <http://infofich.unl.edu.ar/upload/3be0e16065026527477b4b948c4caa7523c8ea52.pdf>.
- E. Wardle and G. Weller, 03 2013.** Kent E. Wardle and Henry G. Weller. *Hybrid Multiphase CFD Solver for Coupled Dispersed/Segregated Flows in Liquid-Liquid Extraction*. 2013, 2013.
- Government, 03 2012.** Danish Government. *Aftale mellem regeringen og Venstre, Dansk Folkeparti, Enhedslisten og Det Konservative Folkeparti om den danske energipolitik 2012-2020*, 2012. URL https://ens.dk/sites/ens.dk/files/EnergiKlimapolitik/aftale_22-03-2012_final_ren.doc.pdf.
- Guerrero et al., December 2017.** E. Guerrero, F. Muñoz and N. Ratkovich. *Comparison between Eulerian and VOF Models for Two-Phase Flow Assessment In Vertical Pipes*. CT&F - Ciencia, Tecnología y Futuro, 7(1), 73–84, 2017. ISSN 0122-5383. URL http://www.scielo.org.co/scielo.php?script=sci_arttext&pid=S0122-53832017000200073.
- Instruments.** National Instruments. *NI USB-6215 DAQ module*. Data sheet. URL www.ni.com.
- Ismail et al., 2005.** I. Ismail, J.C. Gamio, S.F.A. Bukhari and W.Q. Yang. *Tomography for multiphase flow measurement in the oil industry*. Flow Measurement and Instrumentation, 16(2), 145 – 155, 2005. ISSN 0955-5986. doi: <https://doi.org/10.1016/j.flowmeasinst.2005.02.017>. URL <http://www.sciencedirect.com/science/article/pii/S095559860500021X>. Tomographic Techniques for Multiphase Flow Measurements.
- J. Schmitt and Kandlikar, 01 2005.** Derek J. Schmitt and Satish Kandlikar. *Effects of Repeating Microstructures on Pressure Drop in Rectangular Minichannels*. Conference Paper, 2005. International Conference on Microchannels and Minichannels.
- Ji et al., May 2009.** H. Ji, Z. Huang, B. Wang and H. Li. *Measurement system for characterization of gas-liquid two-phase flow in micro-channel*. pages 492–497, 2009. ISSN 1091-5281. doi: 10.1109/IMTC.2009.5168499.

- Kandlikar, June 2002.** S. G. Kandlikar. *Fundamental issues related to flow boiling in minichannels and microchannels*. Exp. Therm Fluid Sci., 26(2-4), 389–407, 2002. doi: 10.1016/s0894-1777(02)00150-4. URL <https://www.sciencedirect.com/science/article/pii/S0894177702001504>.
- Lafmejani et al., June 2017.** S. S. Lafmejani, A. C. Olesen and S. K. Kær. *VOF modelling of gas-liquid flow in PEM water electrolysis cell micro-channels*. Int. J. Hydrogen Energy, 42(26), 16333–16344, 2017. doi: 10.1016/j.ijhydene.2017.05.079. URL <http://www.sciencedirect.com/science/article/pii/S0360319917319493>.
- Landet and Ridder, 2014.** Tormod Landet and Johanna Ridder. *Free surface handling in FVM-MEK4470/MEK9470*. 2014.
- Markus Lehner, Robert Tichler, Horst Steinmüller and Markus Koppe. Water Electrolysis, pages 19–39. Springer International Publishing, Cham, 2014. ISBN 978-3-319-03995-4. doi: 10.1007/978-3-319-03995-4_3. URL https://doi.org/10.1007/978-3-319-03995-4_3.
- Mohammadi and Sharp, 02 2013.** Mahshid Mohammadi and Kendra Sharp. *Experimental Techniques for Bubble Dynamics Analysis in Microchannels: A Review*. J. Fluids Eng., 135, 212021–2120210, 2013. doi: 10.1115/1.4023450.
- og Energiministeriet, 02 2011.** Klima og Energiministeriet. *Energistrategi 2050 - fra kul, olie og gas til grøn energi*, 2011. URL http://www.stm.dk/multimedia/Energistrategi_2050.pdf.
- Olesen and Kær, October 2014.** A.C. Olesen and S.K. Kær. *Flow Maldistribution in the Anode of a Polymer Electrolyte Membrane Water Electrolysis Cell Employing Interdigitated Channels*. SIMS 55, (108), 241–249, 2014. ISSN 1650-3686. URL <http://www.ep.liu.se/ecp/article.asp?issue=108&article=023>.
- Olesen et al., January 2016.** A.C. Olesen, C. Rømer and S.K. Kær. *A numerical study of the gas-liquid, two-phase flow maldistribution in the anode of a high pressure PEM water electrolysis cell*. Int. J. Hydrogen Energy, 41(1), 52–68, 2016. doi: 10.1016/j.ijhydene.2015.09.140. URL <http://www.sciencedirect.com/science/article/pii/S0360319915300859?via%3Dihub>.
- Rajesh and Buwa, 2018.** V.M. Rajesh and Vivek V. Buwa. *Volume-of-fluid simulations of gas-liquid-liquid flows in minichannels*. Chemical Engineering Journal, 2018. ISSN 1385-8947. doi: <https://doi.org/10.1016/j.cej.2018.01.050>. URL <http://www.sciencedirect.com/science/article/pii/S1385894718300652>.
- Henrik Rusche. Computational Fluid Dynamics of Dispersed Two-Phase Flows at High Phase Fractions. PhD thesis, Imperial College of Science, Technology & Medicine, December 2012.
- Saisorn and Wongwises, April 2008.** S. Saisorn and S. Wongwises. *A review of two-phase gas-liquid adiabatic flow characteristics in micro-channels*. Renewable Sustainable Energy Rev., 12(3), 824–838, 2008. doi: <https://doi.org/10.1016/j.rser.2006.10.012>. URL <https://www.sciencedirect.com/science/article/pii/S1364032106001511>.
- Shao et al., June 2009.** N. Shao, Gavriilidis A. and P. Angeli. *Flow regimes for adiabatic gas-liquid flow in microchannels*. Chem. Eng. Sci., 64(11), 2749–2761, 2009. doi: <https://doi.org/10.1016/j.ces.2009.01.067>. URL <https://www.sciencedirect.com/science/article/pii/S0009250909000827>.

- Steinke and Kandlikar, 2006.** Mark E. Steinke and Satish G. Kandlikar. *Single-phase liquid friction factors in microchannels*. International Journal of Thermal Sciences, 45(11), 1073 – 1083, 2006. ISSN 1290-0729. doi: <https://doi.org/10.1016/j.ijthermalsci.2006.01.016>. URL <http://www.sciencedirect.com/science/article/pii/S1290072906000330>.
- Elin Stenmark. On Multiphase Flow Models in ANSYS CFD Software. Master's thesis, Chalmers University of Technology, 2013. URL <http://publications.lib.chalmers.se/records/fulltext/182902/182902.pdf>.
- Versteeg and Malalasekera, 2007.** H.K. Versteeg and W. Malalasekera. *An Introduction to Computational Fluid Dynamics: The Finite Volume Method (2nd Edition)*. Pearson, 2 edition, 2007. ISBN 978-0-13-127498-3. URL <https://www.amazon.com/Introduction-Computational-Fluid-Dynamics-Finite/dp/0131274988?SubscriptionId=0JYN1NVW651KCA56C102&tag=techkie-20&linkCode=xm2&camp=2025&creative=165953&creativeASIN=0131274988>.
- Von karman, March 1931.** T. Von karman. *Mechanical similtude and turbulence*. Nachrichten von der Gesellschaft der Wissenschaften zu Gottingen - Fachgruppe I (Mathematik), (5), 58–76, 1931. URL <https://ntrs.nasa.gov/search.jsp?R=19930094805>.
- Weller, 2008.** Henry G Weller. *A new approach to VOF-based interface capturing methods for incompressible and compressible flow*. OpenCFD Ltd., Report TR/HGW/04, 2008.
- Yeoh, 2010.** Guan Heng Yeoh. *Computational Techniques for Multiphase Flows : basics and applications*. Elsevier, Amsterdam, 2010. ISBN 0080467334.
- Yin, 2016.** C. Yin. *Computational Fluid Dynamics - Lectures 5 and 7*, 2016.

Appendix A: Experimental equipment methodologies and limitations



A.1 Pressure transmitter

In order to measure the pressure at both ends of the mini-channel, two Bürkert type 8314 pressure transducers have been utilized in connection with a NI USB-6215 myRIO DAQ (Data acquisition) module for data collection. The pressure transducers are installed in a two-wire current loop, that is used in a series circuit to provide a robust signal for measurement. The current can be converted to a voltage output drop for measurement, by adding a resistor in series circuit. The output pressure is measured relative to the surrounding pressure. The technical information of the equipment is seen in table A.1.

Table A.1: Technical data of the used pressure transducers and DAQ module [Bürkert], [Instruments].

Bürkert type 8314		
Power supply	8-33	V DC
Output signal	4-20	mA
Pressure range	0-1	bar relative
Response time	<2	ms

NI USB-6215 myRIO		
Measurement type	Voltage	V
Resolution	16	bits
Maximum voltage range	-10, 10	V

With a power supply of 24V the maximum value of the resistor can be estimated by equation A.1:

$$\text{Resistor Load} < \frac{(U - 8V)}{0.02A} \rightarrow \frac{(24V - 8V)}{0.02A} = 800\Omega \quad (\text{A.1})$$

The pressure transmitter operates in a circuit as shown in figure A.1 and it acts as a current source, where it regulates the current flow in the circuit as a function of the particular pressure range of the transmitter. The NI myRIO-1900 measures the voltage drop across a 220 Ω resistor and following Ohm's law ($U = IR$), the regulated current from the pressure transmitter can be estimated and correlated to a pressure value.

With a $220\ \Omega$ resistor in the circuit the voltage drop across it will vary from 0.88V to 4.4V , which falls within the measurable voltage range of the NI myRIO-1900.

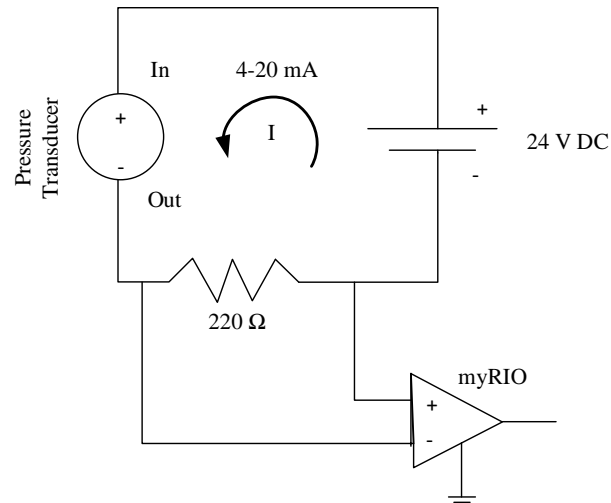


Figure A.1: Pressure transducer circuit.

In figure A.2 the linear relation between the current, voltage, and pressure of the pressure transmitter is plotted.

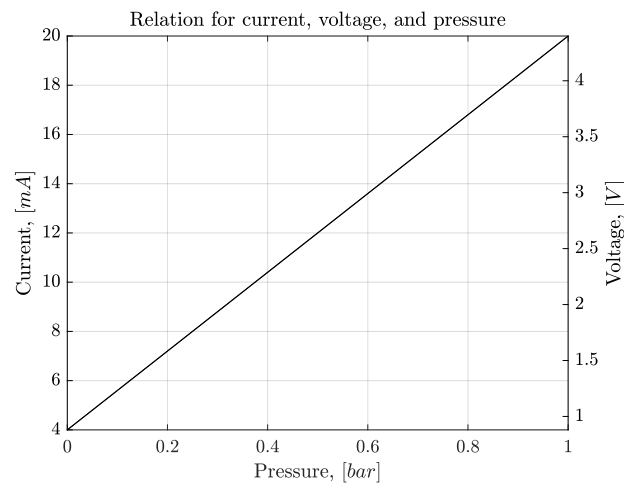


Figure A.2: Linear relation of the pressure transmitter

From the graph, the following linear relation between the pressure and the current can be read:

$$I = 16 \cdot P + 4 \quad (\text{A.2})$$

$$P = \frac{1}{16} \cdot I - \frac{4}{16} = \frac{1}{16} \cdot \left(\frac{U}{R_{load}} \cdot 1000 \right) - \frac{1}{4} \quad (\text{A.3})$$

Where P is the pressure [bar], I is the current [mA], U is the voltage [V] measured by the NI myRIO-1900, and R_{load} is the value of the resistor [Ω].

A.2 LED Lamp

A TAGGY 50W LED Lamp from FLASH LIGHT

Table A.2: Specifications

Voltage	230 V
Light Source	LED
Rated Power	50 W
Lumen	5000



Figure A.3: TAGGY 50W LED Lamp

A.3 Mass Flow Controller

A Burkert 8711 Mass Flow Controller for Gasses is used to supply air.

Table A.3: Specification

Nominal Flow	2 L/min
Max Operating pressure	5.5 Bar
Power Supply	24 V
Input/Output Signal	$0-10 \text{ V}$



Figure A.4: Burkert MFC 8711

A.4 Water Pump

A Elegant-Inline 12V water pump from Comet is used for water supply.

Table A.4: Some specifications for Water Pump

Voltage	12 V
Max current	2.2 A
Delivery Height	max 5.5 m
Volume Flow	max 10 L/min



Figure A.5: Comet Elegant-Inline 12V water pump

A.5 Flowmeter for water

A TecFluid Flowmeter series 2100 is used to control the amount of water supply.

Table A.5: Some specifications for TecFluid Flowmeter

Flowrate	0.4 - 4 <i>L/min</i>
Working pressure	max 15 <i>bar</i>



Figure A.6: TecFluid series 2100 flowmeter

Appendix: Extra Uploaded Content

B

The following are uploaded along with this Master Thesis:

- VOF-Model (OpenFOAM case files)
- Two-Fluid Flow Model - Base (CFX-files)
- Two-Fluid Flow Model - Extended (CFX-files)
- SolidWorks files of the Plexiglass cell with mini-channel
- Paper for in-house conference
 - *Visualization and Characterization of Two-Phase Flow in PEM Water Electrolysis Cell: An Experimental study*